The Forming Galaxy Clusters at the Cosmic Noon

SHIMAKAWA RIZUMU

Doctor of Philosophy

Department of Astronomical Science
School of Physical Sciences
SOKENDAI (The Graduate University for Advanced Studies)

The Forming Galaxy Clusters at the Cosmic Noon

Rhythm Shimakawa

A Thesis for the Degree of Doctor

SOKENDAI
(The Graduate University for Advanced Studies)

Department of Astronomical Science
School of Physical Sciences

April 2012 – May 2014
Subaru Jr. Research Internship, Subaru Telescope

June 2014 – March 2015
Subaru Research Internship, Subaru Telescope

April 2015 – March 2017
Research Fellowship (DC2), Japan Society for the Promotion of Science (JSPS)

This research was done under the supervision of Dr. Tadayuki Kodama with the financial supports of the Japan Society for the Promotion of Science (JSPS KAKENHI Grant Number 15J04923) through JSPS research fellowships for young scientists. This work was also partially supported by the Research Fund for Students (2013) of the Department of Astronomical Science, SOKENDAI (the Graduate University for Advanced Studies).

Abstract

— Galaxy protoclusters at the peak epoch of cosmic star-formation ($z = 2$–3) are ideal test beds to characterise how the present-day cluster galaxies have been formed. These massive systems can directly tell us what physical mechanisms are responsible for the galaxy diversity that is strongly dependent on the environment as clearly seen in the present-day Universe.

— In this *Thesis*, we have conducted and presented very deep Hα line imaging observations of the two known protoclusters (PKS 1138 at $z = 2.2$ and USS 1558 at $z = 2.5$) with MOIRCS on the Subaru Telescope, as an intensive systematic search for high-z star-forming galaxies across various environments. In addition, we have carried out a panoramic Lyα line imaging for one of the target protoclusters, USS 1558, using the Suprime-Cam on Subaru, which is the first systematic dual Hα and Lyα lines survey of a high-z protocluster field.

— Based on the improved technique of narrowband selection, we have successfully identified 249 Hα emitters (HAEs) in total associated with the two protoclusters, down to the stellar mass of 1×10^8 $M_\odot$ and SFR of 2 $M_\odot$/yr. Such a large number of HAEs can trace a wide range of environments up to the highest density regions ever studied, allowing us to investigate the environmental dependence of the physical properties of galaxies in detail even on the sub-structure or group scale ($\lesssim 300$ physical kpc).

— Narrowband imaging has a great advantage as it can sample less massive and less active star-forming objects whose stellar continua are very faint but emission lines are strong enough to be detected. Deep Hα line imaging have identified 54 low-mass HAEs with stellar masses $< 1 \times 10^9$ $M_\odot$. Some of those low mass galaxies show remarkably high star-forming activities (with specific SFRs higher than $(0.1\ \mathrm{Gyr})^{-1}$), and thus significantly deviate from the typical star-forming main-sequence. These active low-mass HAEs tend to show higher observed Hα/UV luminosity ratios. However, the ratios do not correlate with dust extinction measured from SED fitting. This suggests that they have exceptionally hard ionisation fields due to their young ages and low metallicities.

— We have found that the protoclusters' dense cores tend to contain the large numbers of more massive and/or more active star-forming galaxies, and yet they are not significantly deviated from the star-forming main sequence on the stellar mass versus SFR

diagram. On the other hand, dependencies of the physical properties on the environment are diverse among different cluster/group structures. This may suggest that the environmental effects on galaxy formation depend on the stage of cluster/group formation and evolution in the course of the cosmic mass-assembly history.

— We also find that the large-scale structures traced by Lyα emitters (LAEs) around the protocluster core nicely follow the overdensities of HAEs on a large scale. The peak of LAE number density (4 sigma overdesnsity) actually coincides with the USS 1558 protocluster on a large scale. On a smaller scale, however, we do not see any excess of number density of LAEs in the densest groups of HAEs within the protocluster. Rather, LAEs are remarkably missing in those very dense regions. The fraction of LAEs among the entire HAE sample is only one per cent in the high-density regions (upper half in the mean projected distance) in USS 1558, which is an order of magnitude lower than that in low-density regions (lower half). Furthermore, the composite images of HAEs divided into two sub-samples according to the mean projected distance indicate that the escape fraction of Lyα photons is lower in high-density regions. These phenomena suggest that denser circumgalactic/intergalactic matters may deplete the Lyα emission lines originated from star-forming galaxies in the densest groups of the protocluster.

— Based on all these results presented in this *Thesis*, we conclude that the densest regions at z = 2–3 are indeed hosting the formation of the progenitors of massive galaxies that grow into early-type galaxies at the bright end of the red sequence commonly seen in the present-day galaxy clusters. The young protocluster cores without a prominent red sequence are probably in the mid of vigorous accretion of cold gas (cold streams) as predicted by the modern cosmological simulations, since we find the clear depletion effect of Lyα emission lines there. Our first systematic combined analysis of both Hα and Lyα lines in the protocluster environments have provided us with new insights into the physical mechanisms of galaxy formation in the the early phase of galaxy cluster assembly.

Contents

1 | Background

Galaxy protoclusters (Sunyaev & Zeldovich, 1972) at the peak epoch of cosmic star-formation ($z = 2 - 3$) are ideal laboratories where we can understand how cluster galaxies form and grow during the course of cosmic mass-assembly history and the build-up of large-scale structures (LSSs) (White & Frenk, 1991; Cole et al., 2000) in the cold dark matter dominated Universe (Blumenthal et al., 1984; Davis et al., 1985; Bullock et al., 2001). These objects directly inform us of what are occurring in the early phase of cluster formation and galaxy formation therein, which then tell us what the physical mechanisms are that lead to the galaxy diversity depending on the surrounding environments seen in the local Universe (Hubble, 1926, 1936; Toomre & Toomre, 1972; Dressler, 1980). With such motivations, a bunch of research groups, including ourselves, have conducted intensive protocluster surveys (e.g. MAHALO-Subaru, Kodama et al. 2013; ZFIRE, Nanayakkara et al. 2016) in the past decade. Our knowledge of galaxy formation processes, especially for high-z galaxies has been remarkably advanced thanks to the intensive observational programs such as SINS (Förster Schreiber et al., 2009), 3DHST (van Dokkum et al., 2011), KBSS-MOSFIRE (Steidel et al., 2014), MOSDEF (Kriek et al., 2014), and KMOS3D (Wisnioski et al., 2015) that utilize state-of-the-art instruments such as MOSFIRE on Keck and KMOS on VLT. This *Thesis* begins with describing the scientific backgrounds related to our motivations as well as summarising recent achievements by those studies.

1.1 Habitat segregation of galaxy populations in the Universe

Galaxy cluster is the largest system in the Universe, consisting of 100s–1000s of galaxies bound together by self-gravity. For example, Abell 1656 known as Coma Cluster (Hammer et al., 2010), is one of the largest galaxy clusters in the local Universe (Abell et al., 1989). This cluster has a dynamical mass over 10^{15} $M_\odot$ (Gavazzi et al., 2009) and the cluster members move around very fast at a typical velocity of ~1000 km/s in the cluster core (Struble & Rood, 1999). Extended X-ray emission is an important characteristic of galaxy clusters (Sato et al., 2011) since the intra-cluster medium (ICM) is filled with hot plasma heated up to ~10^7–10^8 K by deep potential wells (Sarazin, 1986). The gravitational force comes largely from unseen material, i.e. dark matter, ~10 times more massive than visible objects, i.e. stars and intracluster gas in the Universe. In such an exotic environment, it is easy to imagine that galaxy formation and evolution processes can be different from those in low density regions or the general field, due to some internal and/or external effects such as ram pressure stripping, tidal interactions, and galaxy-galaxy mergers as noted by many past studies (Gunn & Gott, 1972; Fujita, 1998; Okamoto & Habe, 1999; Fujita & Nagashima, 1999; Abadi et al., 1999; Quilis et al., 2000; Okamoto & Nagashima, 2001,

2003; Fujita, 2004; Boselli & Gavazzi, 2006; Gottlöber et al., 2001; Roediger & Brüggen, 2007; Kronberger et al., 2008a,a,b; Kodama & Bower, 2001; Ellison et al., 2010; Peng et al., 2010b; Jaffé et al., 2012; Tal et al., 2014; Jaffé et al., 2015; Peng et al., 2015; Jaffé et al., 2016; Fillingham et al., 2016).

1.1.1 Galaxy properties in nearby galaxy clusters

Butcher & Oemler (1984) first reported a significant increase of blue star-forming galaxies in cluster cores with redshift; from only a few % at $z = 0$, to 10% at $z = 0.23$, and to 20% at $z = 0.4$, based on the photometric data. Red early-type galaxies whose optical-to-near infrared lights are dominated by old stars such as red-giant-branch (RGB) stars and asymptotic-giant-branch (AGB) stars, increase towards cluster centres and towards lower redshifts. This evolutionary trend is called the *Butcher-Oemler (BO) effect* (see also Couch et al. 1994; Dressler et al. 1994; Goto et al. 2003), which is consistent with a picture of hierarchical growth of clusters where galaxies are formed earlier in biased dense cluster cores and clusters grow by accretion of galaxies from surrounding regions (Navarro et al., 1995, 1996; Bullock et al., 2001; Ellingson et al., 2001; McGee et al., 2009). During the course of mass-assembly, star-forming activities in infalling galaxies are considered to be quenched by losing their gas due to ram pressure or tidal stripping (Abadi et al., 1999; Moore et al., 1996, 1998, 1999; Kodama & Smail, 2001).

Predominant early-type galaxies in nearby galaxy clusters show a tight red sequence called colour–magnitude relation (Visvanathan & Sandage, 1977; Dressler, 1980; Gladders & Yee, 2000; López-Cruz et al., 2004; Kodama et al., 2005; Gilbank et al., 2011), which begins to appear at around $z = 2$–3 (Kodama et al., 2007). On the other hand, late-type galaxies are located at bluer side on the colour-magnitude diagram and they are called as the "blue cloud" galaxies in contrast to the "red sequence" galaxies. Galaxies in random fields are known to have bimodal populations separated to red sequence and blue cloud galaxies (Kodama et al., 1999; Strateva et al., 2001; Bell et al., 2004; Baldry et al., 2004), while the distinction of the two is less prominent. Such a very tight red sequence of galaxy clusters suggests that cluster galaxies would have been evolved earlier and then quenched on a shorter time scale (Trayford et al., 2016).

In this context, majority of galaxy population in the centre of nearby galaxy clusters consists of red, early-type ellipticals and S0s (Skibba et al., 2009), which is known as "morphology–density" relation (Dressler, 1980; Dressler et al., 1997; Bamford et al., 2009). This clear piece of observational evidence for environmental dependence is also seen as the kinematic morphology–density relation (Cappellari et al., 2011). A larger fraction of spheroidal galaxies classified as *slow rotators* or boxy ellipticals (Kormendy & Bender, 1996) can be seen in local galaxy clusters compared to the general field. Boxy ellipticals tend to be dispersion-dominated spheroidal galaxies (Emsellem et al., 2011) rather than rotation-dominated. They are considered to be produced by galaxy-galaxy mergers/interactions (Okamoto & Nagashima, 2001; Jesseit et al., 2009; Naab et al., 2014), indicating that the star-forming activities are externally affected in dense environments.

1.1.2 Nature or nurture

These early studies suggest that the environmental dependence of galaxy formation and evolution originates from two effects, namely, "nature" and "nurture" effects. The nature effect means that galaxies formed in dense environments are intrinsically more evolved due to biased galaxy formation, and thus are older and redder (Kauffmann, 1996; Bower et al., 1998; Thomas et al., 2005; De Lucia et al., 2006). In contrast, the nurture effect means that today's early-type galaxies in dense regions have been deformed through some external effects from the surrounding environments (Moore et al., 1996, 1998; Okamoto & Nagashima, 2003; Prieto et al., 2013). These effects have been commonly interpreted in combination. An example of the nurture effects is a frequent merger events in dense environments that produce compact spheroidal galaxies though dissipational processes as predicted theoretically by Mihos & Hernquist (1996) and many others (e.g. Barnes & Hernquist 1996; Bournaud et al. 2007; Jesseit et al. 2009; Hopkins et al. 2008, 2010). In high density regions, galaxy collisions occur more often as predicted theoretically (Okamoto & Habe, 2000; Gottlöber et al., 2001; Fakhouri & Ma, 2009; Jian et al., 2012), and also observationally (Lin et al. 2010; Kampczyk et al. 2013 but see Darg et al. 2010). However, there is little direct evidence at high redshifts in observational perspectives (Hine et al., 2016), and thus it is still a frontier area to explore how the star-forming galaxies have evolved and then quenched since $z > 2$.

1.2 The cosmic high noon

The cosmic star-formation history has been explored with multi-band data from ultraviolet to radio wavelengths. The cosmic star-formation rate density as a function of redshift is known as Madau-Liily plot since it was first reported by Madau et al. (1996); Lilly et al. (1996), which has been developed by deeper and wider extragalactic surveys in various wavelength ranges and various ways (e.g. Hughes et al. 1998; Iwata et al. 2003; Chapman et al. 2005; Le Floc'h et al. 2005; Schiminovich et al. 2005; Hopkins & Beacom 2006; Iwata et al. 2007; Dahlen et al. 2007; Pérez-González et al. 2008; Reddy & Steidel 2009; Bouwens et al. 2011; Magnelli et al. 2011; Cucciati et al. 2012; Bouwens et al. 2012; Magnelli et al. 2013; Gruppioni et al. 2013; Behroozi et al. 2013a; Sobral et al. 2014; Khaire & Srianand 2015; Rowan-Robinson et al. 2016, and for more discussion, see papers in Madau & Dickinson 2014). To constrain the cosmic star-formation history is important not only because it helps to understand galaxy formation mechanism but also since it predicts cosmic supernova rates for example (Dahlen et al., 2004; Hopkins & Beacom, 2006; Mannucci et al., 2007; Botticella et al., 2008; Horiuchi et al., 2011). The cosmic star-formation rate density compiled from various studies can be expressed by the following equation,

$$\psi(z) = 0.015 \frac{(1+z)^{2.7}}{1+[(1+z)/2.9]^{5.3}} \quad \mathrm{M_\odot\ yr^{-1} Mpc^{-3}}, \tag{1.1}$$

which is the formula given by Madau & Dickinson (2014). The cosmic star-formation rate density at $z \sim 1$ is significantly higher by about one order of magnitude than that of $z = 0$. The redshift interval between two and three is known to be the peak epoch of

star-forming activities, and it is sometimes called the "cosmic high noon" in analogy to the "cosmic dawn" at very high redshifts ($z > 6$). AGNs are also much more active than that in the local Universe (Haehnelt & Rees, 1993; Hopkins et al., 2007; Booth & Schaye, 2009; Yamada et al., 2009; Shankar et al., 2009; Aird et al., 2010). The main bodies of most of the galaxies seen today were constructed during this epoch. Therefore, this epoch is critically important in order to draw a general picture of galaxy formation and evolution.

On the flip side, we had been calling this critical era for galaxy formation and evolution as the "redshift desert" up until a few years ago. The major spectral features (e.g. emission lines) are located in the rest-frame optical regime (λ = 3500–9000 Å) as seen in the spectral libraries of Sloan Digital Sky Survey (SDSS) (Abazajian et al., 2009; Eisenstein et al., 2011). At $z > 1.5$, these features are all redshifted to the near-infrared regime, and there has long been no instruments with great sensitivities enough to detect those multiple-lines and/or continuum spectra individually until some time ago. However, the cosmic high noon era is now no longer a “redshift desert" after the advent of cutting-edge near-infrared spectrographs such as MOSIFRE on the Keck, KMOS on the VLT launched recently, as well as the space-based intensive spectral survey with HST (3D-HST; van Dokkum et al. 2011). We now have thousands of deep galaxy spectra at around the peach epoch of cosmic star-formation as described in the following sections.

1.2.1 Increased star-formation activities at high redshifts

It is well known that stellar mass and SFR are closely correlated with each other in the sense that more massive star-forming galaxies tend to be more active. This tight relationship is referred to as the “star-forming main sequence" (Brinchmann et al., 2004; Salim et al., 2007; Daddi et al., 2007a; Elbaz et al., 2007; Noeske et al., 2007). Recent measurements can be seen in the literatures (Speagle et al., 2014; Whitaker et al., 2014; Shivaei et al., 2015; Tomczak et al., 2016). The redshift evolution of the main sequence is also seen, which roughly scales as SFR$\propto (1+z)^2$ (Whitaker et al., 2014), although the scaling parameter strongly depends on stellar mass and the calibrations of SFR (Whitaker et al., 2014; Shivaei et al., 2015). Such highly active star-formation at high redshifts would be supported by rich gas reservoirs and vigorous gaseous inflows and as inferred from recent studies, e.g., higher gas fraction of star-forming galaxies at $z > 1$ based on CO line observation in the radio regime (Tacconi et al., 2010, 2013; Daddi et al., 2010; Riechers et al., 2010; Geach et al., 2011; Carilli & Walter, 2013). The ratio of gas mass to stellar mass scales as $\sim (1+z)^2$, which agrees with the evolution of the star-forming main sequence (Whitaker et al., 2014; Tomczak et al., 2016). Also, the HI optical depth increases with redshift and scales as $\sim (1+z)^{4.3}$ since the epoch of reionisation as investigated by Lyα forest analyses of background quasars (Songaila & Cowie, 2002; Fan et al., 2006b,a; Becker et al., 2007). Likewise, gas accretions would be more vigorous at high redshifts as predicted by cosmological simulations (Kereš et al., 2005; Bouché et al., 2010), observations (Bouché et al., 2013) and semi-empirical chemical evolution model (Cresci et al., 2010; Yabe et al., 2015; Seko et al., 2016).

Since star-forming galaxies tend to have higher gas fractions at this epoch (Obreschkow & Rawlings, 2009; Tacconi et al., 2010; Daddi et al., 2010; Lagos et al., 2011; Tacconi et al., 2013; Carilli & Walter, 2013), mergers of those galaxies within groups at $z > 2$ must be highly dissipational. The major-merger is expected to be a dominant mechanism that drives the morphology transformation at high redshifts (Lofthouse et al., 2016). In this context,

high-z overdense environments would be the ideal site where the morphology–density relation seen at low-z is established since we expect higher chance of wet mergers due to higher number density of galaxies. Recent observations of high-z protocluster fields have suggested a significant increase of dusty star-forming populations that may be caused by galaxy mergers (Tran et al., 2010; Koyama et al., 2013a,b; Santos et al., 2014; Hatch et al., 2017). However, protocluster galaxies seem to follow the same main sequence of star-forming galaxies in the random fields. We are still unsure if such a high fraction of dusty star-formation is directly related to the formation of the morphology–density relation.

On the other hand, we still have a puzzle what mechanisms can stop such intense star-forming activities. Even both semi-analytic and hydrodynamical simulations that generally tend to underestimate SFRs of star-forming galaxies at $z = 1$–4 (see Sparre et al. 2015), often suffer from incorporating proper feedback models. This seems to tell us that more active star-formation seen in high-z galaxies cannot not be suppressed easily. Recent observations and simulations are addressing this controversial issue, and have suggested some negative feedback scenarios such as the virial shock heating (Birnboim & Dekel, 2003; Dekel & Birnboim, 2006; Birnboim et al., 2007; Kereš et al., 2009), AGN feedback (Sijacki et al., 2007; Schawinski et al., 2007b; Cattaneo et al., 2007; Okamoto et al., 2008; Cattaneo et al., 2009; Kaviraj et al., 2011; Cano-Díaz et al., 2012; Olsen et al., 2013; Genzel et al., 2014b; Cicone et al., 2014; Costa et al., 2014; Muratov et al., 2015), morphological quenching (Martig et al., 2009; Davis et al., 2014; Omand et al., 2014; Whitaker et al., 2015), gravitational heating (Dekel & Birnboim, 2008; Johansson et al., 2009; Genzel et al., 2014a), and environmental quenching (Baldry et al., 2006; Schawinski et al., 2007a; Peng et al., 2010b, 2015). Those new models and interpretations are helping us to understand the galaxy feedback processes. Especially, some past studies have reported that number excess of AGNs in the overdense regions at high redshifts (Ohta et al., 2003; Lehmer et al., 2009, 2013; Tanaka et al., 2013a), which may be related to the building of the tight red sequence in galaxy clusters at low redshifts (Schawinski et al., 2007a; Montero-Dorta et al., 2009).

1.2.2 Physical conditions of interstellar medium

Since high redshift galaxies tend to be more active, less chemically-enriched, and accreting a lot of cold gas from surrounding regions, the physical states of the interstellar media of galaxies would be different from those of local galaxies. The BPT diagram is one of the most familiar diagnostics to explore the physical conditions of interstellar medium (ISM) within galaxies, and to identify narrow-line AGNs based on the two line ratios in the rest-optical ([O I]λ6302, [S II]$\lambda\lambda$6718, 6733, or [N II]λ6585/ H$\alpha\lambda$6565 versus [O III]λ5008/ H$\beta\lambda$3728), which was first proposed by Baldwin et al. (1981); Veilleux & Osterbrock (1987). The location on the BPT diagram is determined by various physical quantities such as gas-phase metallicity and stellar ionizing radiation field (hardness and normalization). Typical star-forming galaxies where photoionisation in ISM is driven by young massive OB stars (Strömgren, 1939) form a tight sequence on this diagram (Fig. 1.1), known as the *chemical abundance sequence* (Kauffmann et al., 2003). The presence of the tight sequence thus indicates that these physical parameters are closely correlated and vary only in a systematic way. On the other hand, narrow-line AGNs are located in the branch on the right-hand

side of the BPT (Kewley et al., 2001), because of enhancement of collisionally-excited emission lines by thermal excitation (Hollenbach & McKee, 1989), photo-dissociation (Hollenbach & Tielens, 1999), and extremely energetic photons (Maloney et al., 1996) from the surrounding regions of massive black holes.

Interestingly, the abundance sequence of star-forming galaxies on the BPT diagram shifts upward and/or rightward with increasing redshift, which was first inferred from the composite spectra at $z > 1$ (Shapley et al., 2005; Erb et al., 2006a; Brinchmann et al., 2008; Liu et al., 2008; Yabe et al., 2012) but now we see this clear trend for individual galaxies at high-z (Fig. 1.1) by Kewley et al. (2013b,a); Trump et al. (2013); Newman et al. (2014); Steidel et al. (2014); Coil et al. (2015); Shapley et al. (2015); Sanders et al. (2016); Steidel et al. (2016); Strom et al. (2016). This intriguing evolution on the BPT diagram would be attributed to three physical parameters, namely, ionisation parameter, UV hardness, and electron density as demonstrated by (Kewley et al., 2013a).

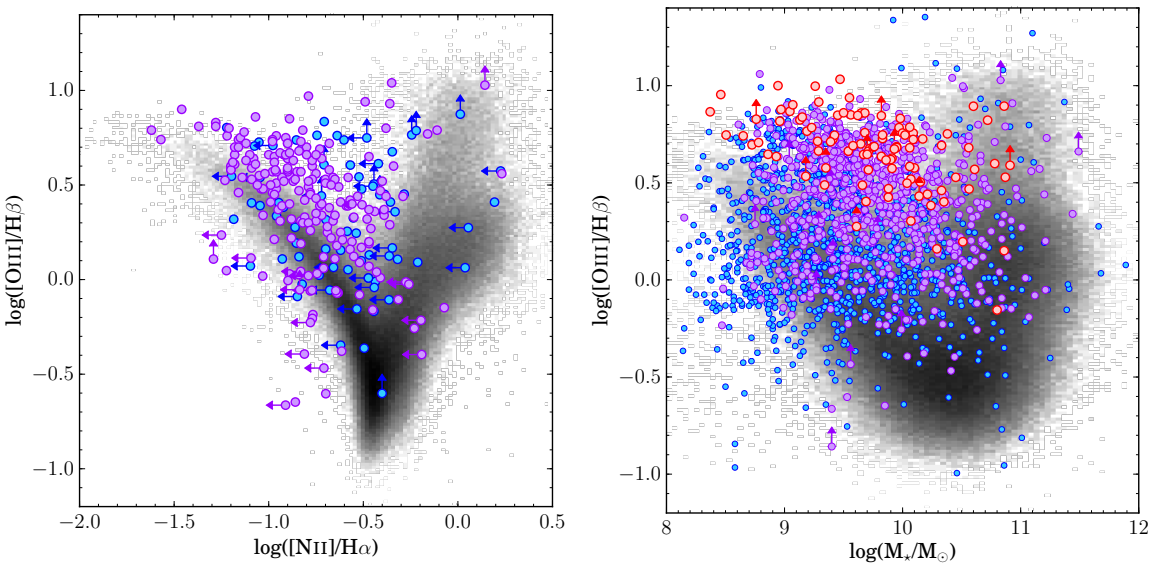

Figure 1.1: (Left) BPT diagram. The black 2D histogram shows the galaxies at $z \sim 0.1$ (366,243 objects) from the SDSS library (Abazajian et al., 2009). Blue and purple symbols are galaxies at z = 1–2 (73 objects) and 2–3 (278) from Trump et al. (2013); Nanayakkara et al. (2016) and Newman et al. (2014); Steidel et al. (2014); Nanayakkara et al. (2016), respectively. (Right) Mass-excitation (MEx) diagram. Black 2D histogram is the same as shown on the left. Blue, purple, and red filled circles indicate galaxies at z = 1–2 (1,201 objects), 2–3 (754), and 3–4 (100) cited from Trump et al. (2013); Momcheva et al. (2016); Nanayakkara et al. (2016), Newman et al. (2014); Steidel et al. (2014); Momcheva et al. (2016); Nanayakkara et al. (2016), and Troncoso et al. (2014); Holden et al. (2016); Onodera et al. (2016); Suzuki et al. (in preparation), respectively.

Firstly, the ionization parameter is raised by a large flux of hydrogen ionizing photons and a higher pressure of interstellar medium. Highly active star-forming galaxies commonly seen at high-z (Daddi et al., 2007a; Elbaz et al., 2007; Noeske et al., 2007) can eject a larger amount of ionising photons, which push the abundance sequence upper-leftward. Also, higher electron densities and harder radiation field enhance collisionally-excited emission lines, which move the abundance sequence upper-rightward. Recent near-infrared spectroscopic surveys have reported that star-forming galaxies at $z > 2$ have higher ioni-

sation parameters (Nakajima et al., 2013; Nakajima & Ouchi, 2014; Shapley et al., 2015; Sanders et al., 2016; Onodera et al., 2016; Strom et al., 2016), higher electron densities (Shimakawa et al., 2015b; Sanders et al., 2016; Onodera et al., 2016; Strom et al., 2016), and harder ionisation field (Steidel et al. 2014, 2016; Strom et al. 2016, see also Lowenthal et al. 1997; Shapley et al. 2003; Iwata et al. 2009; Eldridge & Stanway 2012). These results strongly suggest that high-z galaxies commonly have highly-excited ISM conditions. However, the most plausible cause of the significant upward elevation on the BPT in some star-forming galaxies would be their harder ionisation field as shown by Steidel et al. (2014); Strom et al. (2016). In fact, the effective temperature of stars are hotter and also the optical depth of stellar atmosphere is thinner in high-z galaxies compared to local objects due to their much lower Fe abundance. Moreover, such a harder ionisation fields would be attributed to the fact that the lifetime of metal poor binary system is significantly prolonged due to "quasi-homogeneous evolution" (Eldridge et al., 2011; Eldridge & Stanway, 2012). In metal-poor condition, massive stars can live (Stanway et al., 2016) over their main sequence lifetimes (H⇒He) as if they are fully-mixed, since lower-Z stars can retain rapid rotation over their lifetimes because of less-impact of spinning down by stellar-winds. This quasi-homogeneous evolution model is very consistent with the composite FUV continuum and stellar and nebular lines of star-forming galaxies seen at $z > 2$ (Steidel et al., 2016).

From the perspectives of environment effects, the ISM conditions of protocluster galaxies may well be different from those of typical galaxies in the general field if star-formation histories depend on the environment (Thomas et al., 2005; Elbaz et al., 2007), in particular, galaxy mergers are thought to be more frequent in overdense regions at high-z (Okamoto & Habe, 2000; Gottlöber et al., 2001). However, most of the past spectroscopic studies have reported that protocluster galaxies do not show different ISM properties compared to field galaxies (Shimakawa et al., 2015a,b; Valentino et al., 2015; Kewley et al., 2016) apart from the enhancement of gas-phase metallicity in high-density regions (Kulas et al., 2013; Shimakawa et al., 2015a). This may make sense if the short lifetimes ($\leq$ 100 Myr) and small sizes (smaller than several hundred per sec) of individual HII regions would be negligible compared to the dynamical time scale and > kpc scale size.

1.2.3 Role of circumgalactic/intergalactic medium

Circumgalactic/intergalactic media (CGM/IGM) are critical components for galaxy formation. This is particularly linked to the gas feeding mechanism of galaxies, which is thought to depend on the cosmic age, halo mass and environment (Kereš et al., 2005). It is especially complicated at z = 2–3 (Dekel et al., 2009a,b) when the massive galaxies are just forming. As many modern cosmological simulations show, radiative cooling and self-shielding dominate in the filamentary CGM at high-z (Kereš et al., 2009; van de Voort et al., 2011). This allows cold gas to cool and stream into galaxies by penetrating the hot massive halos $\geq 10^{12}$ $M_\odot$ (Dekel & Birnboim, 2006; Dekel et al., 2009a).

CGM/IGM properties are closely related to the chemical evolution of galaxies. In fact, the chemical abundance of galaxies and its evolution provide cumulative information of gas inflows, star-formation activities, and ejection of metals by supernova driven outflows across the cosmic times (Tinsley, 1980). The overall clear relationship between stellar-mass and gaseous metallicity, known as mass–metallicity (MZ) relation and the scatter around this relation (Tremonti et al., 2004) have critical information and are fundamental tools

to investigate the above mentioned baryonic physical processes (Mannucci et al., 2010; Zahid et al., 2014). It is known that the scatter significantly decreases by incorporating the second parameter, SFR (Mannucci et al., 2010) or HI mass (Bothwell et al., 2013), and such three dimensional relationship is known as the fundamental metallicity relation (FMR; see also Mannucci et al. 2011; Peeples & Shankar 2011; Yabe et al. 2012; Niino 2012; Yates et al. 2012; Dayal et al. 2013; Stott et al. 2013; Andrews & Martini 2013; Lilly et al. 2013; Troncoso et al. 2014; Nakajima & Ouchi 2014; Steidel et al. 2014; Sanders et al. 2015; Kacprzak et al. 2016). Most of these studies show that the scatter around the MZ relation is mainly driven by the correlation between SFR and metallicity at a given stellar mass in the sense that galaxies with higher SFRs tend to have lower metallicities, however, such a correlation seems to be weaker in high-z star-forming galaxies. The FMR is given by $12+\log(\mathrm{O/H}) = \log(\mathrm{M}_\star) - 0.32\ \log(\mathrm{SFR})$ and it has a scatter of only 0.05 dex as reported in the early work by Mannucci et al. (2010). Moreover, the form of the FMR seems to be unchanged out to $z \sim 2.5$, perhaps indicating that most of the star-forming galaxies can evolve only *on* the plane suggesting that star-formation and chemical enrichment are well regulated in galaxies in a secular manner over the past eleven billion years (Mannucci et al., 2010). Then, the FMR plane is recalibrated to $12+\log(\mathrm{O/H}) = \log(\mathrm{M}_\star) - 0.66\ \log(\mathrm{SFR})$ by Andrews & Martini (2013) based on more sophisticated metallicity diagnostic (direct T_e method; Izotov et al. 2006). However, it should be noted that the measurement of gas-phase metallicities is still challenging since the commonly-used calibrations, either empirically or theoretically defined (McGaugh, 1991; Zaritsky et al., 1994; Pilyugin, 2001; Kewley & Dopita, 2002; Pettini & Pagel, 2004; Kobulnicky & Kewley, 2004; Pilyugin & Thuan, 2005; Nagao et al., 2006; Liang et al., 2006; Yin et al., 2007; Maiolino et al., 2008), have considerable uncertainties depending on ISM conditions of galaxies (Kewley & Ellison, 2008). Further investigation, both observationally and theoretically, are clearly required.

Environment is also important in view of chemical evolution (Oppenheimer & Davé, 2008; Davé et al., 2011), as diversities in CGM/IGM at different environments can affect the metal enrichment history through the cosmic time (Davé et al., 2011; Genel, 2016; Bahe et al., 2016). The nature effects would lead to earlier chemical enrichments of CGM/IGM (Genel, 2016), while the nurture effects may enrich chemical abundances of galaxies especially in satellite galaxies in overdense environments, due to ram pressure stripping of outer metal-poor envelope (Bahe et al., 2016) or recycling of chemically-enriched outflowing gas (Davé et al., 2011). Thus, both effects are expected to increase the gas-phase metallicities of cluster galaxies, which is actually seen in low-z galaxy clusters (Ellison et al., 2009; Hughes et al., 2013). However, observational results for high-z protoclusters are still controversial (Kulas et al., 2013; Shimakawa et al., 2015a; Valentino et al., 2015; Kacprzak et al., 2015). We have not yet reached any fully consistent picture especially at high redshifts regarding the chemical evolution which may be closely related to the surrounding CGM/IGM.

To characterise the CGM/IGM properties, the analyses of absorption lines such as Lyα and some metallic lines in the rest-FUV wavelength is very useful. Absorption lines can be observed anywhere below the wavelength of Lyα electron transition at 1216 Å in the spectra of high-z quasars (Lyα forest; Lynds 1971), arising from intervening neutral hydrogen in the intergalactic medium (Gunn & Peterson, 1965; Sargent et al., 1980; Rauch, 1998; Fan et al., 2006a; Meiksin, 2009). By comparing the observed Lyα forest spectra with the intrinsic SED without IGM absorption, we can constrain the optical depth of IGM,

which is known to correlate with galaxy overdensities (Kollmeier et al., 2003; Lee et al., 2014b,a, 2016; Cai et al., 2016a). This technique is the only way to evaluate overdensities at high redshfits independent of galaxy selection bias. In addition to that, metal absorption lines such as C, N, Si, O embedded in IGM would provide us with insights into chemical enrichments of CGM/IGM by galactic winds (Adelberger et al., 2005; Oppenheimer & Davé, 2006; Simcoe et al., 2006; Scannapieco et al., 2006; Schaye et al., 2007; Fox et al., 2007; Steidel et al., 2010).

1.3 Mahalo-Subaru

1.3.1 MAHALO-Subaru project

With all these backgrounds and motivations, we aim to construct a large, systematic, representative samples of star-forming galaxies across cosmic times and various environments, covering the peak epoch of galaxy formation ($1 < z < 3$). We have launched an observational program on Subaru, an 8.2 m aperture telescope on MaunaKea in Hawaii (Iye et al., 2004). The project is called "MAHALO-Subaru" (*Mapping H-Alpha and Lines of Oxygen with Subaru*) led by T. Kodama at NAOJ (Kodama et al., 2013). Our core sample consists of eight known clusters/protoclusters at $1.4 < z < 3.7$, and an unbiased general field UDS-SXDF-CANDELS (Lawrence et al., 2007; Furusawa et al., 2008; Grogin et al., 2011) at z =2.19, 2.53, 3.18, and 3.62 slices. We can systematically map out the galaxies which happen to have redshifted emission lines in our narrowband filters across the entire fields of imaging observations as demonstrated by our past studies (Kodama et al., 2004; Koyama et al., 2010, 2011). For this purpose, we have employed unique sets of narrowband filters on two wide-field cameras, the Subaru Prime Focus Camera (Suprime-Cam; Miyazaki et al. 2002) and the Multi-Object InfraRed Camera and Spectrograph (MOIRCS; Ichikawa et al. 2006; Suzuki et al. 2008). This program has been conducted over $\sim$ 20 nights so far including the six nights allocated as the Subaru intensive program (Kodama et al. S10B-028).

To our great success, we have been identifying lots of H$\alpha\lambda$6565, [OII]$\lambda\lambda$3727,3730, and [OIII]λ5008 emitter candidates that are associated to the known clusters/protoclusters, and those in narrow redshift slices in the random fields at z = 1–4 (Hayashi et al., 2010, 2011; Tanaka et al., 2011; Tadaki et al., 2011, 2012; Hayashi et al., 2012; Koyama et al., 2013a; Tadaki et al., 2013, 2014; Koyama et al., 2014; Suzuki et al., 2015). The highlights of the project include the discovery of very high star-forming activities in the cores of protoclusters at $z > 2$ which must correspond to the forming phase of the present-day passive galaxy populations which are dominant in low redshift rich clusters. The peak of star-formation is then shifted outwards of the clusters with time from $z \sim 3.0$ to $z \sim 0$, indicating the inside-out growth or quenching of clusters (Koyama et al., 2010, 2011; Hayashi et al., 2011; Koyama et al., 2013a; Shimakawa et al., 2014). Such high activity and its spatial propagation are often accompanied by the interesting type of populations, i.e. red (Hα) emitters. They always coincide with the most active environments at any epoch, and therefore they are highly relevant populations to the environmental effects. The red Hα emitters are two-fold: they are either reddened by dust extinction associated to vigorous star forming regions or they are already being truncated and their star-formation rates are declining (hereafter we call these two phases "dust reddening" and "passive reddening" respectively). In both cases, they are likely to be the key populations under the influence of

environmental effects. For instance, galaxy-galaxy mergers tend to involve dust-obscured star-burst initially, followed by the AGNs activation at the galaxy centres, and then the star-forming activities are quenched by the AGN feedback (Fabian, 2012; Cano-Díaz et al., 2012; Schawinski et al., 2014; Genzel et al., 2014b). It is often suggested that AGNs may stop star-formation (sometimes called as "negative" feedback) and contribute to form massive quiescent spheroidal galaxies (Schawinski et al., 2007b, 2009a,b, 2010). Also, it is expected that the hot intra-cluster medium (ICM) trapped in the deep cluster potential wells would strip or evaporate the HI gas around the galaxies residing in the massive haloes, and thus gaseous inflows would be stopped, and then star formation activity is declined slowly (e.g. Gunn & Gott 1972; Fujita 1998; Fujita & Nagashima 1999; Abadi et al. 1999; Quilis et al. 2000; Okamoto & Nagashima 2003; Fujita 2004; Boselli & Gavazzi 2006; Roediger & Brüggen 2007; Kronberger et al. 2008a,a,b from theoretical perspective, and Kodama & Bower 2001; Peng et al. 2010b; Jaffé et al. 2012; Tal et al. 2014; Jaffé et al. 2015; Peng et al. 2015; Jaffé et al. 2016; Fillingham et al. 2016 from observational viewpoints). Such phenomena would redden galaxy spectra, and can actually often seen in the overdense environments in the local Universe (Kenney et al., 2004; Merluzzi et al., 2016). Considering these factors, the red Hα emitters are possibly in the transition phase from normal star-forming galaxies, to red, spheroidal, quiescent galaxies seen in today's galaxy clusters.

Our large sample of clusters/protoclusters also enable us to statistically investigate how the environmental dependence intrinsically biases the star-forming activities in dense environments. Koyama et al. (2013b) recently compare relations between stellar mass and star-formation rates (SFRs) known as the star-forming main-sequence of star-forming galaxies (Daddi et al., 2007a; Elbaz et al., 2007; Noeske et al., 2007), based on the large combined samples of Hα emitters in three clusters at $z = 0.4$, 0.8, and 2.2 from MAHALO-Subaru and those in the general fields (UDS and COSMOS) from the HiZELs (the High-Z Emission Line Survey; Best et al. 2010). They show that star-forming galaxies in both low- and high-density regions follow the same main-sequence. However, the galaxy distribution along the main-sequence is clearly dependent on environment in the sense that protocluster galaxies tend to have higher masses and higher SFRs. They also show that the dust attenuation in cluster galaxies is higher than that in the field galaxies, by comparing the Hα emitters with those of the mid-infrared imaging data (MIPS/Spitzer). This further supports the scenario where dusty starbursts occur more frequently in dense environments due to external effects such as galaxy-galaxy mergers as predicted by N-body simulations (Gottlöber et al., 2001; Genel et al., 2014).

1.3.2 Spectroscopic follow-up campaigns

Upon all the achievements from the imaging data, we have carried out spectroscopic follow-up surveys at near-infrared with MORICS and MOSFIRE (the Multi-Object Spectrometer for InfraRed Exploration; McLean et al. 2010, 2012), in order to explore the physical states of star-forming galaxies in protocluster regions. This is a natural, straightforward extension of the MAHALO-Subaru narrow-band imaging survey, since important strong emission lines such [SII]$\lambda\lambda$6718, 6733, [NII]$\lambda\lambda$6550, 6585, H$\alpha\lambda$6565, [OIII]$\lambda\lambda$4960, 5008, H$\beta\lambda$4863, and [OII]$\lambda\lambda$3727, 3730 that are well-calibrated in local galaxies in the rest-frame optical (Brinchmann et al., 2004; Tremonti et al., 2004; Kauffmann et al., 2004; Andrews & Martini, 2013), are all redshifted to the near-infrared regime at $1.5 < z < 2.6$. Figure 1.2 represents

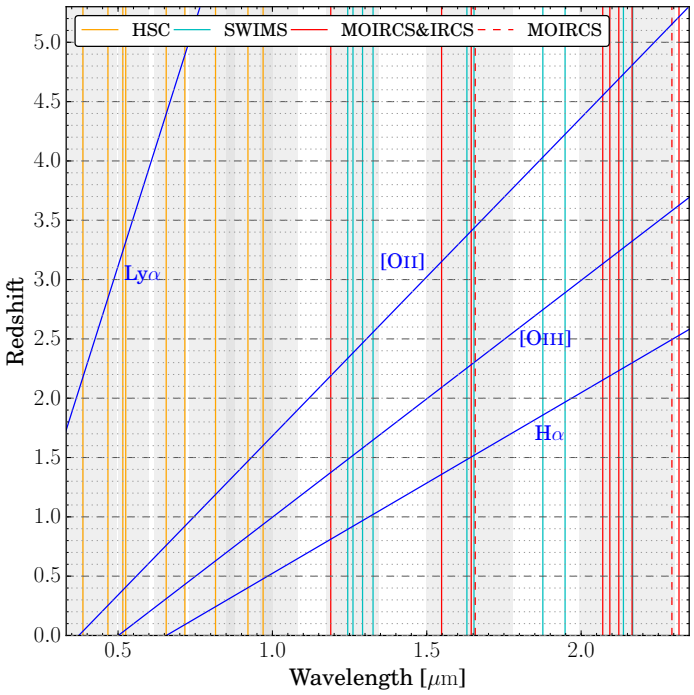

Figure 1.2: Spectral coverage of representative emission lines in the rest-optical regime and the narrowband filters on Subaru instruments, such as Hyper Suprime-cam (orange), SWIMS (cyan), both MOIRCS and IRCS (red solid lines), and MOIRCS only (red dashed lines).

the wavelength shift of the representative emission lines as a function of redshift and the availability of those lines in the near-infrared observations. For example, when we use the HK500 grism, a low resolution grism on the MOIRCS, [NII], Hα, [OIII], and Hβ lines can be accessed all at once at $z \sim 2$, which then enable us to make the BPT diagram (Baldwin et al., 1981; Veilleux & Osterbrock, 1987; Kewley & Dopita, 2002; Kauffmann et al., 2004; Brinchmann et al., 2008; Kewley et al., 2013b,a; Steidel et al., 2014, 2016) which is the most familiar line diagnostic diagram to study physical states of galaxies and to identify AGNs. In addition, we can estimate gas-phase metallicities of HAEs based on the several empirical calibrations (Pettini & Pagel, 2004; Nagao et al., 2006; Kewley & Ellison, 2008; Maiolino et al., 2008). We make a stress that our near-infrared spectroscopy is highly feasible and efficient, since our targets are selected by the presence of strong emission lines in the narrow-band filters.

The Hα emitters provide us with the best samples of star-forming galaxies in terms of depth, small dust obscuration, high completeness, and low contamination, as well as small selection bias, since Hα is the brightest emission line of typical star-forming galaxies (Sobral et al., 2013; An et al., 2014) and its strength is closely correlated with SFR (Kennicutt, 1998). The redshifts are also secure as we trace the emission lines. These are all great advantages of Hα emitters over other common selection techniques such as the UV selected galaxies at $z > 1.5$ (Erb et al. 2003; Steidel et al. 2004; Adelberger et al. 2004; Förster Schreiber et al. 2006; Erb et al. 2006b; Law et al. 2007; Genzel et al. 2011 and also see Reddy et al. 2005; Oteo et al. 2015). Such a high completeness enables us to identify filamentary/group structures/substructures traced by Hα emitters (HAEs) as clearly demonstrated by Hayashi et al. (2012); Koyama et al. (2013a). Our narrowband Hα imaging survey program have identified two particularly dense protoclusters where more than 60 of Hα-emitting star-forming galaxies, including some active nuclei (AGNs),

are associated in the vicinities of radio galaxies (RGs) at $z > 2$ within the MORICS field of view (FoV), namely, *USS 1558–003* at $z = 2.53$ (Hayashi et al., 2012), and *PKS 1138–262* at $z = 2.16$, (Koyama et al., 2013a) (hereafter PKS 1138 and USS 1558, respectively). We have conducted the follow-up near-infrared multi-object spectroscopy of HAEs in these two targets with MOIRCS and MOSIRE on April 2013 and June 2014, respectively (S13A039, Kodama et al.; S14A114, Shimakawa et al.).

The MORICS observations use two and three masks of the HK500 grism covering the wavelength range of 1.3–2.5 μm for PKS 1138 and USS 1558, respectively. Also one mask of VPH-K grism is partially used for PKS 1138. The observation was carried out with five allocated nights and the total integration time in each configuration (mask) was 126–276 minutes under 0.6–1.0 seeing condition. The obtained data were reduced in a standard manner by using the MOIRCS MOS Data Pipeline (MCSMDP: Yoshikawa et al. 2010) and the reduced spectra have limiting magnitude of $m_{AB} = 22.2 - 22.6$ in 1σ. Based on the spectra, we have eventually identified 27 and 36 HAEs in PKS 1138 and USS 1558, respectively (see details in Shimakawa et al. 2014, 2015a).

The MOSFIRE observation was focused on only USS 1558 due to the limited allocation time of one night. We used J and H band modes that provide high spectral resolutions of R = 3318 and 3660 in the range of $\lambda = 1.17$–1.35 and 1.47–1.80 μm, respectively. Due to the great sensitivities of the MOSFIRE, we detect multiple emission lines of individual sources in their deep spectra obtained after the standard data processing (Steidel et al., 2014). Those line fluxes are distributed between 0.5×10^{-17} and 10×10^{-17} erg s^{-1}cm^{-2} above the signal-to-noise ratios of 3.2 (Shimakawa et al., 2015b). In this spectroscopy, we gave higher priority to spectroscopically-confirmed members by the previous MOIRCS observation, but we newly confirmed additional four HAEs associated with USS 1558.

1.4 This thesis

Whilst our understandings of galaxy formation mechanisms at the cosmic high noon have been remarkably deepened, the early stage environmental effects on galaxies are still very poorly understood. Rather, many recent studies have reported no clear trends of changing galaxy properties as a function of overdensities at high redshifts (e.g. Kacprzak et al. 2015; Kewley et al. 2016; Dey et al. 2016), and the environmental effects would be thought to be negligible or very small at such high redshifts. However, the past results are sometimes inconsistent due for example to different protocluster samples, some of which are not even clear if they are truly “protoclusters". In fact, we should admit that the definition of protoclusters is quite vague, and is different from one study to another. Furthermore, different observations and galaxy selection techniques also cause some systematic uncertainties and sampling biases, which may lead to different conclusions.

1.4.1 MAHALO-DEEP survey

With these background in mind, this *Thesis* aims to tackle this challenge and investigate the early environmental effects based on the unique samples of Hα-emitting galaxies associated with the two massive protoclusters at $z > 2$. The Hα line is the most luminous emission line in the spectra of typical star-forming galaxies, and is known to be associated with relatively unbiased and less dust attenuated tracer of star-formation activity compared

to other emission lines and UV lights. Therefore, deep narrowband imaging survey of Hα line emitters can provide us with the highest sampling density of star-forming galaxies in protoclusters, enabling us to conduct the most robust case studies ever. Moreover, the deep survey allows us to detect low-mass star-forming systems, which would be more susceptible to environmental effects by surrounding matters. This may help us obtain a concrete picture of the connection between galaxy formation and the cluster growth or formation.

Besides, including the MAHALO-Subaru, many intensive surveys by lots of research groups have investigated high-z galaxies in overdense environments to know how the cluster galaxies today are formed and evolved, and how they are affected by the surrounding environments. Such modern high-z galaxy surveys have focused on massive, passively evolving and star-forming galaxies. Since they are thought to be ancestors of even more massive systems ($> 10^{11}$ $M_\odot$) in the local Universe, those would provide us with insights into physical origin of high fraction of slow rotators in galaxy cluster cores (kinematic morphology–density relation, Cappellari et al. 2011). On the other front, the characteristics of low-mass galaxies ($\lesssim 10^9$ $M_\odot$) have been less understood despite of their obvious importance as the building blocks of today's L*-type galaxies at $z > 2$, according to the abundance matching and the evolutionary tracking of star-forming main sequence (Behroozi et al., 2013b; Tomczak et al., 2016; Shimakawa et al., 2016). Therefore, they are likely to be holding the keys to resolve formation mechanisms of our Galaxy as well. In addition to that, low-mass satellites should be more susceptible to environmental harassment by massive host systems (Ellison et al., 2009; Peng et al., 2010b; Kauffmann et al., 2013; Shimakawa et al., 2015a) and would eventually grow into the red sequence galaxies preferentially seen in the present-day massive clusters.

To break these situations, we have recently conducted MAHALO-DEEP protocluster/field survey (S15A047; S16B081; Kodama et al.) as the deeper extensions of our previous successful program, MAHALO-Subaru. The targets include very massive protoclusters, PKS 1138 and USS 1558, and some random fields, such as GOODS-South-CANDELS and COSMOS-CANDELS fields for comparison. This deep narrowband imaging survey is motivated to study the following subjects.

Identification of substructures by deep sampling: Narrowband observation has a great advantage of mapping substructures associated with protoclusters, since this allows us to comprehensively search for star-forming cluster members down to a certain flux limit. The past shallower imaging surveys have successfully identified internal structures of the two protoclusters (Koyama et al., 2013a; Hayashi et al., 2012). The deeper narrowband imaging will enable us not only to confirm those structures but also find more detailed substructures by many more galaxies.

Low-mass galaxies in the protoclusters: Deeper narrowband imaging allows us to reach and explore lower-mass galaxies because of the relationship between stellar mass and SFRs (Hα) (the star-forming main sequence) (Daddi et al., 2007a; Elbaz et al., 2007; Noeske et al., 2007). Low-mass systems are more likely to be affected by the environmental impacts. If true, we may be able to see more environmental dependences in such low-mass galaxies. Cooke et al. (2014) have argued a lack of star-forming galaxies in a $z = 2.5$ protocluster region MRC 2104 based on the narrowband

Hα search, which may be attributed to higher amount of dust extinction and/or earlier galaxy formation in dense regions. However, their argument is based on the shallow imaging data ($NB_{3\sigma}$ = 21.4 and $Ks_{3\sigma}$ = 24.0), and thus their results should be taken with a caution. The deep survey also enables us to establish a statistical sample of dual Lyα and Hα emitters in the over-density regions for the first time, since LAEs tend to be younger, less-massive galaxies (Gawiser et al., 2006; Nilsson et al., 2007; Ouchi et al., 2008; Guaita et al., 2011). Such a statistical sample allows us to study environmental dependence of the escape fraction of Lyα photons for the first time.

Faint end of the star-forming main-sequence: While the values of slope and scatter of the star-forming main sequence have been measured by recent studies out to high redshifts (Santini et al., 2014; Skelton et al., 2014; Shivaei et al., 2015; Tomczak et al., 2016), low-mass end of the star-forming main sequence of star-forming galaxies is still largely unexplored. Recent deep Lyα line imaging surveys have reported the consistency of the slope of the main-sequence towards low-mass at least down to 10^8 $M_\odot$ (Shimakawa et al., 2016). However, it is quite important to test this result by using non-LAEs since LAEs would be in a specific phase of galaxy formation as repeatedly noted in the literature. In addition to that, investigating the low-mass end of the main sequence of protocluster galaxies is interesting. Since less-massive systems in dense environments should have higher chance of interactions with other baryonic matters (galaxies and intergalactic/intercluster medium) and/or dark matters in the massive haloes, the star-formation histories are expected to be affected by some external environmental processes such as gas stripping, tidal interactions and gas evaporations (Fujita, 2004; Jaffé et al., 2015; Bekki, 2014; Koyama et al., 2014). We would expect to see larger scatter of the main sequence, or higher fraction of outliers from the main sequence in the protoclusters. In the current datasets, although both the protocluster HAEs and the field ones follow more or less the same main sequence, there is a hint of environmental dependence that more emitters in PKS 1138 are up-scattered from the main-sequence (Koyama et al., 2013a,b). Such a possible boost of star formation in protoclusters is also predicted by a cosmological simulation (Genel et al., 2014). It may be more visible below $\sim 5\times10^9$ $M_\odot$ if we take into account the stellar mass function, although the current data become incomplete rapidly at this depth. MAHALO-DEEP imaging will thus make this intriguing unconfirmed trend much clearer. Together with the morphological information by HST as demonstrated by Wuyts et al. (2011); Whitaker et al. (2015), we can address the physical origin of the possible boost of star-formation.

Spatially extended Hα emission: It is quite intriguing but challenging to search for spatially extended (> 10 kpc) Hα emission, i.e., Hα blobs. It requires the imaging data as deep as possible in order to overcome the cosmological dimming effect of diffuse extended emission. In particular, we will explore deeper extended Hα haloes in the RGs that are already showing jet-like extended Hα emissions as discovered by the previous shallower data (Hayashi et al., 2012). Moreover, both of the RGs are known to have very extended Lyα haloes (Carilli et al., 2002; Villar-Martín et al., 2007). These are likely to be the sites of feedback in action where ionized gas is blown out due probably to strong energy input by central AGNs. Direct measurements of the spatial extent of Hα emission by deep Hα image will help us to investigate ionisation

fields caused by galaxy feedback, and possible connection between the AGNs and the surrounding protocluster members. Also, deep Hα imaging may detect other Hα blobs or diffuse Hα emission.

In short, the MAHALO-DEEP Hα imaging has a great potential to study possible biased star-formation histories of young, low-mass star-forming galaxies in the dense protoclusters at $z > 2$. This provides us with new insights into the physical origins of the environmental dependence of the present-day L*-type galaxies in the local massive galaxy clusters. The previous studies can address only the formation of massive galaxies. Also, the deeper Hα survey has a higher chance of detecting extended Hα emission which are good candidates for gas outflowing galaxies under strong feedback.

1.4.2 Dual Hα and Lyα imaging

The observational limitation due to the Earth's atmosphere has created a big gulf between high-z galaxy surveys at $z < 2.6$ and those at $z > 2.6$. Especially, commonly-used star-formation tracer, H$\alpha\lambda$6565 emission line is no longer observable from ground-based telescopes at redshifts greater than 2.6, and thus, the Ly$\alpha\lambda$1216 line has been used as alternative tracer of star-forming galaxies wherever we observe (e.g. Ouchi et al. 2003; Venemans et al. 2007; Dey et al. 2016).

However, everyone knows that only a small fraction (~ 10 %) of star-forming galaxies show detectable Lyα emission lines (Hayes et al., 2010; Matthee et al., 2016; Hathi et al., 2016). Even worse, the environmental effects on escape fractions of Lyα photon has not been explored so far. In particular, gaseous conditions of CGM in young protocluster cores are expected to be different from those of well-known hot cores in massive mature clusters at low redshifts (Dekel et al., 2009a,b; van de Voort et al., 2011). Since high-z protoclusters are still associated with large amounts of cold gas media, cooling time-scale would be much shorter than dynamical time, which leads vigorous cold gas streams towards protocluster cores. Thus, the large amounts of inflowing HI gas with high column density (van de Voort et al., 2011) may prevent Lyα photons from galaxies from escaping from protocluster haloes. Based on these circumstances, study for the dependence of physical properties and the selection effects of Lyα emitters (LAEs) in high-z dense protoclusters is highly desirable. Thus, we have carried out dual Hα and Lyα line imaging survey for the same protocluster field, USS 1558 at $z = 2.53$. The main goals are described in the following.

Comaparison between LAEs and HAEs: The dual emitter surveys of HAEs and LAEs for the protoclusters at $z = 2.1$–2.6 where both Hα and Lyα lines are observable, is crucial to test the Lyα selection effect for high-z protocluster search. By comparing spatial distribution of HAEs with that of LAEs, this *Thesis* explores influence of the selection bias of LAEs to the protocluster searches at high redshifts, which should provide us with important insights into the past and future high-z protocluster surveys using LAEs as tracers.

Environmental dependence of Lyα photon escape fraction: Local massive galaxy clusters contain lots of passive, very massive galaxies as seen in the bright end of the red sequence (Visvanathan & Sandage, 1977; Gladders & Yee, 2000). Those are thought to be formed at the redshift greater than two (Kodama et al., 2007). Indeed, we see many

massive red star-forming galaxies in the protoclusters at $z \gtrsim 2$ (e.g. Hayashi et al. 2012; Koyama et al. 2013a). Judging from these contexts, young protocluster circumstances at high redshift need to be supported by rich cold gas inflows (Dekel et al., 2009a,b) to form massive galaxies seen in the local Universe. So far, however, there is no evidence showing presence of rich cold gas medium in massive protoclsuter cores. With this motivation, we for the first time investigate the environmental dependence of the escape fractions of Lyα photons of protocluster galaxies. The Lyα photon escape fraction is defined by the ratio of observed Lyα flux to dust-corrected Hα flux, which can inform us of how large amounts of Lyα photons have been absorbed from galaxies by intervening HI clouds or dust along the line of sight (Hayes et al., 2010; Matthee et al., 2016). Therefore, this analysis would be able to constrain the environmental dependence of the amount of dense cold gas.

1.4.3 Two very massive structures, PKS 1138 and USS 1558

Here we introduce two great targets for our purposes, PKS 1138 and USS 1558 protoclusters identified by our past narrowband and spectroscopic studies.

PKS 1138 : PKS 1138 is among the most familiar protoclusters at $z \sim 2$ ever investigated by many researchers (Pentericci et al., 1997; Carilli et al., 1998; Kurk et al., 2000; Pentericci et al., 2000; Carilli et al., 2002; Kurk et al., 2004a,b; Croft et al., 2005; Venemans et al., 2007; Hatch et al., 2009; Doherty et al., 2010; Ogle et al., 2012; Kodama et al., 2013; Koyama et al., 2013a,b; Tanaka et al., 2013b; Shimakawa et al., 2014; Dannerbauer et al., 2014; Shimakawa et al., 2015a). In particular, the spatial distribution of HAEs reveal its filamentary structures (Fig. 1.3), which consist of the X-shape structure over a 60 square co-moving Mpc, and a large void region towards the south (Koyama et al., 2013a). In the crossroad right at the centre is the radio galaxy (RG) known as the "Spiderweb" galaxy that has a unique web-like morphology in the rest-frame UV image by ACS/HST. The spectroscopic redshift distributions of the HAEs and the LAEs suggest that the vicinities of the RG seem to be relatively well mixed in velocity space, whilst the outer regions are more structured in velocity along the filaments (Shimakawa et al., 2014). Their perfect alignment in 3-D toward the RG at $z = 2.16$, suggest that those galaxies are falling along the filaments towards the protocluster core centred on the RG. All those spatial and velocity structures in the density peak may suggest that the inner part of the protocluster core (< 0.5 Mpc on the physical scale) is already collapsed and nearly virialised, while the outer regions are still in the early phase of galaxy assembly towards the core. If we assume a kinematic virialisation in the core, the dynamical mass of the core is estimated to be 1.71×10^{14} $M_\odot$ according to the velocity dispersion of 683 km s^{-1} within the core and the prescription given in Finn et al. (2005). This seems to be consistent with the X-ray observation with the High Resolution Imager on ROSAT, which shows the emitted energy is $6.7 \pm 1.3 \times 10^{44}$ erg s^{-1} in the core at the 2–10 keV band, corresponding to the dynamical mass of $\sim 10^{14}$ $M_\odot$. However, it is still unclear whether or not the protocluster core is virialised and also there are a lot of contaminations in the X-ray emission from AGN (Carilli et al., 1998; Pentericci et al., 2002).

The central core is composed of both many red passively evolving galaxies and

many star-forming galaxies (Tanaka et al., 2013b; Koyama et al., 2013a), which is surprisingly dense compared to the random fields (Kodama et al., 2013; Koyama et al., 2013a). The overdensity of red passively evolving galaxies suggests that the star-formation activities in some of the galaxies in the protocluster core are already quenched as seen in massive clusters at lower redshifts. At the same time, however, we see starbursting galaxies traced by the red HAEs detected at 24 μm with MIPS/Spitzer (Koyama et al., 2013a) and/or 870 μm with LABOCA on APEX (Dannerbauer et al., 2014). Some of them show diffuse morphologies in their ACS images (Koyama et al., 2013a), suggesting that they are in the phase of dusty starburst triggered by galaxy-galaxy mergers. On top of that, Pentericci et al. (2002) have reported an excess of soft X-ray sources in this field. Also, additional five candidates of Seyfert AGNs are identified by our study on the BPT diagram (Shimakawa et al., 2015a). Therefore, various populations (passive galaxies, dusty starbursts, and AGNs) are mixed together in PKS 1138. It remains unclear so far, however, if those populations are related to some environmental effects.

Intriguingly, we see the enhanced gas-phase metallicities in the less massive HAEs in PKS 1138 (Shimakawa et al., 2015a). The upward offset from the M–Z relation in the random fields (Erb et al., 2006a) is the order of 0.15–0.20 dex at the stellar mass of $\lesssim 10^{10}$ $M_{\odot}$ (Fig. 1.4). We must note that the comparison sample of Erb et al. (2006a) is based on the UV-selected galaxies (Adelberger et al., 2004; Steidel et al., 2004). However, the metallicity offset remains consistently even if we compare with the NIR magnitude selected (HST F160W-band) star-forming galaxies (Sanders et al., 2015), which are more comparable to our Hα-selected samples together with the NIR data. The enhanced chemical enrichment seen in the protocluster galaxies should mean that the past histories of star-formation and gas inflow and outflow are different from those of galaxies in the general field at the same redshift. It should be noted that we have excluded the AGN contamination by the BPT diagram (Kewley et al., 2013b,a) and the X-ray data (Pentericci et al., 2002). Three possible scenarios are considered here to account for the metallicity enhancement; (1) gaseous recycling of chemically enriched gas (Oppenheimer & Davé, 2008; Davé et al., 2011; Kulas et al., 2013), (2) stripping of metal poor gas in the reservoir (Hughes et al., 2013; Bahe et al., 2016), (3) earlier, accelerated galaxy evolution in dense environments (Thomas et al., 2005; Genel, 2016). However, we have not yet reached to any conclusive view. The successful model should also account for the absent of the environmental dependence (in the offset direction) of the star-forming main-sequence (Koyama et al., 2013b). Moreover, it is still highly controversial whether the chemical enrichment in cluster galaxies have proceeded further than those in the general field (Kulas et al., 2013; Valentino et al., 2015; Kacprzak et al., 2015). Further investigations and other approaches both observationally and theoretically, are required.

USS 1558 : USS 1558 was first discovered by its large overdensity in red galaxies associated to the radio galaxy (Kajisawa et al., 2006; Kodama et al., 2007), and it was successively identified as the strong overdensity of the associated star-forming galaxies as well (Hayashi et al., 2012). Now this object can be regarded as the densest protocluster ever discovered to date at $z > 2$, by more than ~ 2 times denser than any other known clusters/protoclusters such as PKS 118 (Kurk et al., 2000; Koyama et al., 2013a);

SSA22 at $z = 3.1$ (Steidel et al., 1998; Kubo et al., 2015); 4C23.56 at $z = 2.5$ (Tanaka et al., 2011); 2QZ at $z = 2.3$ (Matsuda et al., 2011b; Kato et al., 2016); Cl J1449+0856 at $z = 2.0$ (Gobat et al., 2013; Valentino et al., 2015); COSMOS-ZFOURGE at $z = 2.1$ (Yuan et al., 2014; Kacprzak et al., 2015); COSMOS-UVISTA at $z = 2.4$ (Chiang et al., 2014, 2015). The overdensity is such that the mean separation of HAEs at the density peak is only 150 kpc in 3-D on the physical scale. Three dense groups of HAEs are identified by Hayashi et al. (2012) which align in the NW-SE directions: a loose group around the RG associated with six distant red galaxies (DRGs), the richest clump at 3.5 arcmin away from the RG containing 20 HAEs within 1.64 square arcmin, and a small clump in between the two. These are also well aligned along the line of sight according to the spectroscopic data (Shimakawa et al., 2014). Shimakawa et al. (2014) have revised these three groups to two clumps C1 and C2 because of the poor kinematic separation between the latter two clumps (Fig. 1.3). We have spectroscopically confirmed 19 HAEs in the densest group and we have 12 more candidates which are not confirmed yet. Although it is unsure if these massive systems are already virialised, we have estimated the dynamical masses (R200) of C1 and C2 assuming the local virialisation, and obtained 0.10×10^{14} and 0.87×10^{14} $M_{\odot}$ from their velocity dispersions of 284 and 574 km s^{-1}, respectively (Shimakawa et al., 2014) following the Finn et al. (2005) prescription. These groups will very likely to eventually merge together and become a single rich galaxy cluster in the future.

The dense HAE groups in USS 1558 seem to be different evolutionary stage as compared to PKS 1138 in the sense that blue HAEs are dominant in those region (Hayashi et al., 2012) while the density peak of PKS 1138 are dominated by DRG and red HAEs as described above. This may suggest that the large amount of circumgalactic medium (HI; CGM) remains in dense groups and the cold accretion is still prevalent in these regions (Dekel et al., 2009a,b). The sufficient gas reservoirs feed the fresh gas into resident galaxies (Dekel et al., 2009a,b) and thus those can form stars intensively as detected by Hα emission lines. Indeed, we cannot see a clear red sequence in USS 1558 (Kodama et al., 2013), and also there is no excess of massive HAEs differently from PKS 1138 (Koyama et al., 2013a). Thus, USS 1558 protocluster is more likely to be in a young phase of galaxy cluster formation.

Our previous near-infrared spectroscopy with MOIRCS and MOSFIRE (Shimakawa et al., 2015a,b) have successfully identified hydrogen Balmer lines (Hα, Hβ) and high-ionisation oxygen lines [OIII]. Interestingly, their [OIII] line fluxes are comparable to or larger than Hα line fluxes, suggesting that they tend to have higher ionisation parameters and harder radiation fields than low-z star-forming galaxies. Such a trend is now well established by large intensive projects such as KBSS-MOSFIRE (Steidel et al., 2014), MOSDEF (Kriek et al., 2014), and ZFIRE (Nanayakkara et al., 2016) with MOSFIRE on Keck. The right-upward offset of the chemical abundance sequence on the BPT diagram of our HAEs in the protoclusters are consistent with the typical star-forming galaxies at the similar redshifts (Shimakawa et al., 2015a). Shimakawa et al. (2015b) also succeeded in measuring the electron densities of HAEs in USS 1558, which was the first trial of the direct, systematic measurements of electron densities at $z > 2$. We have found that high-z star-forming galaxies tend to have by an order of magnitude higher electron densities than local galaxies. On the other hand, we do

not see any environmental dependence of electron densities among galaxies at $z > 2$ (Sanders et al., 2016).

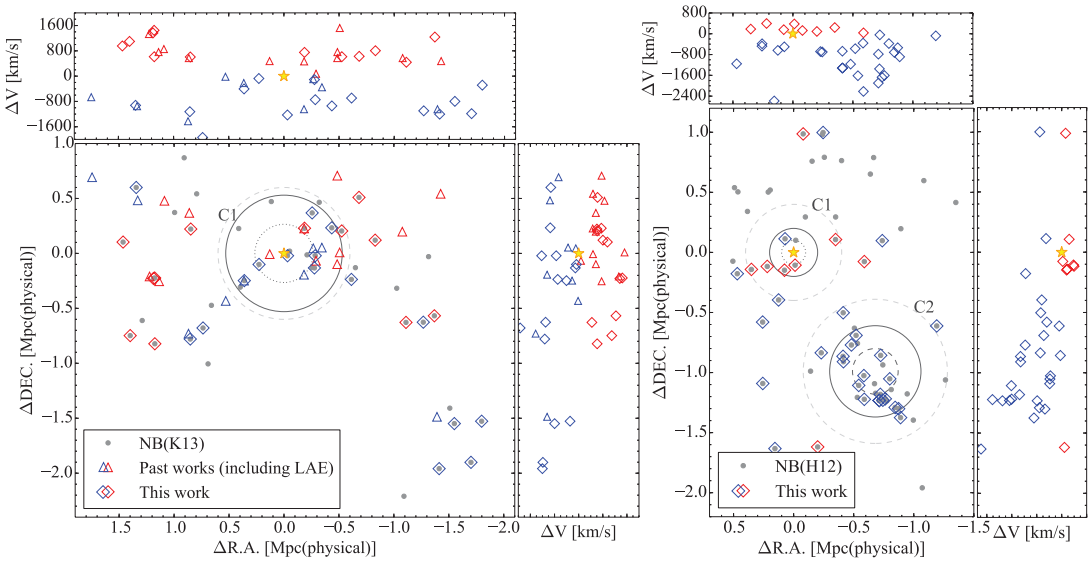

Figure 1.3: The massive protoclusters, PKS 1138 on the left and USS 1558 on the right (Figure 2 in Shimakawa et al. 2014). Grey points are HAE candidates discovered by the past narrowband imaging (Hayashi et al., 2012; Koyama et al., 2013a). Open diamonds represent the cluster members that are spectroscopically confirmed by Shimakawa et al. (2014). In the left panel, triangles are the confirmed Hα and Lyα emitters in the previous work (see the literature). Blue and red symbols are separated by blue- and redshifted galaxies, respectively, with respect to the RGs (star symbols). Shimakawa et al. (2014) define three groups, PKS 1138-C1, USS 1558-C1 and USS 1558-C2 as indicated by grey dashed circles. Solid and dotted black circles show R200 and 0.5×R200, respectively.

1.4.4 Thesis outline

The *Thesis* consists of the following parts: details of our projects, observations, data analyses and selection methods (§2), spatial distributions of the obtained protocluster members and Hα line morphology of bright radio galaxies (§3), comparison of physical properties of star-forming galaxies across environments (§4), discussion and conclusions of our results (§5), and our future prospects (§6).

We assume cosmological parameters of Ω_M=0.3, Ω_Λ=0.7 and H_0=70 km s^{-1}Mpc^{-1} and employ a Chabrier (2003) stellar initial mass function (IMF). The AB magnitude system (Oke & Gunn, 1983) is used throughout this *Thesis*.

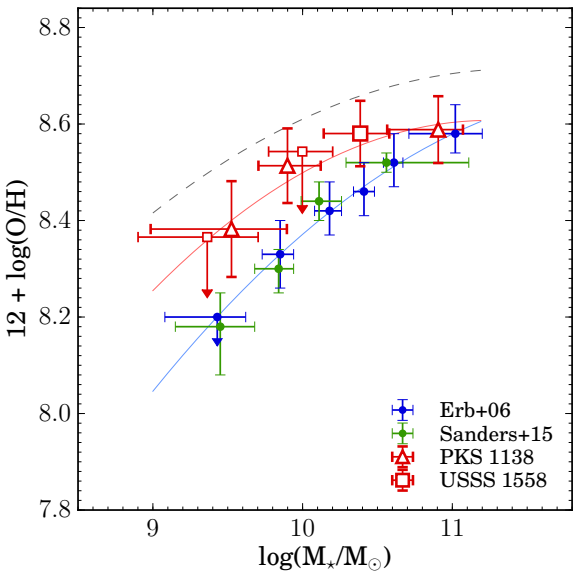

Figure 1.4: Stellar mass versus gaseous metallicity diagram, revised from Figure 6 in Shimakawa et al. (2015a). Red triangles, red squares, blue dots, green dots indicate HAEs in PKS 1138, USS 1558, UV-selected galaxies (Erb et al., 2006a), and F160W-band magnitude selected star-forming galaxies (Sanders et al., 2015) at z = 2–2.6, respectively. Those gas-phase metallicities are derived from the Pettini & Pagel (2004) prescription (so-called N2 index), which uses [NII]/ Hα line ratio. While the errorbars in Shimakawa et al. (2015a); Erb et al. (2006a) show 1σ scatters in stellar mass and 1σ flux errors in the metallicities, the errorbars of Sanders et al. (2015) show the ranges of each stellar mass bin. The red and blue curves are the best-fitting curves for Shimakawa et al. (2015a); Erb et al. (2006a), respectively. The dashed curve is the median of the M–Z relation for the galaxies at $z \sim 0.1$ with $\mathrm{EW}_{\mathrm{H}\alpha} > 20$ Å based on the SDSS sample (Abazajian et al., 2009).

2 | Data and analyses

Over the two decades, a number of high redshift protocluster searches have been carried out by many research groups (Steidel et al., 1998; Shimasaku et al., 2003; Miley et al., 2004; Kajisawa et al., 2006; Overzier et al., 2008; Mayo et al., 2012; Hatch et al., 2014; Toshikawa et al., 2012; Wylezalek et al., 2013; Chiang et al., 2015; Toshikawa et al., 2016). Among them, *narrowband technique* is one of the most effective tools that allows us to comprehensively trace star-forming objects associated with overdense regions down to a certain limits in line flux and its equivalent width, such as Ly$\alpha\lambda$1216 (Kurk et al., 2000; Venemans et al., 2002, 2005; Ouchi et al., 2005; Venemans et al., 2007; Yamada et al., 2012; Wylezalek et al., 2013; Lee et al., 2014c; Dey et al., 2016) and H$\alpha\lambda$6565 lines (Kurk et al., 2004a; Tanaka et al., 2011; Hayashi et al., 2012; Koyama et al., 2013a; Cooke et al., 2014). This section describes the datasets, and our improved selection method of line emitting galaxies.

2.1 Archive data and update

This work employs the multi-broadband datasets and deep composite narrowband images in combination with the early data taken by MAHALO-Subaru survey (S10B-028, Kodama et al.), the new data by MAHALO-DEEP survey (S15A-047, Kodama et al.), and collaborations with the other research groups. The broadband data are mainly collected by the past MAHALO-Subaru campaign (z, J, Ks for PKS 1138 and B, r, z, J, H, Ks for USS 1558), which are already published by Koyama et al. (2013a) for PKS 1138 and Hayashi et al. (2012) for USS 1558, respectively. In the PKS 1138 region, B-band data with FORS1 and r, i-band images with FORS2 on the Very Large Telescope (VLT) are distributed by Kurk et al. (2000, 2004a) in private communication. H. Dannerbauer in University of Vienna and N. Hatch in University of Nottingham kindly provided us with deep near-infrared data at Y, H, Ks-bands for PKS 1138 taken by HAWK-I on the VLT. In addition to that, spatially-resolved ACS and WFC3 images by the Hubble Space Telescope (HST) are available in both protocluster fields (F814W, F160W in PKS 1138 by Miley et al. 2006, and F814W, F160W in USS 1558 by Hayashi et al. 2016). Those space-base data are deep enough to constrain photometries of narrowband emitters and thus we also use these data. All broadband images are carefully reduced by primary investigators in the literatures based on the reduction pipelines optimised for each science image. Seeing size and limiting magnitudes of the reduced data are summarised in Table 2.1.

Then, we here summarise information of the recent deeper imaging with narrowband and broadband with MOIRCS on the Subaru Telescope executed during April 30 and May 6, 2015. In this observing run, we mainly focused on narrowband imaging with NB2071

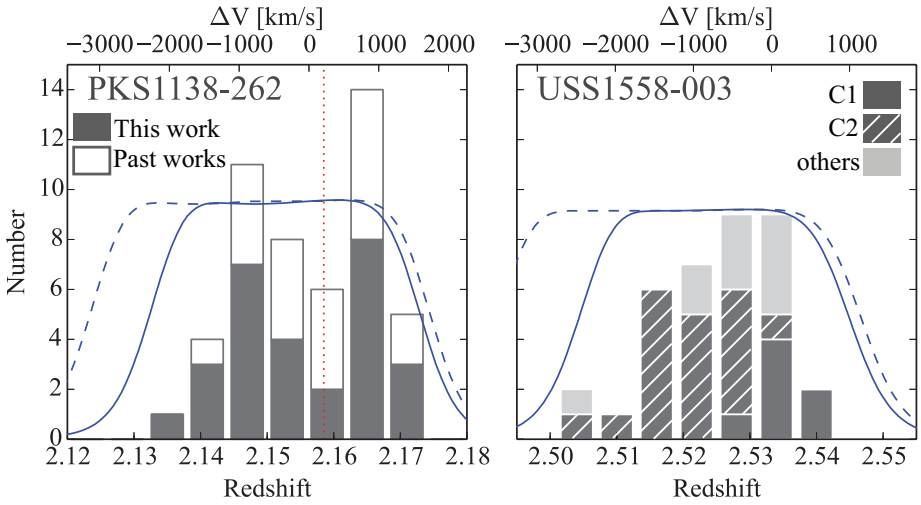

Figure 2.1: Redshift distributions of spectroscopically-confirmed members in PKS 1138 (left) and USS 1558 (right) given by Shimakawa et al. (2014). The bin size is $\delta z = 0.006$ in both panels. All colour-filled histograms are based on the MOIRCS/Subaru spectroscopy. X-axis on the upper side shows peculiar velocities with respect to the RGs (ΔV). Blue solid curves correspond to the filter response curve of each narrowband filter, NB2071 and NB2315. Blue dashed curves indicate the reachable redshift range by wavelength shifts of the transmission curves within the FoV (Tanaka et al., 2011). In PKS 1138, protocluster members identified by other past studies (Kurk et al., 2000, 2004b; Croft et al., 2005; Doherty et al., 2010) are also presented by the opened histogram. There is a strong OH line at $\lambda = 2.073$ nm, which would affect redshift confirmation for HAEs in PKS 1138 (see Shimakawa et al. 2014). In USS 1558, black solid, slashed and grey solid histograms show the galaxies in clumps 1, 2 and outside them in the protocluster (Fig. 1.3), respectively. The top axis shows peculiar velocities with respect to each RG.

($\lambda_{\rm center}$ = 2.071 μm, FWHM= 270 Å) and NB2315 ($\lambda_{\rm center}$ = 2.315 μm, FWHM= 260 Å) that can capture Hα emission line of star-forming galaxies associated with PKS 1138 and USS 1558, respectively (Fig. 2.1). The observation was carried out under a photometric condition and a seeing condition of FWHM < 0.7 arcsec. Integration times of the additional observations were 125 and 380 min at NB2071 and NB2315, respectively, which were split to 180 sec individual exposures. In addition to that, we took further J (116 min) and Ks (150 min) imaging for USS 1558. Combined with our previous data, deeper NB2071 image for PKS 1138 and deeper J, Ks, and NB2315 images for USS 1558 have been reconstructed by this observation. The total integration times are now 311 (NB2071), 191 (J), 207 (Ks), and 583 (NB2315) min, respectively.

All the data taken by this new observation were reduced in a standard manner using the reduction pipeline MCSRED[1] made by I. Tanaka at Subaru telescope (Tanaka et al., 2011) that is composed of IRAF[2] script. The reduction procedures include flat fielding (self flat for broadbands and dome flat for narrowbands; see details in Tanaka et al. 2011), masking objects from the science data (thus pipeline process are conducted at least twice), sky subtraction, distortion correction, cross checking, and image mosaicing. Those processes can be executed automatically. We eventually obtain updated deeper image in NB2071 ($\rm NB_{3\sigma}$ = 24.15 with 0.63 arcsec seeing) for PKS 1138 and deeper J, Ks, and NB2315 images

($J_{3\sigma}$ = 25.30, $Ks_{3\sigma}$ = 24.96, and $NB_{3\sigma}$ = 24.29 with 0.63 arcsec seeing) for USS 1558.

Table 2.1 summarise data qualities of all narrowband and broadband datasets relevant to this *thesis*. We also have Lyα line image for USS 1558, which is explained in §2.4.3. Galactic extinctions are based on the Fitzpatrick (1999) extinction law with R_V = 3.1 and the dust reddening, E(B–V) = 0.0343 (PKS 1138) and 0.1339 mag (USS 1558) from Schlafly & Finkbeiner (2011).

[1] http://www.naoj.org/staff/ichi/MCSRED/mcsred.html
[2] http://iraf.noao.edu

Table 2.1: Data summary for PKS 1138−262 (upper table) and USS 1558−003 (lower table). The first to fourth columns indicate filter name, filter centre wavelength, filter FWHM, and zero point magnitude, respectively. The fifth column shows aperture size for colour measurements (see §2.4.2) in diameter. The limiting magnitude of three sigma for each filter is represented in the sixth column. The seventh column shows the amount of galactic extinction derived from the Fitzpatrick (1999) extinction law and the dust reddening, E(B−V) by Schlafly & Finkbeiner (2011). Ks and Kv are Ks-bands by the MOIRCS/Subaru and HAWK-I/VLT, respectively. F475W and F814W images in PKS 1138 have deeper area in the centre (27.88 and 27.38 in three sigma limiting magnitude, respectively).

PKS 1138

Band	λ_{center} (μm)	FWHM (arcsec)	ZP (AB)	Aperture (arcsec)	3σ Depth (AB)	A_λ (mag)
NB	2.07	0.63	23.839	1.3	24.15	0.01
Ks	2.15	0.63	26.244	1.3	24.13	0.01
Kv	2.15	0.38	27.356	1.2	24.81	0.01
H	1.62	0.49	27.708	1.2	25.28	0.02
J	1.25	0.63	31.481	1.3	24.50	0.03
Y	1.02	0.37	26.719	1.2	26.43	0.04
z	0.91	0.70	33.409	1.3	26.53	0.05
F814W	0.81	0.11	25.937	1.1	26.97	0.06
i	0.79	0.70	26.61	1.3	26.41	0.06
r	0.65	0.94	27.09	1.4	26.28	0.08
F475W	0.47	0.11	26.068	1.1	27.46	0.13
B	0.43	0.80	26.59	1.4	26.81	0.14

USS 1558

Band	λ_{center} (μm)	FWHM (arcsec)	ZP (AB)	Aperture (arcsec)	3σ Depth (AB)	A_λ (mag)
NB	2.32	0.63	23.692	1.3	24.29	0.05
Ks	2.15	0.63	25.555	1.3	24.96	0.05
H	1.64	0.66	26.857	1.3	24.23	0.07
F160W	1.54	0.19	25.946	1.1	26.45	0.08
J	1.25	0.63	26.357	1.3	25.30	0.11
z	0.91	0.66	33.239	1.3	26.46	0.19
F814W	0.81	0.11	25.947	1.1	25.86	0.24
r	0.63	0.64	34.541	1.3	27.60	0.35
B	0.45	0.68	33.785	1.3	27.90	0.55
NB428	0.43	1.25	30.870	2.5	26.26	0.57

2.2 Other relevant datasets

Since these two protoclusters are particularly unique, super-massive structures discovered to date, we are best positioned to conduct the environmental study and provide unique insights into the early environmental effects on star-formation activities in the tempestuous period of cluster formation ($2 < z < 3$). For this purpose, we have intensively accumulated unique data-sets on the two targets.

We have obtained spatially resolved images in the rest-frame UV and optical by WFC3 and ACS on the Hubble Space Telescope (HST). F475W and F814W data of 1.1 arcsec seeing are already available in 5.6×3.5 square arcmin field of PFS 1138. F814W and F160W imaging was conducted by Hayashi et al. (2016) which fully covers the three dense clumps in USS 1558 discovered by Hayashi et al. (2012). We have also conducted high resolution narrowband Hα imaging with the InfraRed Camera and Spectrograph (IRCS) assisted by AO118 (Kobayashi et al., 2000; Hayano et al., 2010; Minowa et al., 2010) to obtain spatially-resolved Hα maps within individual galaxies located in the densest clump C2 of USS 1558 (Suzuki et al. in preparation) as a part of our systematic AO-assisted narrowband imaging survey called GANBA-Subaru (*Galaxy Anatomy with Narrow-Band AO-imaging with Subaru*) led by Minowa et al. (in preparation). These data allow us to resolve the internal structure of stellar mass and star-forming regions (Tadaki et al., 2014), which cannot be done with the natural seeing conditions of $\gtrsim 0.4$ arcsec at best (corresponding to ~ 3 kpc at $z = 2$–3).

Both protoclusters have been observed with ACIS-S (for PKS 1138) and ACIS-I (for USS 1558) detectors on the Chandra X-ray Observatory for 11 hrs and 28 hrs, which can constrain X-ray luminosities down to 1.5×10^{44} and 0.5×10^{44}, respectively. The x-ray data help us search for AGNs associated with the protoclusters (Pentericci et al. 2002 for PKS 1138; Martini et al. in preparation for USS 1558). In the submm–radio regime, we have deep 850 μm images down to ~ 1.5 mJy for both PKS 1138 and USS 1558 fields with SCUBA2 on JCMT (Kodama et al.). Also, CO_{J3-2} and dust continuum data (870 μm) are just obtained for the part of these regions with the Atacama Large Millimeter/submillimeter Array (ALMA), led by T. Kodama at NAOJ through the systematic ALMA survey project called GRACIAS-ALMA (*Galaxy Resolved Anatomy with CO Interferometry And Submm observations with ALMA*). Such data will be able to inform us of spatially-resolved dust-hidden star-formation and molecular gas content. The recent ALMA results suggest that star-formation is taking place in compact regions at galaxy centres at $z \sim 2$ (Barro et al., 2016; Tadaki et al., 2016).

12 out of 83 HAEs in the PKS 1138 protocluster have been observed with multi-object integral field spectroscopy, KMOS (the K-band Multi Object Spectrograph). This supplies us with three dimensional Hα data that are essential to resolve kinematics of star-forming regions of protocluster galaxies, and the measured spin parameters may provide us with the insights into how they fall into the protocluster core (Koyama et al. in preparation).

All these accumulating top quality data make these protoclusters exceptionally unique and ideal targets to test the effect of environment on the early stage of cluster galaxy formation. However, most of the data are still under analyses by the collaborators. Thus this *thesis* does not refer to these data unless otherwise mentioned.

2.3 Data analyses

2.3.1 Revisit of narrowband selection

The narrowband technique provides us with Hα emitter candidates at certain redshifts showing flux excesses in their narrowband images relative to those of counterpart broadband (Ks-band in this case). The significance of the excess of narrowband flux (Σ) is quantified by the excess of magnitude offset of NB-band from Ks-band (Ks–NB) with respect to the photometric 1-sigma error (σ) as a function of narrowband magnitude (Bunker et al., 1995). The equation can be described by,

$$\mathrm{Ks}-\mathrm{NB} = -2.5\log(1-\Sigma\delta 10^{-0.4(\mathrm{ZP}-\mathrm{NB})}) + \emptyset_{\mathrm{Ks-NB}} \tag{2.1}$$

where $\emptyset_{\mathrm{Ks-NB}}$ is correction factor of colour term. This value would not be zero if centre wavelength of a narrowband filter is different from that of a broadband, since galaxy spectra are not always flat as a function of frequency. What is especially important here is narrowband flux errors δ, which have been estimated in several ways so far. One is based on 1σ errors from random empty aperture with the fixed aperture size same as for photometry of science objects (in general $\sim 1.5-2.5\times$ seeing size is used, e.g., Hayashi et al. 2010; Koyama et al. 2010).

$$\delta = \sqrt{\sigma^2_{\mathrm{NB},S} + \sigma^2_{\mathrm{Ks},S}} \tag{2.2}$$

where S is aperture area. 1σ count errors, $\sigma_{\mathrm{filter},S}$ can be derived by traditional random empty aperture photometry. The other way would be errors from the rms values per pixel scaled by aperture area (e.g. Sobral et al. 2009, 2013), which is given by,

$$\delta = \sqrt{S(\sigma^2_{\mathrm{NB},1} + \sigma^2_{\mathrm{Ks},1})}. \tag{2.3}$$

This is grounded under the assumption that photometric aperture error is proportionate to square root of aperture area ($\sigma \propto \sqrt{S}$). In a practical sense, however, this is false (i.e. $S(\sigma^2_{\mathrm{NB},1} + \sigma^2_{\mathrm{Ks},1}) \neq {\sigma'_{\mathrm{NB},S}}^2 + {\sigma'_{\mathrm{Ks},S}}^2$) since the science images highly likely have pixel-to-pixel correlations (Skelton et al., 2014), which would be due to such contamination from very faint sources and local residuals of background subtraction. The pixel-to-pixel correlation can be quantified by random photometry with empty apertures of various pixel sizes. If there were no pixel-to-pixel correlation, a power-law index (N) in $\sigma \propto \sqrt{S}^N$ should be one, but if pixel-to-pixel were perfectly correlated within the aperture, the background noise would increase with aperture size as $N = 2$. Indeed, we found that all narrowband and broadband data used in this *thesis* have pixel-to-pixel correlations because power law functions of all science images show N values between 1 and 2. Figure 2.2 shows the examples of NB2071, NB2315, and Ks-band in both fields. The best-fitting curves by power law in those data show $1 < N < 2$ (Table 2.2), indicating that we cannot apply the equation 2.3 for our datasets.

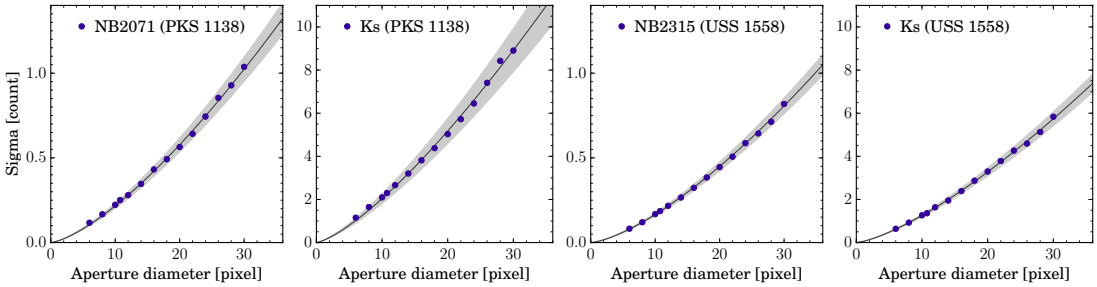

Figure 2.2: 1σ count errors as a function of aperture size in pixel at NB2071, Ks for PKS 1138, NB2315, and Ks for USS 1558 from left to right. Black curves show best-fitting curves. Grey regions correspond to 1σ scatters inferred from scatters of local background rms within the science images, which are dumped by the SExtractor. Pixel size in each image is 0.117 arcsec / pixel.

Table 2.2: Best-fitted power-low functions of random empty apertures with various aperture sizes ($\sigma = a\ D^N$). Errors of a show the local standard deviations compared to that in the entire region, corresponding to 0.06–0.12 mag variations in limiting magnitude.

Target	Filter	a (count)	N
PKS 1138	NB2071	0.0084 ± 0.00059	1.412
	Ks	0.0920 ± 0.01034	1.345
USS 1558	NB2315	0.0060 ± 0.00035	1.441
	Ks	0.0520 ± 0.00294	1.383

Secondly, estimation of narrowband excess so far is founded on fixed area of circular aperture, however, this should have some problems. Since galaxies do not always look perfectly round, circular aperture tend to probe empty pixel area more than necessary in which galaxy continuum does not appear. This leads us to overestimate background noise and then may miss HAEs strongly elongated. Furthermore, even within a narrow redshift slice, detectable HAEs have various sizes and luminosities. Therefore, sizes and luminosities of selected HAEs could be biased toward specific values of those sensitive to a certain aperture size. To overcome this problem, we conduct band photometries based on MAG_AUTO, i.e., aperture areas enclosed by those Kron ellipses in their narrowband images. This means that we can use more flexible photometric aperture optimized to each source. This improved technique enables more appropriate noise estimation and then would provide us with less-biased HAE samples. We tailor a error function to our photometry measurement, which is given by,

$$\delta(S) = \sqrt{\sigma_{\rm NB}(S)^2 + \sigma_{\rm Ks}(S)^2} \tag{2.4}$$

where $\sigma_{\rm NB}(S)$ and $\sigma_{\rm Ks}(S)$ are 1σ background errors within aperture area (S) at narrowband and broadband, respectively. We adapt the same aperture area S for noise estimation as those enclosed by the Kron Ellipse in the narrowband image for individual sources to evaluate the significance of their narrowband flux excess Σ. Standard deviation can be

rewritten by $\sigma = a\, D^N$. D is circularised aperture diameter in pixel ($D = 2 \times \sqrt{S/\pi}$) and a is a scaling factor. Table 2.2 summarises parameters of these functions.

2.3.2 Colour–magnitude diagram

Before executing narrowband selection, we quantified accurate zero point of Ks–NB i.e. correction factor of colour term ($\emptyset_{\mathrm{Ks-NB}}$). This procedure is important especially to minimise systematic error of NB flux estimation by two different narrowband filters (NB2071 and NB2315). We first investigated possible $\emptyset_{\mathrm{Ks-NB}}$ values by using model spectra distributed by Tremonti (2003). Figure 2.3 shows colour term distributions of Ks–NB2071 and Ks-NB2315 in single stellar population (SSP) synthesis models with various ages, 0.025, 0.1, 0.9, 2.5, and 11 Gyrs. Those metallicities are fixed to the solar abundance, they have no dust extinction, and nebular line components are not included. We also check the colour term distribution by other spectral models of constant star-formation histories with age of 6 Gyr and exponential declined tau (τ = 5, 9, and 12 Gyrs) models, and we then confirmed that those colour term distributions do not deviate from the range covered by five SSP models.

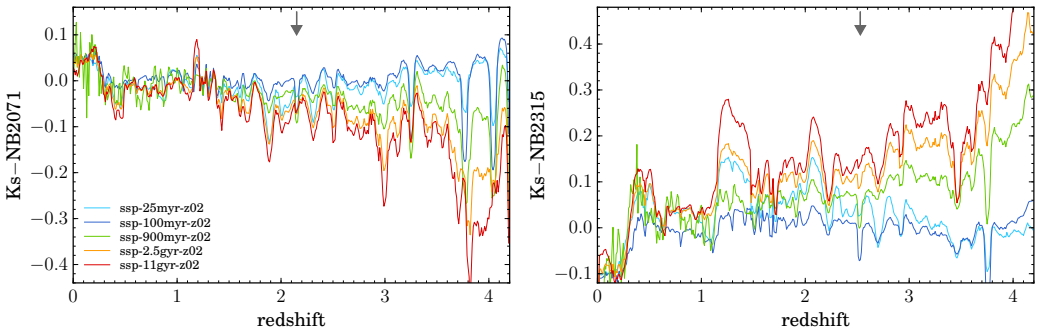

Figure 2.3: Colour term distributions of Ks–NB2071 and Ks-NB2315 in SSP models with various ages, 0.025, 0.1, 0.9, 2.5, and 11 Gyrs. Those metallicities are fixed to the solar abundance. Downward arrows indicate detectable Hα redshift by each narrowband.

Amount of dust extinction is also critical to determine the offset of narrowband magnitude from Ks-band. When we assume stellar extinction of $A_V = 1$, $\emptyset_{\mathrm{Ks-NB}}$ values decrease and increase by $\sim 0.05 - 0.10$ mag in NB2071 and NB2315, respectively (Fig. 2.4). After that, we evaluated typical $\emptyset_{\mathrm{Ks-NB}}$ points in each narrowband selection based on the spec-z sources by MOSDEF survey (Kriek et al., 2014). We derive the flux densities at the wavelength of each narrowband filter from the SED-inferred spectra based on the SED-fitting code of FAST, IDL-script pipeline (Kriek et al., 2009). Since those total fluxes are available in the large library, the 3D-HST catalogue (Skelton et al., 2014), we have just applied these photometry to the SED fitting. As a result, the MOSDEF samples at $z > 1$ well agree with the distribution from the simple model spectra, whilst we see some scatters for a given redshift. Median NB–Ks values of the MOSDEF samples are estimated to be $\emptyset_{\mathrm{Ks-NB2071}} = -0.03$ and $\emptyset_{\mathrm{Ks-NB2315}} = 0.07$. This work decided to use these values in the narrowband selection.

Since we obtained $\delta(S)$ and $\emptyset_{\mathrm{Ks-NB}}$ values by sophisticated analyses, now we can select narrowband emitters based on the equation 2.1. This work first computes Σ values for all sources. Then we employ HAE candidates showing more than 2.5Σ excesses in the

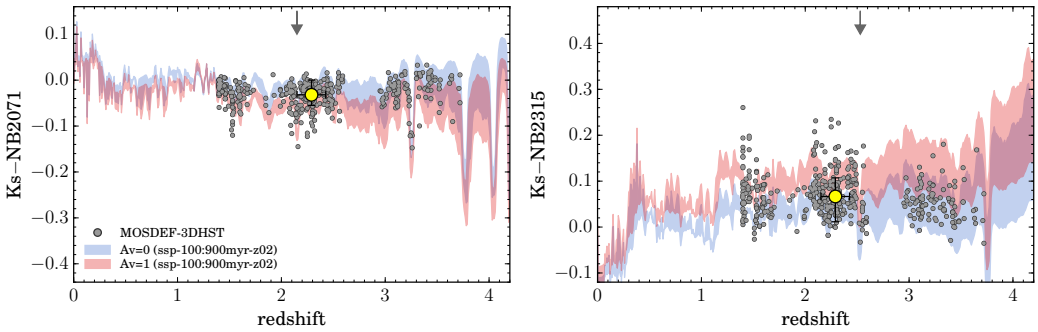

Figure 2.4: Same as Figure 2.3, but here uses SSP models with ages of 0.1 and 0.9 Gyrs, and those with extinction of $A_V = 1$. Grey circles show the colour term based on the SED of spec-z samples by MOSDEF (Kriek et al., 2014). Those median values and scatters are shown by yellow circles and errorbars.

narrowband fluxes and line equivalent widths (EWs) more than 30 Å in the rest frame (here assuming $z = 2.15$ for PKS 1138 and $z = 2.53$ for USS 1558, respectively). Narrowband line flux, line-subtracted flux density, and EW are calculated by the following formula,

$$F_{\rm NB} = \Delta_{\rm NB} \frac{f_{\rm NB} - f_{\rm Ks}}{1 - \epsilon \Delta_{\rm NB}/\Delta_{\rm Ks}}, \tag{2.5}$$

$$f_{\rm c} = \frac{f_{\rm Ks} - f_{\rm NB}\ \epsilon \Delta_{\rm NB}/\Delta_{\rm Ks}}{1 - \epsilon \Delta_{\rm NB}/\Delta_{\rm Ks}}, \tag{2.6}$$

$$\mathrm{EW}_{\rm NB,rest} = \frac{F_{\rm NB}}{f_{\rm c}} (1+z)^{-1}, \tag{2.7}$$

where ϵ is scaling factor adjusting coverage fraction between narrowband and broad-band. While Ks-band fully covers response curve of NB2071 (i.e. $\epsilon = 1$), NB2315 filter is out of the response curve of Ks-band ($\epsilon = 0$). According to the equation 2.7, EW thresholds of > 30 Å for PKS 1138 and USS 1558 are estimated to be Ks–NB2071 > 0.263 and Ks–NB2315 > 0.441, respectively.

With these criteria, we performed source detections for each field by using an astronomical software for the source extraction (SExtractor; Bertin & Arnouts 1996). The source photometry were executed with the double-image mode of the SExtractor with detection parameters of DETECT_MINAREA = 9, DETECT_THRESH = 1.2, ANALYSIS_THRESH = 1.2, and DEBLEN_MINCONT = 0.0001. We employ band photometries of MAG_AUTO read out by the SExtractor with photometry parameters of PHOTO_AUTOPARAMS = 1.0, 2.0 and PHOTO_AUTOAPERS = 8.1, 8.1 so that the Kron radii may not be so large and not too small. The input parameters for the source extraction are summarised in Table 2.3. As a result, we detect 16,096 and 17,348 sources in the narrowband images for PKS 1138 and USS 1558, respectively, where the outside edges or noisy regions are removed. Figure 2.5 shows the colour-magnitude diagram, NB vs. Ks–NB in PKS 1138 (left) and USS 1558 (right). Taking account of brighter objects tend to be located at lower redshifts, colour-term distributions

Table 2.3: SExtractor parameters.

Parameter	Input	Default
DETECT_MINAREA	9	—
DETECT_THRESH	1.2	—
ANALYSIS_THRESH	1.2	—
DEBLEND_NTHRESH	32	—
DEBLEN_MINCONT	0.0001	—
BACK_SIZE	64	—
BACK_FILTERSIZE	5	—
BACK_PHOTOTYPE	LOCAL	GLOBAL
BACK_THICK	32	24
PHOTO_APERTURES	10.76	—
PHOTO_AUTOPARAMS	1.0, 2.0	2.5, 1.5
PHOTO_AUTOAPERS	8.1, 8.1	0.0, 0.0

of detected sources exactly matches our predictions inferred from the SED models (Figure 2.3 and 2.4). We assume 2 sigma limiting magnitude in Ks-band for Ks-faint objects. Among them, 134 and 212 objects meet our selection criteria in PKS 1138 and USS 1558, respectively. In these groups, 20 and 50 galaxies are not detected at Ks-band with more than two sigma, and thus those Ks-band magnitudes are assumed to be two sigma limiting magnitude for line flux and EW estimations.

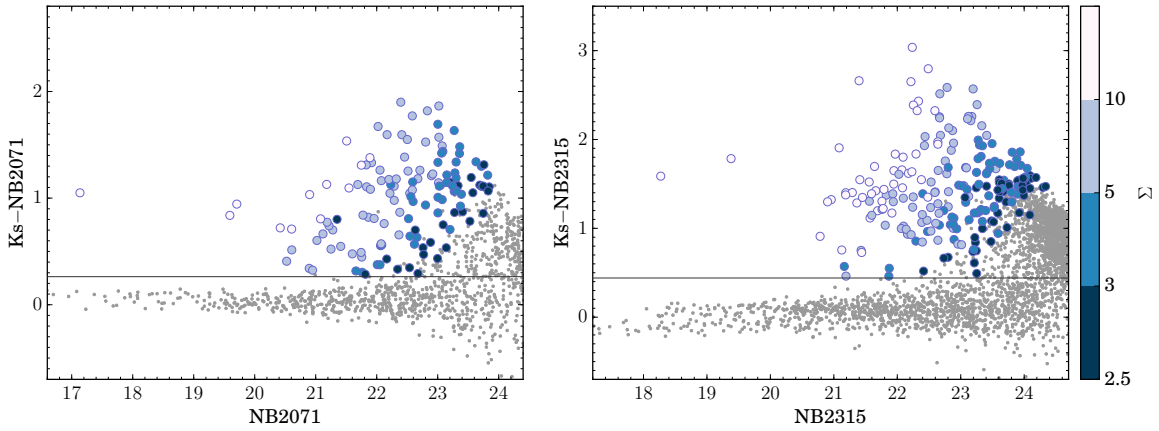

Figure 2.5: Colour–magnitude diagram (left: Ks–NB2071 for PKS 1138, right: Ks–NB2315 for USS 1558). Grey dots are all detected sources. Large circles have significant narrowband flux excesses more than 2.5Σ. Those colours are changed by significances of their flux excesses denoted by the colorbar on the right side. The black horizontal lines correspond to the criteria of line EW > 30 Å.

2.4 Sample selection

Based on the selected narrowband emitters samples, we have to conduct further analyses to choose HAEs more likely associated with protoclusters. This section describes procedures to identify HAEs using colour-colour digram and explains SED-fitting of HAEs after the corrections of those flux losses. We then mention the narrowband imaging survey for Lyα line in USS 1558 at $z = 2.53$ and a test of search for diffuse HAE sources by a unique detection method with high dynamic range mode.

Those processes were conducted with the assistance of the Tool for OPerations on Catalogues And Tables (TOPCAT; Taylor 2015).

2.4.1 Colour–colour selection

Further extractions should be needed to select HAEs located at the protocluster redshifts, since the current emitter samples would still have contaminants by the other line emitters, such as Pa$\alpha\lambda$18756, [SIII]$\lambda\lambda$9071,9533, and [OIII]$\lambda\lambda$4960,5008 lines. This work thus deselect such contaminant fore/back-ground emitters based on two simple colour-colour selections BzK, YHK for emitters in PKS 1138 and rJK, BrK for USS 1558, respectively. BzK and rJK have been used to remove low-z contaminants at $z < 1.5$ for each protocluster region (Koyama et al., 2013a; Hayashi et al., 2012). This work additionally uses YHK and BrK diagrams in PKS 1138 and USS 1558 to reject background [OIII] emitters at $z = 3.1, 3.6$, respectively. [OIII] emitters would be principal contaminations in narrowband imaging at Ks-band range according to An et al. (2014).

We demonstrate how efficiently these colour selections work based on the HAE samples with spec-z from the past MOIRCS spectroscopic surveys by Shimakawa et al. (2014, 2015b), and spec-z sources from the redshift catalogue in the COSMOS-CANDELS field by MOSDEF (Kriek et al., 2014) where the same broadband filter-sets as we employ here are available by 3D-HST photometric catalogue (Skelton et al., 2014). Also, we have some additional spectroscopically-confirmed HAEs by combining with the other studies in PKS 1138 (Kurk et al., 2000, 2004b; Croft et al., 2005; Doherty et al., 2010; Tanaka et al., 2013b). Furthermore, HAEs whose Lyα emission are identified by optical narrowband imaging surveys (Kurk et al. 2000; Shimakawa et al., see §2.4.3) are also included into the spec-z samples since they are highly expected to be protocluster members as well as spec-z sources. Combined with those spec-z samples, this work empirically defines colour thresholds on the colour-colour diagrams.

As a results, we find that whilst the colour diagnostics for HAEs in PKS 1138 would not work quite well, those for HAEs in USS 1558 allow us to select only HAEs at the expected redshift $z = 2.5$ efficiently (Fig. 2.6). Here we assume two sigma magnitudes for non-detections at each broadband photometry. rJK diagram can separate narrowband emitters into low-z ($z < 1.6$) objects and high-z objects, and then BrK diagram can remove [OIII] emitters at $z = 3.7$ since their Lyman Break features stride across between B and r-band wavelengths. On the other hand, contaminant [OIII] emitters at $z \sim 3.1$ still mix with objective HAE samples at $z = 2.2$ in BzK and YHK diagrams, suggesting that we may have unignorable contaminations in our HAE samples. To deselect background [OIII] emitters more completely, U-band photometry must be needed. However, we stress that the targets are overdense regions and thus such other line emitters should be poor relative

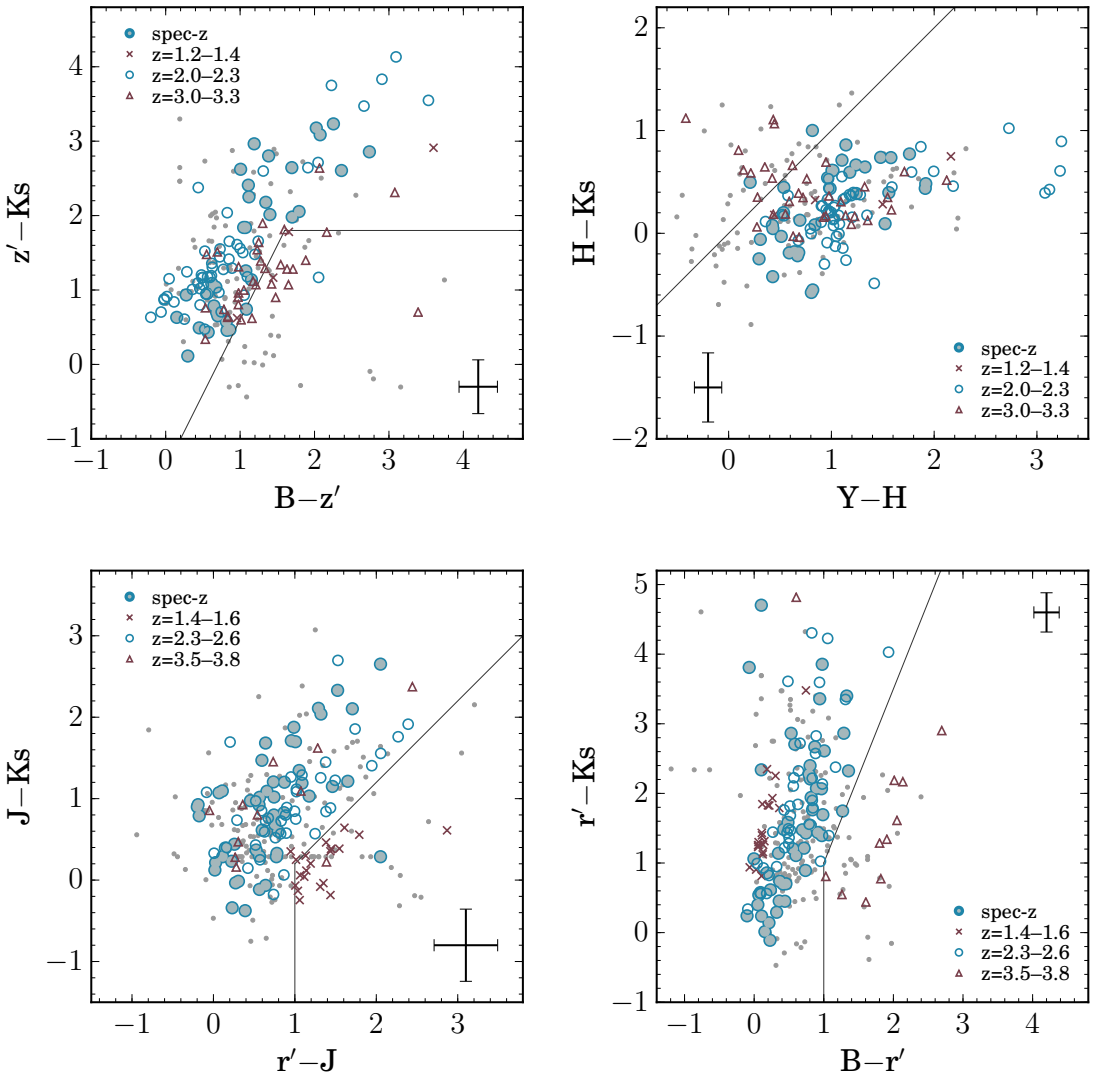

Figure 2.6: Moving clockwise from the upper left panel, Bz'Ks and YHKs for PKS 1138, and Br'Ks and r'JKs diagrams for USS 1558. Grey dots and blue filled circles indicate our narrowband emitters and those with spec-z or dual Lyα and Hα emitters that are highly expected to be protocluster members (see text). The black crosses on each panel show typical 1σ errors of the narrowband emitters. Red triangles and crosses are the spec-z samples by MOSDEF survey (Kriek et al., 2014) at $z = 3.0 - 3.3$ and $z = 1.2 - 1.4$ on the upper panels, and at $z = 3.5 - 3.8$ and $z = 1.4 - 1.6$ on the lower panels, respectively. These samples are helpful for us to deselect foreground [SIII] emitters and background [OIII] emitters.

to blank field survey. Indeed, our past spectroscopy with MOIRCS that has confirmed 28 BzK-selected HAE members, includes only 1 [OIII] emitter at $z = 3.1$ (Shimakawa et al., 2014), meaning very small fraction of contaminations even in PKS 1138.

Our colour-colour diagnostics allows further extractions of protocluster members, which provide us with 85 and 164 HAEs including spec-z objects in PKS 1138 and USS 1558, respectively (Table 2.4 and 2.5). This *thesis* employs these emitters as protocluster members hereafter.

Table 2.4: Classification of narrowband emitters in PKS1138−262.

Class	Selection	Numbers
Class0	NB2071	134
Class1	BzK, YHK	50
Class2	spec-z a/o LAEs	35
1+2		85

Table 2.5: Classification of narrowband emitters in USS1558−003.

Class	Selection	Numbers
Class0	NB2315	212
Class1	rJK, BrK	113
Class2	spec-z a/o LAEs	51
1+2		164

2.4.2 SED fitting

We then conduct SED-fitting for selected HAEs to derive their stellar mass and dust reddening. Those flux densities at multi-broadbands are estimated from photometry with fixed circular aperture that depends on seeing FWHM for each filter as summarised in the Table 2.1. Flux contamination from Hα (+ [NII]) lines to Ks-band magnitudes are also corrected. Then, flux losses of emission fluxes and broadband photometries in all samples are modified based on the MAG_AUTO photometry with PHOTO_AUTOPARAMS = 2.5 given by,

$$F_{\rm NB,Total} = F_{\rm NB,Kron1.0} \times \frac{f_{\rm NB,Kron2.5}}{f_{\rm NB,Kron1.0}}, \tag{2.8}$$

$$f_{\rm BB,Total} = f_{\rm BB,Aper} \times \frac{f_{\rm Ks,Kron2.5}}{f_{\rm Ks,Aper}}, \tag{2.9}$$

where F and f is line flux and flux densities of band filters. Kron1.0 and Kron2.5 mean MAG_AUTO measurements with PHOTO_AUTOPARAMS = 1.0 and 2.5, respectively. These flux corrections typically add corrections of 10% for line flux and 30% for broadband flux densities. The obtained Hα luminosities and rest-EW are presented in Fig. 2.7. Those mean values and scatters are $\log(L_{\rm NB}/{\rm erg\ s^{-1}}) = 42.32 \pm 0.41$ and 42.22 ± 0.39, and $\log({\rm EW_{NB}}/{\rm \AA}) = 2.23 \pm 0.30$ and 2.29 ± 0.26 in PKS 1138 and USS 1558, respectively.

We then carried out SED-fitting based on the SED-fitting code fast distributed by Kriek et al. (2009). The SED fitting was conducted assuming a fixed redshift of $z = 2.15$ for PKS 1138 and $z = 2.53$ for USS 1558, respectively, based on the stellar population model of Bruzual & Charlot (2003), the Calzetti et al. (2000) extinction curve, the Chabrier (2003) IMF (initial mass function), and fixed metal abundance of $Z = 0.008$. Also, this allows star-formation history with delayed exponentially declining star-formation (SFR $\propto\ t\ exp(-t/\tau)$) with $\tau = 10^9 - 10^{11}$ yr. Here, log(age/yr) between 7.6 and 9.4 are given. These values do not

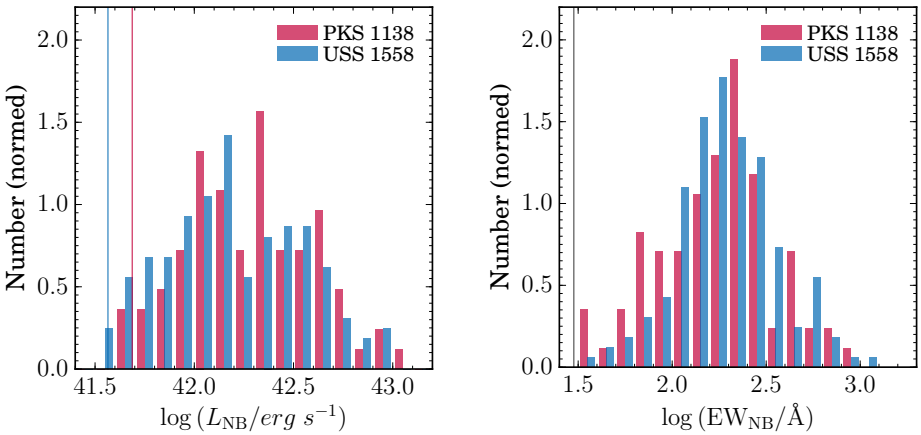

Figure 2.7: Distributions of narrowband (Hα+[NII]) luminosities and equivalent widths in the rest-frame of the HAE samples. Red and blue histograms show HAEs in PKS 1138 and USS 1558, respectively. Red and blue vertical lines on the left figure indicate flux limits for PKS 1138 and USS 1558, respectively. Black line shown in the right panel is threshold of line EW = 30 Å.

significantly affect stellar mass estimations, whilst measured dust extinctions are slightly dependent on input parameters. However, obtained values of dust extinction A_V in ~ 80 % of HAEs are still consistent within a range of ± 20 % uncertainties even if we apply free parameters for τ and age as long as the FAST code allows. This *thesis* ignores such a small model-dependency of extinction calibrations since this work solely focuses on relative comparison within the HAE samples selected in the exact same way based on the same datasets. We only use broadband photometries showing more than two sigma detections in individual HAEs. 1σ errors of obtained physical parameters are estimated by 100 Monte Carlo simulations attached with the FAST code.

Obtained stellar masses and errors of HAEs are presented in Fig. 2.8. We also measure stellar masses of galaxies at photometric redshift of $z = 2.0$–2.6 distributed by Skelton et al. (2014) for comparison. Our HAE samples are limited to certain Hα luminosities ($\log(L_{NB}/\mathrm{erg\ s^{-1}}) = 41.7$ and 41.6 in PKS 1138 and USS 1558, respectively), which cause incompleteness in stellar mass since less massive star-forming galaxies tend to have less active star-formation known as star-forming main sequence (Daddi et al., 2007a; Elbaz et al., 2007; Noeske et al., 2007). According to the figure, our HAE samples would be relatively complete above the stellar mass of $\log(M_\star/M_\odot) = 9.6$ and 9.4 if we believe that the number of HAEs increase in smaller stellar masses, which is quite feasible taking account of stellar mass function of HAEs at $z = 2.2$ in random field (Sobral et al., 2014). On the other hand, lower-mass HAEs than these threshold should be biased toward active star-forming galaxies. These stellar mass limits also seem to be consistent with distributions on the stellar mass versus Ks-band magnitude diagram of photo-z sources in the COSMOS field, although the comparison should be carefully considered for HAEs in USS 1558 because Ks-band magnitude limits are similar between USS 1558 and the COSMOS regions. This work defines HAEs with stellar masses more than those mass limits as mass-control samples, which provides us with relatively less-biased star-forming populations when we study and discuss physical properties of the HAE samples. The mass-control samples contain 57 and 88 HAEs in PKS 1138 and USS 1558, respectively.

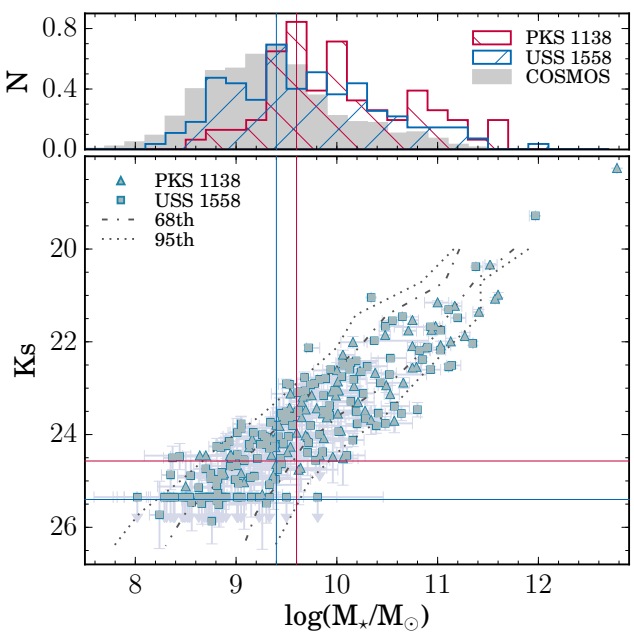

Figure 2.8: Stellar mass distribution as a function of Ks-band magnitude of HAEs. Red, blue, and grey histograms show the stellar mass distributions of HAEs in PKS 1138 and USS 1558, and 2519 photo-z sources at $z = 2.0 - 2.6$ in the COSMOMS-CANDELS field (Skelton et al., 2014), respectively. Theses are plotted on the figure of stellar mass versus Ks-band as triangle and square symbols, respectively. Horizontal lines indicate 2σ limiting magnitude in Ks-band (red: PKS 1138 and blue: USS 1558). Combined with 68th and 95th percentile distribution of photo-z sources at $z = 2.0 - 2.6$ as shown by dash-dot and dotted lines, we expect that our HAE samples are relatively complete at the stellar mass larger than $10^{9.6}$ and $10^{9.4}$ $M_\odot$ in PKS 1138 and USS 1558 (denoted by vertical lines), respectively.

2.4.3 Follow-up Lyα line survey of USS 1558

In order to widen search range of the super-dense USS 1558 protocluster and search for Lyα emitters (LAEs) associated with USS 1558, we conducted Lyα line imaging of USS 1558 at $z = 2.53$ with the the Subaru Prime Focus Camera (Suprime-Cam; Miyazaki et al. 2002) on the Subaru Telescope. The observation used the custom-made narrowband filter, NB428 belonging to R. Shimakawa (P.I. of this *thesis*) with support from the Research Fund for Studies (2013) of SOKENDAI. This filter is manufactured specifically for the purpose to detect objects with Lyα emission and absorption associated with the USS 1558 protocluster region at z=2.53±0.03. The NB428 filter has the central wavelength of 4297 Å and FWHM of 84 Å, respectively, with a good spatial homogeneity of the central wavelength less than ±3 Å across the field of view. In particular, the NB428 filter makes a pair with our companion filter, NB2315, (belonging to T. Kodama; see Shimakawa et al. 2016) installed on the MOIRCS/Subaru (Fig. 2.9). Combined narrowband analyses for resonant Lyα line and non-resonant Hα line by NB428 and NB2315 provide us with escape fractions of Lyα photons of HAEs in USS 1558 and those environmental dependence for the first time. In addition to that, LAEs at $z = 2.53$ selected by the NB428 filter have some great benefits. Those broadband photometries of F160W, Ks, U do not include H$\beta\lambda$4863, [OIII]$\lambda\lambda$4960,5008, H$\alpha\lambda$6565. or Ly$\alpha\lambda$1216 lines. This allows us to measure their accurate galaxy properties such as stellar masses and sizes from these broadband data and SED-fitting without strong rest-optical line contaminations. Nevertheless, all strong optical emission lines such as Hα, Hβ, [OIII], and [OII] lines including the [OIII]λ4364 auroral line can be observed with the ground-based telescopes, which enables robust estimation of those gas-phase metallicities based on the direct Te method (Izotov et al., 2006) by future spectroscopic observations with larger aperture telescopes.

With these motivations, we carried out Lyα narrowband imaging of the USS 1558 region on June 10, 2015 and UDS-CANDELS field for comparison on August 19, 2014 through the

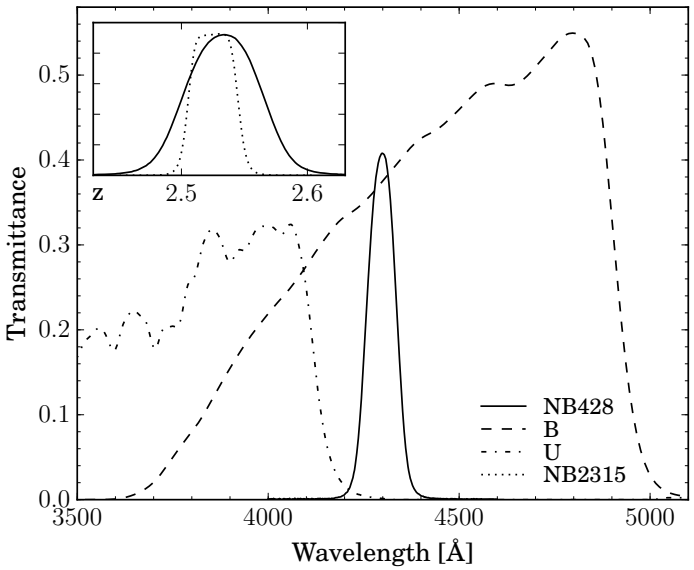

Figure 2.9: The narrowband filter, NB428. The black solid, the dashed, and the dash-dot curves indicate the filter transmittances of NB428 and B-band on the Suprime-Cam, and U-band on the CFHT, respectively. The upper left inset shows the filter response curves of NB428 on Suprime-Cam (solid curve) and NB2315 on MOIRCS (dotted curve) as a function of Lyα and Hα redshift, respectively.

Subaru Normal (S15A031; Shimakawa et al.) and Service programs (S14B198; Shimakawa et al.), respectively. Since the latter observation is already analysed and published by Shimakawa et al. (2016), this *thesis* mainly focuses on the Lyα line imaging of the USS 1558 protocluster. Especially, deep Hα image in USS 1558 should help us to confirm LAE candidates at $z = 2.5$ because majority of LAEs are considered to be less massive and less dusty objects and thus low-mass star-forming galaxies as reported by a bunch of past studies (Gawiser et al. 2006; Nilsson et al. 2007; Ouchi et al. 2008; Guaita et al. 2011, but see Hagen et al. 2016; Hathi et al. 2016) except very luminous LAEs most of which would be AGNs (Ouchi et al., 2008; Konno et al., 2016; Sobral et al., 2016).

The observation was carried out under photometric but bad seeing condition of FWHM = 0.8–1.4 arc sec. The science frame with seeing size worse than 1.2 arc sec are trashed and eventually we use 19 frames that reach in total 3.7 hrs integration time composing 700 sec exposures in each frame. The data were reduced by a data reduction package for the Suprime-Cam, SDFRED (ver.2; Yagi et al. 2002; Ouchi et al. 2004). This outputs a reduced final image semi-automatically in the standard manner, which includes bias subtractions, flat fielding, distortion correction, PSF matching, sky subtraction, and image mosaicing. More details of the pipeline are explained by Ouchi et al. (2004). In addition to that, we implement cosmic ray reduction using the algorithm of cosmic ray identification, L.A.Cosmic (van Dokkum, 2001). The final combined image has a seeing FWHM = 1.25 arcsec, and limiting magnitude of 26.26 in 3 sigma with 2.5 arcsec aperture diameter that goes down to 25.69 mag reckoning with the galactic extinction.

In common with the narrowband selection for Hα line, we select Lyα emitter (LAE) candidates by estimating significance of the narrowband flux excess. However, we here simply apply the traditional narrowband selection with fixed aperture photometry (Hayashi et al., 2010; Koyama et al., 2010), since seeing size of NB428 image is quite large and observational depth is shallow. This work selects the LAE candidates meeting criteria of more than three sigma flux excess, larger than $\mathrm{EW}_{\mathrm{Ly}\alpha} = 15$ Å in the rest frame, and NB magnitude brighter than 25.13 mag (five sigma in limiting magnitude). The correction

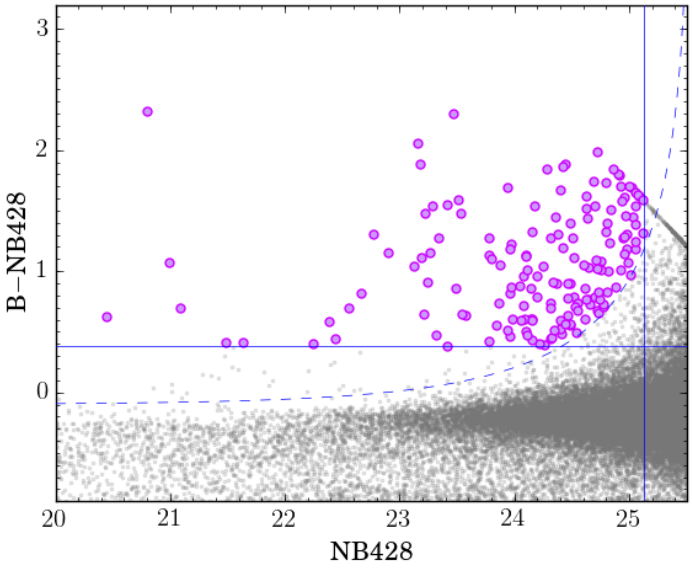

Figure 2.10: Colour–magnitude diagram to select Lyα emitters in USS 1558. The grey dots and the purple circles show detected objects and LAE candidates showing significant flux excesses, respectively. The dashed curve indicates threshold of 3Σ flux excess. The blue horizontal and vertical lines are EW threshold of 15 Å in the rest frame and 5σ limiting magnitude of NB428, respectively.

factor of the colour term ($\emptyset_{\mathrm{B-NB}}$) is assumed to be -0.1, which is tailored to that in our past study for the same NB428 filter in the UDS-CANDELS field (Shimakawa et al., 2016). Two sigma limiting magnitude are assumed for the sources without B-band detections. As a result, in total 162 objects show significant flux excesses in the narrowband image. This *thesis* employs all these samples as LAEs at $z = 2.5$, however, we note that considerable amount of foreground contaminations such as [OII]$\lambda\lambda$3727, 3730, CIV$\lambda\lambda$1548, 1551 should be included as noted by Sobral et al. (2016). The current available photometric data are only B, r, and z-bands with the Suprime-Cam, which are insufficient to obtain clean LAE samples. With this in mind, we handle the LAE samples with care, hereafter.

2.4.4 Do they have diffuse HAEs?

By utilizing high dynamic range for source extraction (HDR SExtraction) based on the SExtractor, we test if there is any faint and diffuse HAEs in our target regions. The HDR SExtraction technique is sometimes employed especially for the data with high spatial resolution like HST images (Rix et al., 2004; Barden et al., 2012; van der Wel et al., 2012; Guo et al., 2013; Galametz et al., 2013), since normal detection method by using the SExtractor tend to miss diffuse sources in high-resolution data. The purposes that we here use this unique method are not to miss faint HAEs as few as possible, and to discover diffuse HAEs if they exist in our data.

The HDR SExtraction is composed of "Cold" mode and "Hot" mode. These two detection procedures are separately conducted, and then combine those catalogues together in a manner similar to Barden et al. (2012). We set the Cold mode with the same detection criteria as for the narrowband selection (Table 2.3), and then additionally execute the Hot mode with the SExtractor again with different detection criteria, DETECT_THRESH=1 for the image smoothed by a top-hat function, which is useful to search objects with low surface brightness (see the manual edited by B. D. Holwerda). The hot mode provides us with additional diffuse sources as shown in Figure 2.11. Whilst most of those are highly likely noise, this technique stops us missing faint objects.

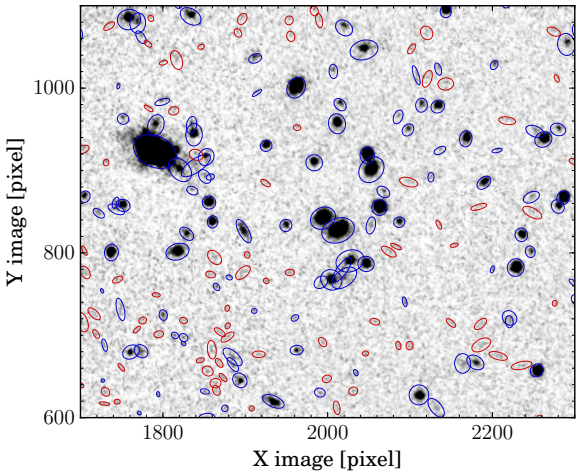

Figure 2.11: An example of the HDR SExtraction technique. We see that many noisy and diffuse sources are identified by the Hot mode shown by red Kron ellipses that cannot be traced by the normal detection method denoted by blue Kron ellipse (i.e. the Cold mode). Note that this figure only shows additional detections for the Hot mode detections.

3 | Appearance of the protoclusters with line emitters

Spatial distributions of narrowband-selected line emitters can identify structures and substructures in and around the protoclusters as demonstrated by the past studies (Tanaka et al., 2011; Koyama et al., 2013a; Hayashi et al., 2012). This section shows the results of Hα spatial mapping of the two protocluster fields. Also, we for the first time map Hα and Lyα emitters together in a high-z protocluster USSS 1558 at $z = 2.5$, which provide us with a unique opportunity to look into the escape fraction of Lyα photons with respect to Hα in dense environment. This gives an important caution to the previous protocluster surveys at $z > 3$ with Lyα emission line alone. Moreover, we show Hα and Lyα line geometries of the RGs inferred from the continuum-subtracted emission lines images.

3.1 Spatial distributions of line emitters

Due to the sophisticated selection technique, we have identified 85 and 164 HAE samples in PKS 1138 and USS1558, respectively. By utilizing such quite high sampling densities, we can search for another new HAE groups in these regions, and also can characterize underlying substructures more than ever.

In order to quantify the impact of environmental dependence, we start with defining two density parameters, namely, projected mean distance and fixed aperture density, to evaluate overdensities in the following manners,

$$\langle a \rangle_{\mathrm{Nth}} = 2\sqrt{\frac{1}{\pi \Sigma_{\mathrm{Nth}}}}, \tag{3.1}$$

$$\rho_{\mathrm{R}} = \frac{N}{\pi R^2}, \tag{3.2}$$

where N is the number of HAEs within a radius of r_{Nth} that is the distance to the $(N-1)$th neighbour from each HAE. Σ_{Nth} is the number density within the Nth radius ($= N/\pi r_{\mathrm{Nth}}$) and R is the fixed aperture radius. This work employs $N = 5$ and $R = 0.3$ ph-Mpc. Note that higher values in the mean distance and fixed aperture density indicate lower and higher densities, respectively. We also should stress that the measured density parameters maintain relative consistencies even if we choose a different N value as shown

in Figure 3.1, which compares the 5th mean distance with that from $N = 3$. Likewise, the choice of aperture size (R) for the measurements of ρ_R does not dramatically change the relative differences (Fig 3.1). In addition to that, we confirm the tight relationship between the mean distances $\langle a \rangle_{5th}$ and the fixed aperture densities $\rho_{0.3}$ as shown in the same figure.

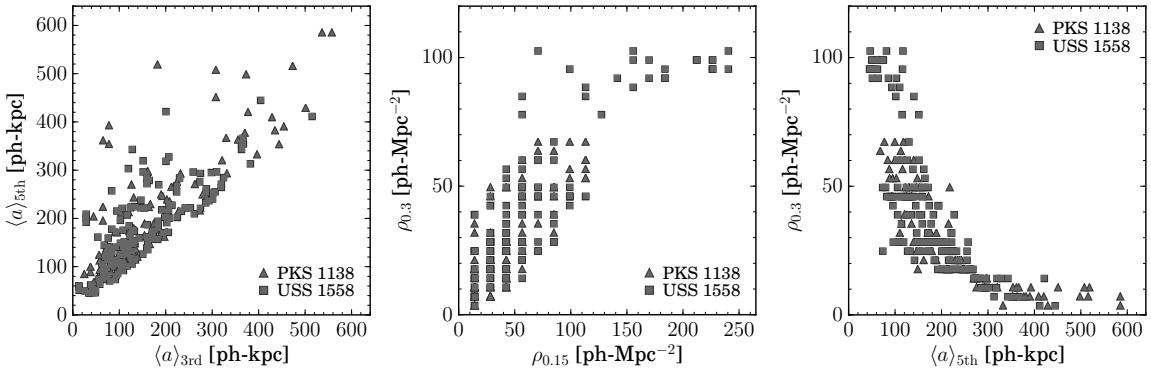

Figure 3.1: From left to right, the 3rd mean distance ($\langle a \rangle_{3rd}$) versus the 5th mean distance ($\langle a \rangle_{5th}$), fixed aperture density within the radius of 300 ph-kpc ($\rho_{0.3}$) relative to that within the radius of 164 ph-kpc ($\rho_{0.15}$), and the mean distance ($\langle a \rangle_{5th}$) versus the fixed aperture density ($\rho_{0.3}$). Triangle and square symbols indicate PKS 1138 and USS 1558, respectively.

Figure 3.2 shows the normalised distributions of the 5th mean distance and the fixed aperture density within the radial distance of 0.3 ph-Mpc. Both density parameters suggest that USS 1558 is a denser system of star-forming galaxies than PKS 1138 by $\sim 30\%$. The mean distance seems to distribute more continuously on the histograms than the fixed aperture density because the mean distance is defined by a more flexible aperture. We eventually decide to employ the 5th mean distance ($\langle a \rangle_{5th}$) hereafter unless otherwise noted, since this parameter simply tells us how closely star-forming galaxies are located between each other in the projected distance, and also since this parameter is roughly compatible with the impact parameter (b) and thus is very useful for the discussion (see §5.3). In either case, typical values of these density parameters indicate that our targets are associated with remarkably high overdensities, $\langle a \rangle_{5th} = 215^{+364}_{-112}$ ph-kpc and $\rho_{0.3} = 21^{+47}_{-9}$ ph-Mpc^{-2} in PKS 1138, and $\langle a \rangle_{5th} = 164^{+262}_{-95}$ ph-kpc and $\rho_{0.3} = 28^{+67}_{-13}$ ph-Mpc^{-2} in USS 1558, respectively. Especially, the HAE samples in the top 25 percentile overdesnsities in USS 1558 are assembling closely with less than 100 ph-kpc in the projected mean distance, suggesting that those haloes should overlap with each other sometimes physically and more easily along the line of sight, and possibly they can be in large common haloes with their neighbours. These values indicate that we are effectively collecting protocluster members up to denser regions by more than several times compared to any competitive studies (e.g. Yuan et al. 2014; Cooke et al. 2014; Chiang et al. 2015; Kubo et al. 2015).

We then investigate spatial distributions of HAEs and those density structures in PKS 1138 and USS 1558, given by Figure 3.3 and 3.4. Within the survey field of MAHALO-DEEP campaign, 47 and 100 out of 85 and 164 HAEs are newly identified protocluster members associated with PKS 1138 and USS 1558, respectively, as compared to the past studies (Koyama et al., 2013a; Hayashi et al., 2012). On the flip side, 9 and 4 sources in PKS 1138 and USS 1558 classified as HAEs by Koyama et al. (2013a); Hayashi et al. (2012) do not meat our selection criteria and thus those are not treated by this *Thesis*. We here

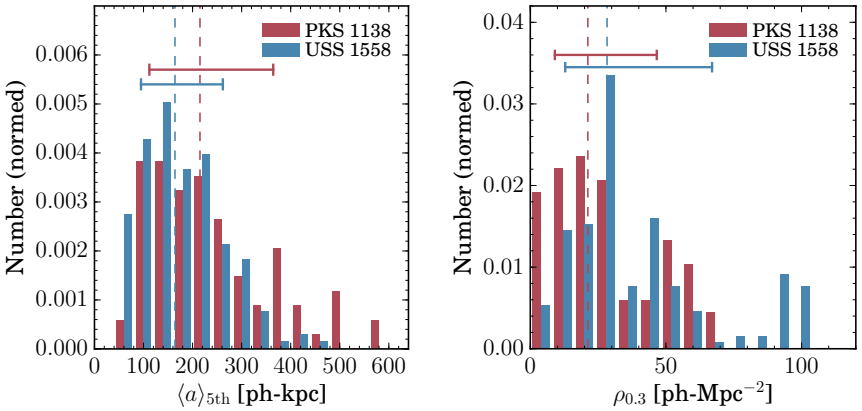

Figure 3.2: Normalised distributions of the 5th mean distance ($\langle a \rangle_{5\mathrm{th}}$) and the fixed aperture density within the radii of 300 ph-kpc ($\rho_{0.3}$). The red and blue histograms indicate PKS 1138 and USS 1558, respectively. The red and blue vertical dashed lines show the median values in PKS 1138 and USS 1558, respectively. The red and blue horizontal lines are standard deviations in PKS 1138 and USS 1558 for each diagram.

describe the characteristics of these two protoclusters mainly focusing on some newly-discovered features by this work, combined with a new result from the Lyα narrowband imaging for USS 1558.

Overall, deeper narrowband imaging for PKS 1138 allows us to detect even more HAEs associated with already-known substructures found by Koyama et al. (2013a), especially those following filamentary structures towards a north-western and north-eastern parts from the RG. Therefore, deep Hα imaging increases the contrast between dense and under-dense region on a local scale rather than that newly identified HAEs are distributed evenly across the survey field. On the other hand, our deep survey do not find any Hα sources in the southern void region again as reported by Koyama et al. (2013a), strongly suggesting that this field also has under-dense environment as contrasted with the centre region where projected mean distance reaches shorter than 100 kpc on the physical scale. In the centre massive structure, six HAEs including the RG are detected with the Chandra X-ray Observatory, suggesting the AGN overdensity in this region as reported by Pentericci et al. (2002). While nine HAEs including the RG are detected in the past narrowband imaging for Lyα line (Kurk et al., 2000, 2004a), other 23 LAE candidates are still not confirmed even by our deep Hα imaging. In fact, Kurk et al. (2000) have selected LAE candidates by comparing the narrowband with centre wavelength of 3814 Å with B-band photometry whose centre wavelength (4343 Å) is largely different from that of the narrowband filter. This would produce considerable contamination due to strong colour term effects, which might be the reason why we miss many LAE candidates by our Hα line imaging.

The previous HAE survey for USS 1558 has reported that three dense groups including the vicinity of the RG, the densest group in south-western region, and relatively smaller groups between them (Hayashi et al., 2012, 2016). Then, this observation have identified additional two dense groups of HAEs: a group northward from the RG and an eastern small group (Fig. 3.4). All those five groups have the peak density of < 100 ph-kpc in the 5th mean distance, meaning these are extremely dense environments. Such a protocluster fragmentation in USS 1558 suggests that this overdense region is still in a early phase of

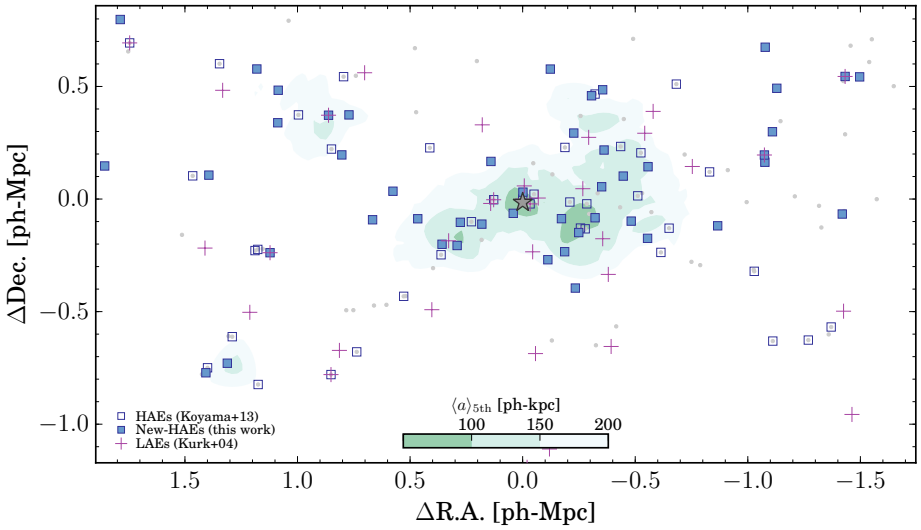

Figure 3.3: PKS 1138 at $z = 2.15$. The open and filled blue squares indicate HAEs that are also identified by Koyama et al. (2013a), and HAEs newly discovered by this work, respectively. The grey dots are narrowband emitters that do not meat our selection criteria. The purple crosses show LAE candidates reported by Kurk et al. (2004a), and some of those are spectroscopically confirmed (Pentericci et al., 2000; Croft et al., 2005). The star symbol is the RG. Green filled contours represent the regions with the 5th mean distances of < 100, 100–150, and 150–200 ph-kpc, which are smoothed by the Gaussian kernel of $\sigma = 0.5$ arcmin.

cluster formation. Those will eventually merge into a very massive galaxy cluster in the local Universe. In addition to that, we have found a filamentary structure that extends from the dense group around the RG in a westward direction.

Figure 3.4 shows the spatial distribution of LAEs and HAEs over the entire field of the Suprime-cam and the MOIRCS on the Subaru telescope. It should be noted that our LAE selection is only based on the colour–magnitude diagram (§2.4.4). Thus this should contain unignorable number of foreground contaminations such as MgIIλ2800, CIII]λ1909, and CIVλ1550 emitters at $z = 0.53$, 1.25, and 1.77, respectively (Sobral et al., 2016). Our Lyα line imaging over a much wider area (32'×27') than the MOIRCS field-of-view (4'×7') enables us with extending the survey field and thus search for a large-scale structures involving the USS 1558 protocluster. We see the density peak of LAE candidates around the RG reaching 4σ excess in the number density, which is quite roughly consistent with spatial distribution inferred from the HAE samples. The large-scale structure extends toward north-west, and there is another protocluster candidate 0.1 degree away from USS 1558.

Dual Lyα and Hα line survey for the first time provides us with insights into protocluster survey using Lyα line at further redshifts ($z > 2.6$) where Hα line is no longer observable from the ground. The fact that the large scale structure of LAEs associated with the USS 1558 protocluster at the same redshift range, indicates the availability of LAEs as the survey of large scale structures at high redshift. Within the MOIRCS field of view, 13 out of 16 LAE candidates are also confirmed by our Hα narrowband imaging unlike the result seen in PKS 1138. This suggests that these dual Lyα and Hα emitters should be cluster members at $z = 2.5$. However, surprisingly, we cannot find LAEs in the dense groups of HAEs except the RG that has very extended Lyα nebula. We could not find the

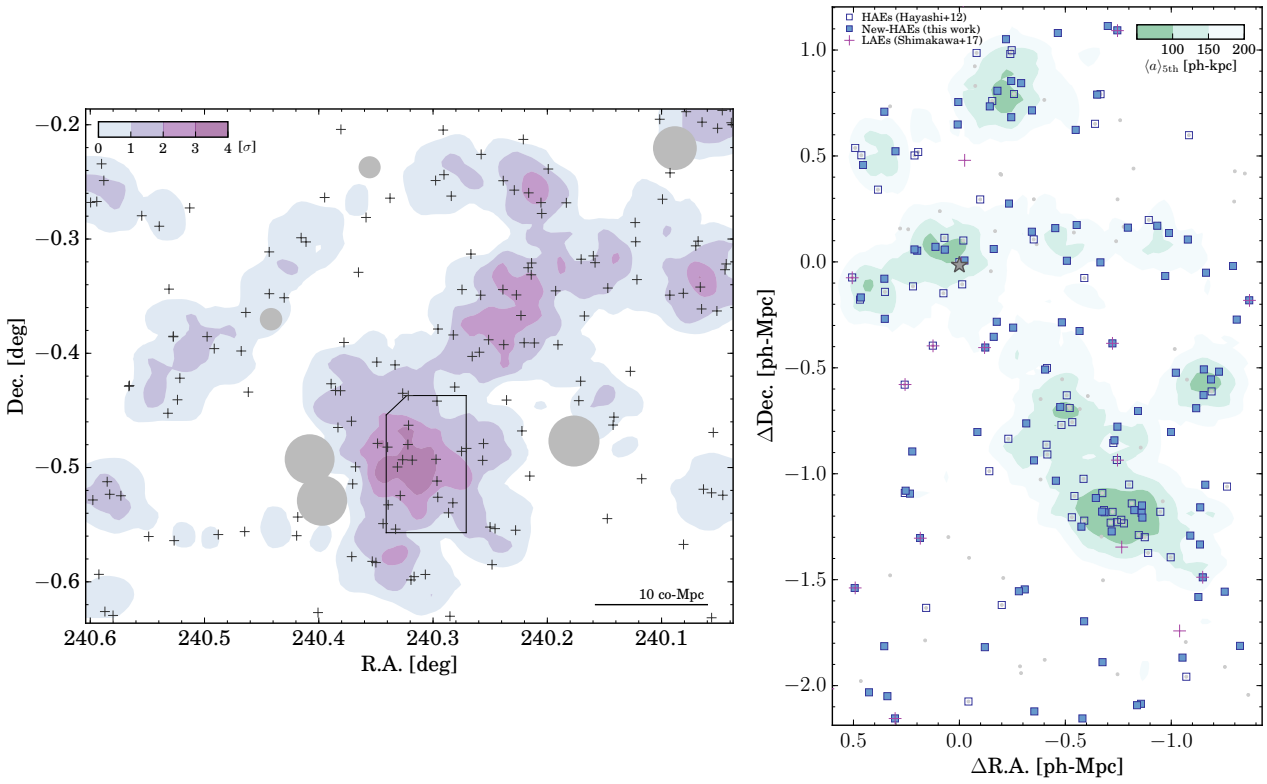

Figure 3.4: The USS 1558 protocluster. The left panel shows spatial distribution of LAE candidates discovered by the narrowband NB428 observation with the Suprime-Cam. Those are shown by the cross symbols. The region enclosed by black lines corresponds to the field of the narrowband Hα imaging for USS 1558 with the MOIRCS. The filled contours show the deviation of overdensities ($0-1\sigma$, $1-2\sigma$, $2-3\sigma$, $3-4\sigma$). These are based on the number densities within 2 arcmin radius smoothed by the Gaussian kernel of $\sigma = 1$ degree. The right panel shows spatial distribution of HAEs selected based on spec-z and broadband colours. Symbols and contours are the same as Fig. 3.3.

LAEs samples in the HAE overdesnities on the local scale. This suggests that LAE survey would miss overdense structures playing a critical role in protocluster regions, and also that identified galaxies by Lyα line observation also should be biased toward galaxies in not much relevant to overdense environments. Therefore, LAEs can be used for tracer of massive structures on more than ten Mpc scale, and yet it is no longer able to work for identifications of substructures smaller than that. We discuss this intriguing event more quantitatively in §4.2 and also its physical origins in the discussion section (§5.3).

3.2 Extended emission line nebulae around the radio galaxies

Our deep Hα narrowband imaging has detected extended Hα nebulae around the RGs in PKS 1138 and USS 1558. Both of those have end-to-end spatial extents of greater than 50 kpc on the physical scale, which are clearly larger than their stellar continua (Fig. 3.5 and 3.6) and seeing size of 0.63 arcsec.

In either RG, extended Hα nebulae align along the northeast–southwest directions,

which are consistent with the directions of radio continuum emissions and alignment of extended Lyα nebulae (Carilli et al., 2002; Villar-Martín et al., 2007). This suggests that wide-spread Hα haloes would be attributed to ionised circumgalactic medium due to large amounts of energy from jet. Such a wide-spread gas ionisation can be realised by energy-driven outflowing shell from the RG as simulated by the recent studies (e.g. Costa et al. 2014), which would be dominant outflow mechanism in galaxies hosting AGNs according to the modern observations (Genzel et al., 2014b; Cicone et al., 2014).

Figure 3.6 also shows large Lyα nebula (Lyα blob) associated with the RG in USS 1558. The Lyα emission extends over 100×100 kpc^2 that is larger than the size of the Hα nebula, while the alignment of Lyα line image looks consistent with that of Hα line. This would be due to resonant scattering of Lyα line through circumgalactic medium.

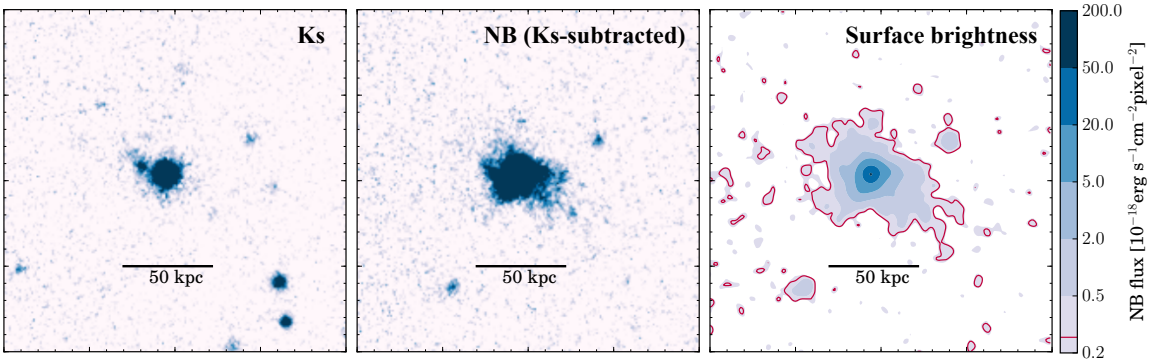

Figure 3.5: The left and the middle panels show Ks-band image (emission subtracted) and continuum-subtracted line image of the RG in PKS 1138 (the Spiderweb galaxy) at $z = 2.16$. The right figure represents surface flux densities per pixel by filled contour. The contour map is smoothed by the Gaussian kernel with sigma of two pixels. The red contour line corresponds to 2σ level of excess in narrowband flux per pixel.

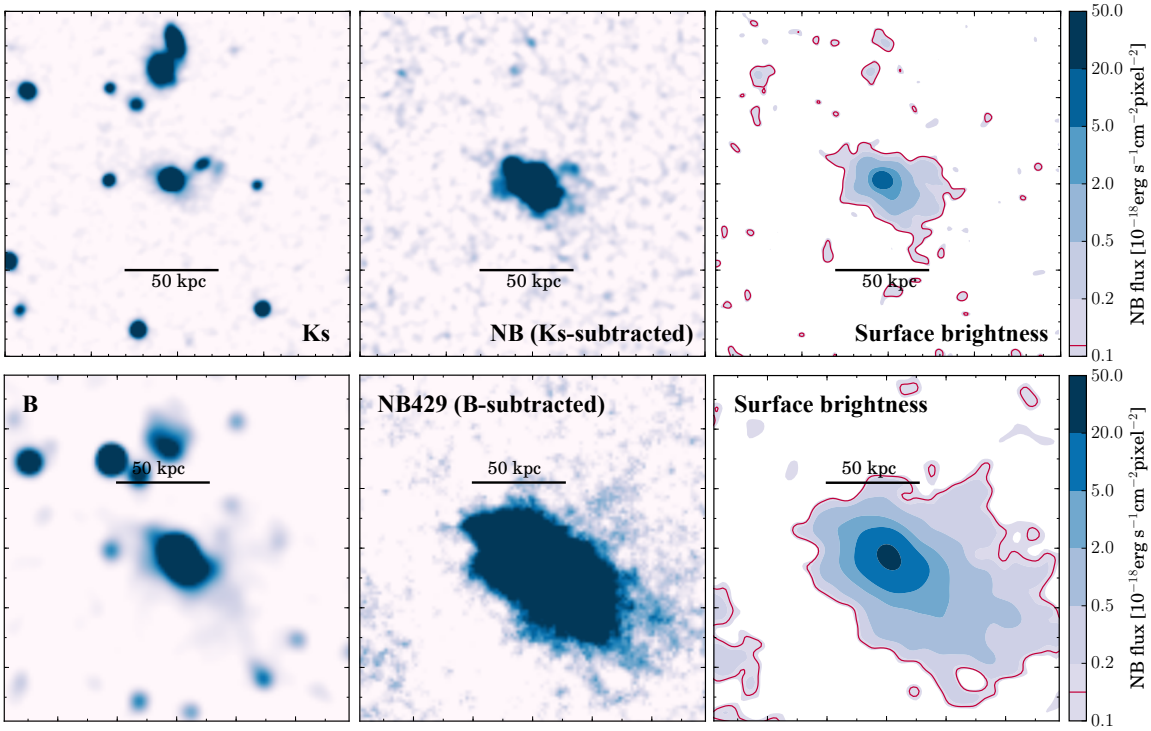

Figure 3.6: Upper three figures are the same as Fig. 3.5, but for the RG in USS 1558. The lower panels also show the RG in B-band (left) and Lyα (middle) images. The lower right figure is contour map of Lyα flux per pixels as shown in Fig. 3.5. The red contour line indicates 2σ level of excess in narrowband flux.

4 | The roles of environment on galaxy formation at the cosmic noon

H-**Alpha** narrowband photometry immediately enables us to determine star-formation rates (SFRs) of individual detected HAE sources from their line intensities through the Kennicutt (1998) prescription. Also, some other important physical parameters such as stellar mass and dust reddening can be derived from the SED-fitting based on the existing broadband datasets. This section informs us of how physical properties of HAEs change depending on galaxy overdensities by comparing those as a function of the mean projected distance across the protocluster regions. Furthermore, we investigate for the first time the environmental dependence of Lyα emissivities of star-forming galaxies by combining the HAE data with the narrowband Lyα imaging data at the same redshift slice which was also obtained by ourselves.

4.1 Characteristics of galaxies across environments

It is worth comparing star-forming activities of protocluster galaxies within the complicated structures with those in the random fields to understand the early environmental effects on galaxy formation. In particular, galaxy-galaxy mergers are expected to occur more frequently in protoclusters at high redshifts than in the general field (Okamoto & Habe, 2000; Gottlöber et al., 2001; Genel et al., 2014). Higher chance of merger events may increase the fraction of enhanced star-forming populations along the main sequence and/or seen as a scatter around the sequence.

4.1.1 Calibration of star-formation rate

We measure star-formation rates (SFR) of HAEs based on the Kennicutt (1998) prescription assuming Chabrier (2003) IMF (SFR is reduced by a factor of 1.8 compared to the standard Kennicutt 1998 calibration). We also estimate dust extinction at the wavelength of Hα emission line from the SED-inferred stellar extinction using the Calzetti (2001) attenuation curve and Cardelli et al. (1989) extinction curve. We derive a scale factor ($k_{\mathrm{H}\alpha}$) at the Hα wavelength as $\mathrm{A}_{\mathrm{H}\alpha} = k_{\mathrm{H}\alpha}\ \mathrm{E(B{-}V)}_{\mathrm{stellar}}$. We should note that ratio of nebular extinction to stellar extinction depends on galaxy properties, especially on SFR (Price et al., 2014; Koyama et al., 2015; Reddy et al., 2015). However, the assumption that $\mathrm{E(B{-}V)}_{\mathrm{stellar}} = \mathrm{E(B{-}V)}_{\mathrm{nebular}}$ is actually reasonable at high redshifts as reported by the recent deep spectroscopic survey with MOSFIRE (Reddy et al., 2015). They have reported the typical value of $\mathrm{E(B{-}V)}_{\mathrm{stellar}} - \mathrm{E(B{-}V)}_{\mathrm{nebular}} \sim 0.1$ where $\mathrm{E(B{-}V)}_{\mathrm{stellar}}$ is derived from the Reddy

et al. (2015) extinction curve that is similar to Calzetti (2001).

4.1.2 Star-forming main sequence

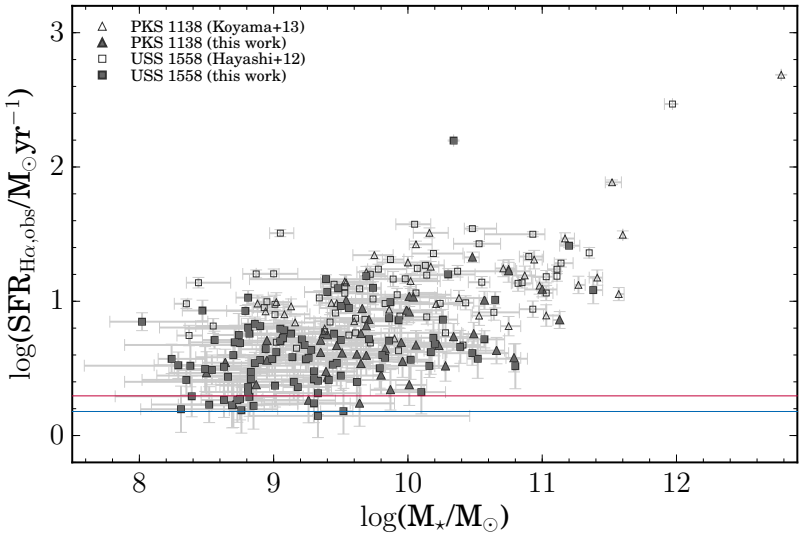

Figure 4.1: Stellar mass versus dust-uncorrected SFR from observed Hα luminosities. The triangles and squares are HAEs in PKS 1138 and USS 1558. The open and filled symbols indicate the HAEs already detected in the previous studies (Koyama et al., 2013a; Hayashi et al., 2012) and then confirmed by this work, and the ones newly identified by this work for the first time. Those 1σ errors are presented by errorbars in each plot. Horizontal lines correspond to the observed Hα flux limits in PKS 1138 (red) and USS 1558 (blue), respectively. Red open triangle and square symbols indicate median values and standard deviations of the HAEs in each stellar mass bin (1E8–9, 1E9–10, 1E10–11, and >1E11 M$_\odot$).

Figure 4.1 shows the dust-uncorrected SFRs of the HAEs as a function of their stellar masses. Flux limits of our narrowband observations correspond to the limits of log SFR = 0.24 and 0.16 M$_\odot$/yr without dust correction in PKS 1138 and USS 1558, respectively. Because of these SFR limits, our samples are biased toward highly active HAEs in the low-mass regime below M$_\star \lesssim$ 9.6 and 9.4 in PKS 1138 and USS 1558, respectively. We thus also define the mass-control samples for the HAEs with stellar masses above these thresholds (see also §2.5.2).

We show the same diagram of Fig. 4.1 in Fig. 4.2, but those SFRs are dust-corrected as explained in the previous section. The figure indicates a tight mass–SFR correlation called the star-forming main sequence, which is a well-known positive relation seen in the local Universe (Brinchmann et al., 2004) and at high redshifts (Daddi et al., 2007b; Elbaz et al., 2007; Noeske et al., 2007). We find that there is no clear difference between HAEs in PKS 1138 and those in USS 1558, and yet we have relatively more HAEs in the low-mass regime of USS 1558 since the Ks-band image of USS 1558 is deeper by 0.8 mag than that of PKS 1138. We also compare the results with the star-forming main sequence in the random field at $z = 2.1 - 2.6$ (Shivaei et al., 2015) and confirm that our mass-control samples in the protocluster regions are consistent with field galaxies as found by Koyama et al. (2013b). In the general field, Shivaei et al. (2015) have reported that the observed scatter of the

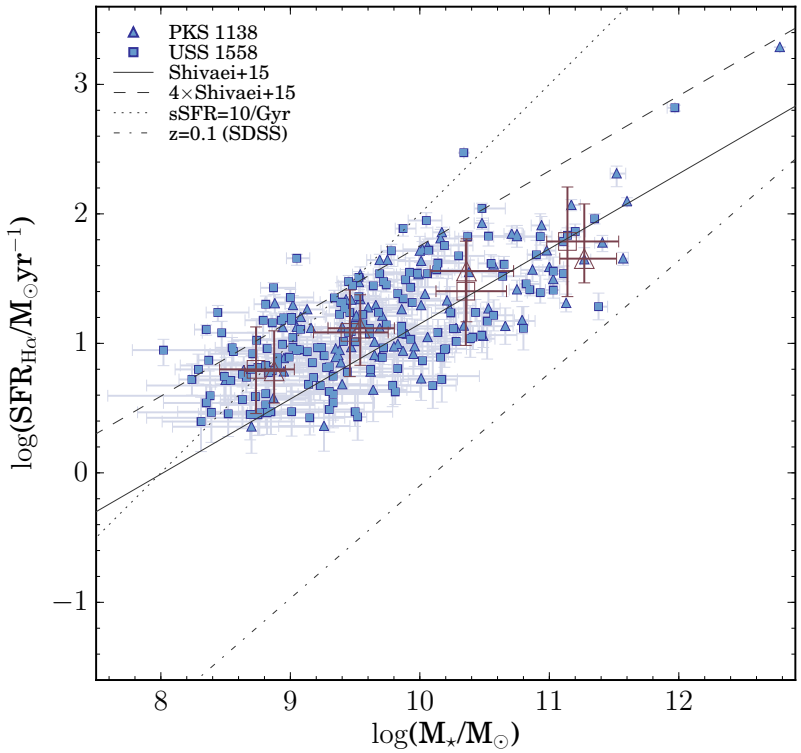

Figure 4.2: Stellar mass versus dust-corrected SFR. The symbols are the same as in Figure 4.1. Black dot-dashed, solid, dashed, and dotted lines indicate the star-forming main sequence at $z \sim 0.1$ based on the SDSS library (Abazajian et al., 2009; Brinchmann et al., 2004), that at $z = 2.1 - 2.6$ (Shivaei et al., 2015), the slope where SFR is 4× higher than that of Shivaei et al. (2015), and the constant specific SFR (sSFR) of sSFR = 10 /Gyr.

star-forming main sequence at $z = 2.1 - 2.6$ is 0.36 dex around the linear relation with the constant slope of $\log(\mathrm{SFR}/\mathrm{M}_\odot\ \mathrm{yr}^{-1}) = 0.58\ \log(\mathrm{M}_\star/\mathrm{M}_\odot) - 4.65$. The standard deviation around the main sequence of our mass-control samples shows a well consistent value of 0.35 dex with respect to their best-fitted main sequence. In this figure, we also show the best-fitted line of mass–SFR relation for the SDSS samples at $z = 0.027 - 0.25$ which are limited to those with the Hα line EW of more than 30 Å for consistency with our sample selection. Our HAE samples have by an order of magnitude higher SFRs for a given stellar mass than those of typical nearby galaxies that are selected based on the large SDSS data library (Abazajian et al., 2009).

Whilst we are missing less-active star-forming systems in the low-mass regime, the identification of low-mass HAEs of $\mathrm{M}_\star < 10^{9.5}\ \mathrm{M}_\odot$ is quite original since most of the past extragalactic surveys at $z > 2$ have only investigated more massive systems due to the observational limit. Our deep Hα imaging enables us to extend the Hα-emitting galaxies down to $\sim 0.2\ \mathrm{M}_\odot$/yr, and then almost double the sample size compared to the past observation in the same field (Fig. 4.1). Intriguingly, we have discovered extremely active HAEs as reported by Hayashi et al. (2016) whose specific SFR (SFR divided by stellar mass) exceed 10 Gyr^{-1}, meaning that they can product the same amount of stars as their current stellar masses within just 100 Myr. We discuss how faster such low-mass starburst

objects will grow into massive galaxies than typical low-mass galaxies in the discussion section (§5.1).

4.1.3 Environmental dependence on the substructure scale

We compare the physical properties of HAEs as a function of overdensity inferred from the mean distance across the survey fields which contain the protoclusters at the centre. This provides us with robust and reliable comparisons since the galaxies are observed and selected in exactly the same way. This work begins with dividing the HAEs in the PKS 1138 and USS 1558 protoclusters into three groups by the 5th mean distance ($\langle a \rangle_{5\mathrm{th}}$) defined in §3.1; denser 25th ($\langle a \rangle_{5\mathrm{th}} < 137$ and 116 ph-kpc in PKS 1138 and USS 1558, respectively), the 50th percentiles ($\langle a \rangle_{5\mathrm{th}} < 214$ and 164 ph-kpc), and the other halves ($\langle a \rangle_{5\mathrm{th}} > 214$ and 164 ph-kpc), respectively. We then test if there are any statistical differences in the physical properties among these groups by the Kolmogorov–Smirnov (KS) test.

The results of the comparison between HAEs in denser 50th percentiles and the lower densities in PKS 1138 are presented in Fig. 4.3 where we compare distributions of (a) stellar mass, (b) SFR, (c) specific SFR (sSFR), (d) deviation from the main sequence reported by Shivaei et al. (2015), (e) SED-inferred dust extinction, and (f) Y−Ks colour over 4000Å/Balmer break between the two samples. Table 4.1 also summarises the comparisons between HAEs in denser 25th percentiles and 50th percentiles in lower densities. It should be noted that denser 25th percentiles show the same behaviours as the HAE samples in denser 50th percentiles. As mentioned in §2.5.3, our HAE samples in PKS 1138 are relatively more complete at the stellar mass larger than $10^{9.6}$ $\mathrm{M}_{\odot}$. Therefore, we also carried out the tests based on the mass-control sample above this threshold, given by dotted lines in the figures. According to the KS tests based on the mass-control sample, the probability that HAEs at higher and lower density regions are drawn from the same parent population is less than 5 per cent for their stellar masses and Y−Ks colours. Also, p-values are close to ~ 0.1 as a function of sSFR and offset from the main sequence. On the other hand, we cannot find statistically significant differences in the other physical parameters since the p-values are always higher than 0.05. The results of the KS tests are summarised in Table 4.1.

Strong colour and mass dependence on environments in PKS 1138 agrees with the past studies by Koyama et al. (2013a,b). Koyama et al. (2013a) have reported that red HAEs tend to be located near the centre, while the spatial distribution of bluer HAEs seems to be more scattered. Moreover, Koyama et al. (2013b) have shown that the enhancement of stellar mass in HAEs around the centre of PKS 1138. Our results statistically confirm these trends. The environmental dependence of broadband colour over the 4000Å/Balmer break suggests that dense substructures in PKS 1138 are dominated by dustier or older star-forming populations. Either case seems feasible if we take into account of higher chance of galaxy mergers in high density regions (Okamoto & Habe, 2000; Gottlöber et al., 2001) or advanced galaxy evolution there due to the hierarchical clustering formation (Thomas et al., 2005). In addition to that, the mass enhancement seen in the comparison between the mass-control samples ($\mathrm{M}_{\star} > 10^{9.6}$ $\mathrm{M}_{\odot}$) suggests that galaxy mass assembly proceeds earlier or faster in denser environment. This also favours the two scenarios since both galaxy mergers and advanced galaxy evolution are expected to promote the mass enhancement. To constrain those evolutionary paths and star-formation time scale would

be important to resolve the environmental impact on massive galaxy formation, which can be demonstrated by the spectral analyses based on a deep near-infrared spectroscopy with the MOSFIRE (McLean et al., 2010, 2012) on the Keck telescope. On the other hand, we could not find the deficiency of less massive HAEs ($\lesssim 10^{10}$ $M_\odot$) in denser environments as reported by Cooke et al. (2014) in the MRC 2104 protocluster $z = 2.5$.

In the case of USS 1558, however, the two groups divided by the median values of the mean distance do not show statistical difference in physical properties except for SFR (Fig 4.4). We cannot rule out that two HAE samples separated by overdensities consist of the same population for physical parameters because of high p-values (> 0.05) except as to SFR, while it can be ruled out for SFR based on the comparison in the entire sample with $p = 0.02$. Even if we restrict the HAE samples to those in denser 25th percentiles, we confirm that these indistinguishable trends still looks the same and the statistics become less significant.

The USS 1558 protocluster still would be in a young phase of cluster formation as commonly seen at $z > 3$ because the red sequence is not sufficiently established yet unlike PKS 1138 (Kodama et al. 2007, see also Fig. 4.7). Indeed, there is a weaker difference in the 4000Å/Balmer break colours across environments as compared to PKS 1138. Thus, such a young forming phase of cluster in USS 1558 may not be sufficient to cause any clear difference in the other physical parameters between HAEs in different densities. Therefore, the environmental impacts on galaxy formation in the earlier-stage galaxy cluster before building of the red sequence is less important. We discuss this point more deeply in §5.4. In particular, the KS test shows high possibilities that the two samples are drawn from the same distribution in sSFR and in the deviation from the main sequence, while HAEs in dense environments tend to have higher SFR than those in lower-density regions. This would mean that SFRs of HAEs in higher density regions increase more likely along the main sequence not in perpendicular direction on the mass–SFR diagram. Thus, this may suggest that massive structures at $z = 2.5$ are suitable site to form massive galaxies, which would be closely linked to the Lyα depletion effect described in the following section (§4.2).

Combining these features seen in the two protoclusters at different redshifts, we could say that mass enhancement and redder galaxy colours in PKS 1138 at $z = 2.15$ could arise from SFR enhancement at higher redshift as observed in USS 1558 at $z = 2.53$. SFR and mass enhancements in USS 1558 and PKS 1138 might correspond to forming stage and late phase of massive cluster galaxy formation, respectively. We can also say that environmental dependence of physical properties would depend on physical characteristics of protoclusters and redshifts, since we see individual features in two protoclusters.

We see this trend more clearly if we compare stellar mass and SFR distributions of HAEs in the densest group with those in the outside of the dense HAE groups (Fig. 4.5). In USS 1558, five groups of HAEs are identified. We first identified groups that have galaxies with mean distance of $\langle a \rangle_{5\mathrm{th}} < 100$ ph-kpc and then classify surrounding neighbours up to ($\langle a \rangle_{5\mathrm{th}} = 150$ ph-kpc as group members. Defined five groups include a northern group (=YK), a group in a vicinity of RG (TK), a densest group in south-west region (MH), a group between TK and MH (IT), and eastern group (KT). Those contain 9, 12, 28, 9, and 6 HAE members, respectively, and 90 HAEs are out of those dense group environments. The densest MH group among them has a sufficient number to statistically compare physical properties of HAEs in group environments and those in the outskirts. As a results, HAEs in the densest group environment (MH) show both mass and SFR enhancements as compared

to those in the outskirts according to the KS test, which shows p-value of 0.02 and 0.01, respectively.

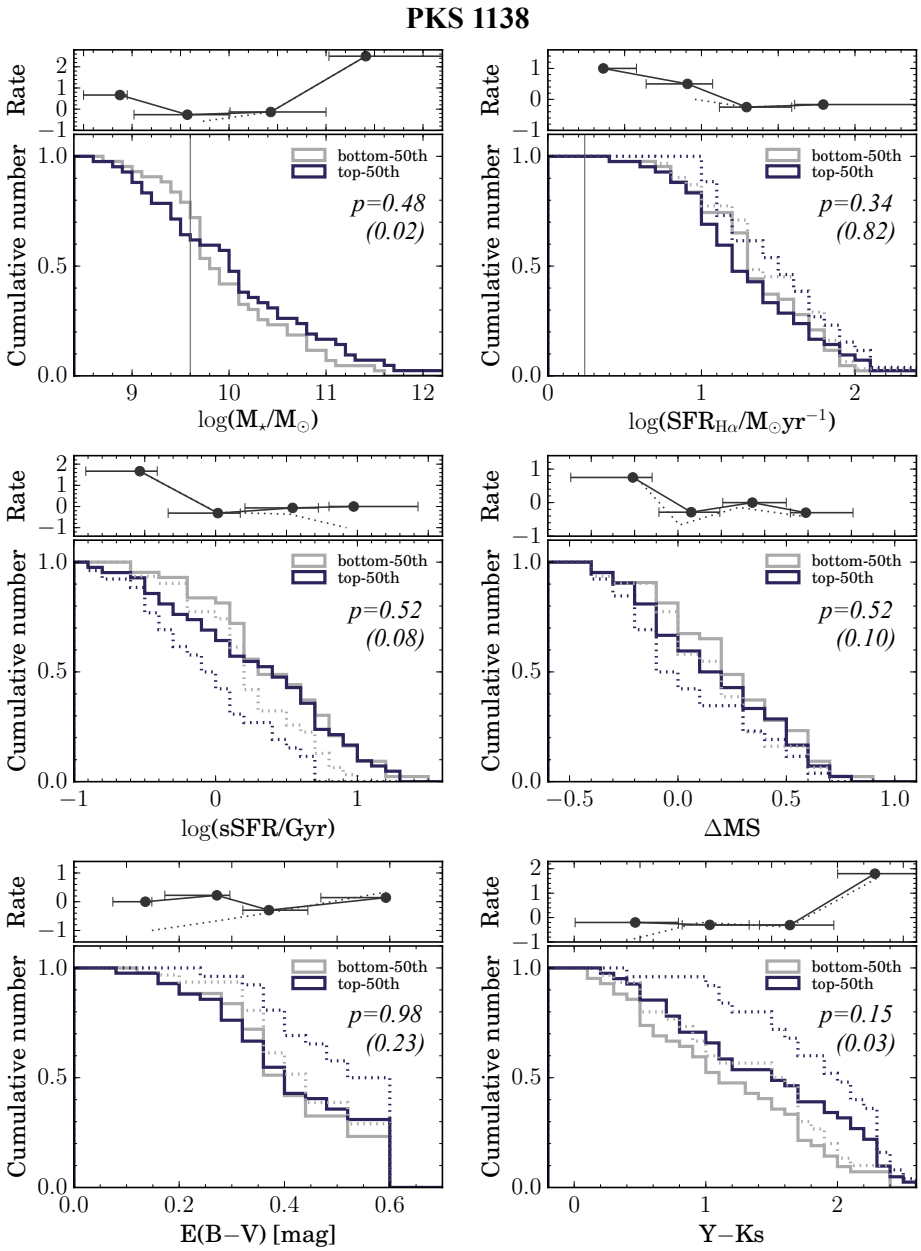

Figure 4.3: Cumulative distribution functions for galaxies properties, (a) stellar mass, (b) SFR, (c) sSFR, (d) deviation from the main sequence of Shivaei et al. (2015), (e) SED-inferred stellar extinction (E(B–V)), and (f) Y–Ks colour of HAEs in PKS 1138. The vertical lines in (a) and (b) show the mass limits of the mass-control sample and SFR limit, respectively. Purple and grey indicate distributions of the HAE samples with the mean distance of < 214 (denser 50th percentile densities) and ≥ 214 ph-kpc (bottom 50th percentile densities), respectively. Dotted cumulative functions are limited to the mass-complete HAE samples. Inset p-values are derived from the two-sample KS test (values enclosed by parentheses mean the p-values for the mass-control sample). The upper panels in each figures represent the excess rates of the number of HAEs in high-density regions relative to those in low-density regions at each bin, respectively.

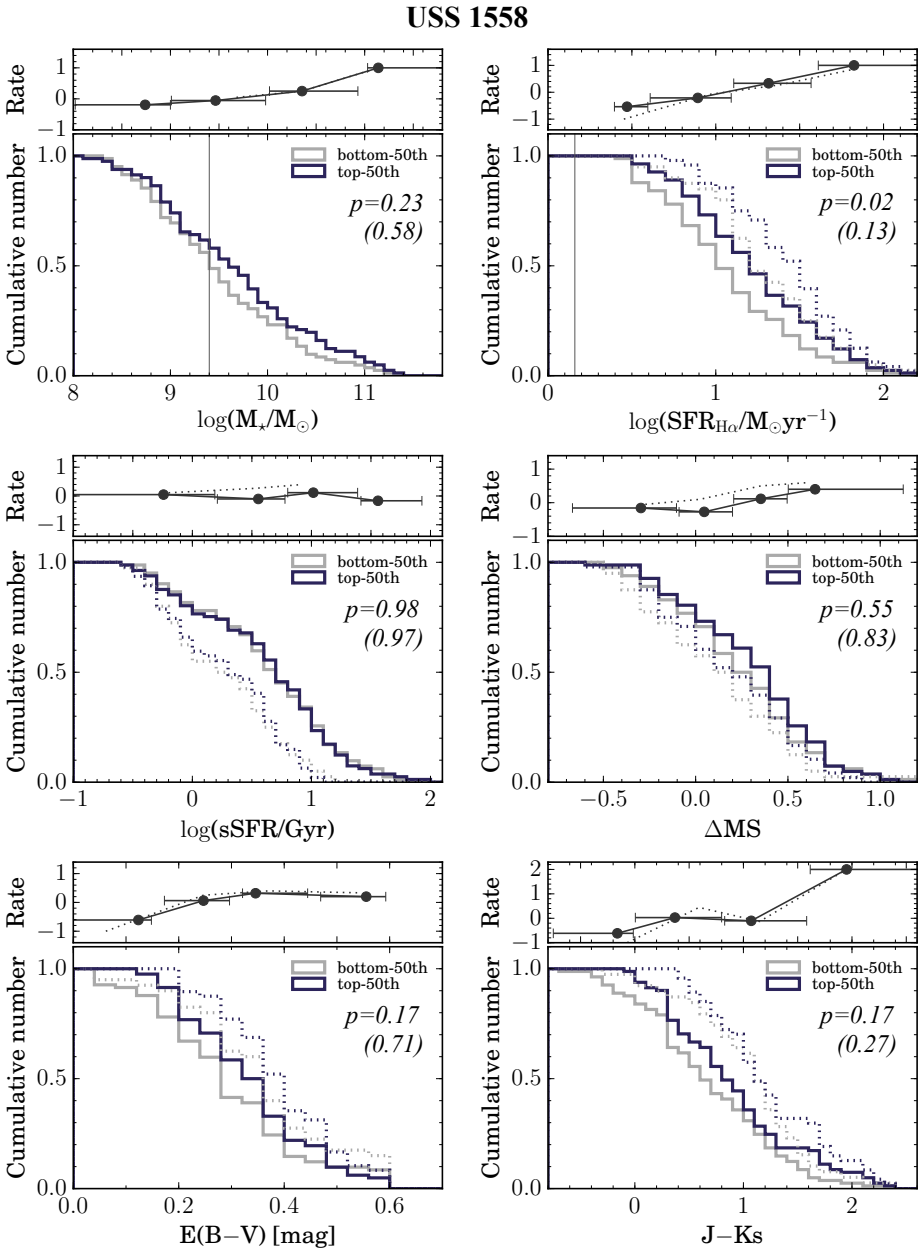

Figure 4.4: Same as Figure 4.3, but for HAEs in USS 1558.

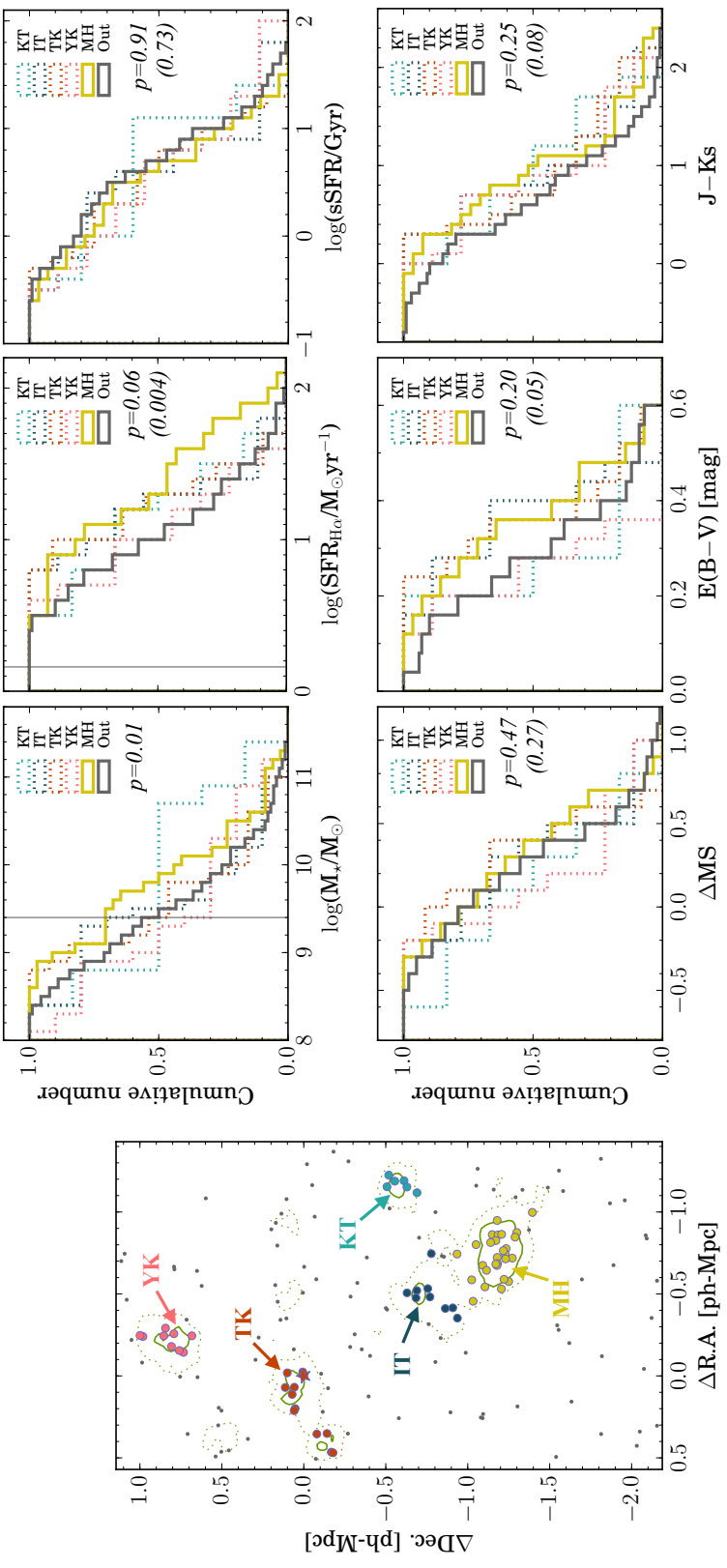

Figure 4.5: (Left) Companions in the USS 1558 protoclusters. Five groups are identified based on the following definitions. We first defined group cores including galaxies with a mean distance of $\langle a \rangle_{5\mathrm{th}} < 100$ ph-kpc (corresponds to $\lesssim -1\sigma$ of $\langle a \rangle_{5\mathrm{th}}$ in the entire HAE samples). Then, surrounding neighbours with $\langle a \rangle_{5\mathrm{th}} < 150$ ph-kpc ($\sim$ typical mean distance in USS 1558) are selected as group members. We eventually classified five groups, northern group (=YK), vicinity of RG (TK), densest group in southwest region (MH), group between TK and MH (IT), and eastern group (KT). Those consist of 9, 12, 28, 9, and 6 HAE members, which are shown with pink, red, yellow, blue, and cyan circles, respectively. (Right) Six panels on the right side are cumulative distribution functions of HAEs for six physical parameters as shown in Figure 4.4, but here we compare these properties among HAEs in each group and those outside of all the group regions.

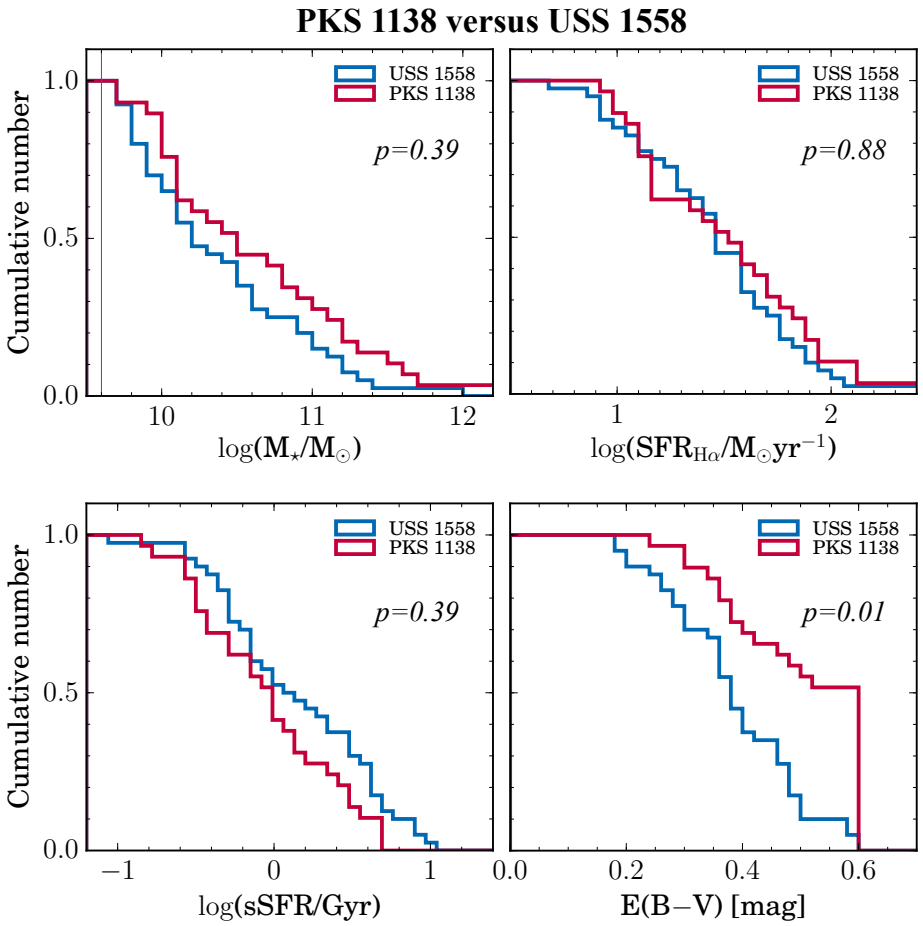

Figure 4.6: Comparison of physical parameters (stellar mass, SFR, sSFR, and E(B−V)) of HAEs between PKS 1138 and USS 1558. We use only HAEs of stellar mass $> 10^{9.6}$ $M_\odot$ to make a valid comparison. We also select HAEs in the dense region with the 5th mean distance lower than 110 and 80 ph-kpc in PKS 1138 and USS 1558, respectively.

We also compare HAEs between the two protoclusters in the same manner. Figure 4.6 shows the comparisons of physical properties (stellar mass, SFR, sSFR, and dust reddening) between HAEs in PKS 1138 and USS 1558. We use HAEs in higher density regions (denser 50th percentiles) for each protocluster and select the samples with stellar mass $> 1 \times 10^{9.6}$ $M_\odot$ to make a valid comparison. We find that PKS 1138 has more dusty HAEs than USS 1558. The possibility that these two populations are composed of the same population is only one percent. This trend is consistent with the result of the past MOIRCS spectroscopy (Shimakawa et al., 2015a), in which we have argued that the amount of nebular extinction at the wavelength of Hα for PKS 1138 would be systematically larger based on the Hα/Hβ line ratios (Balmer decrement) of the composite spectra. Indeed, PKS 1138 has 19 dusty HAEs detected at 24μm by MIPS on Spitzer (Koyama et al., 2013a). Moreover, it is likely that PKS 1138 tends to have systematically more massive and less active star-forming systems than USS 1558, although the statistics is not sufficient to draw a firm conclusion because of high p-values (> 0.3) in the KS tests.

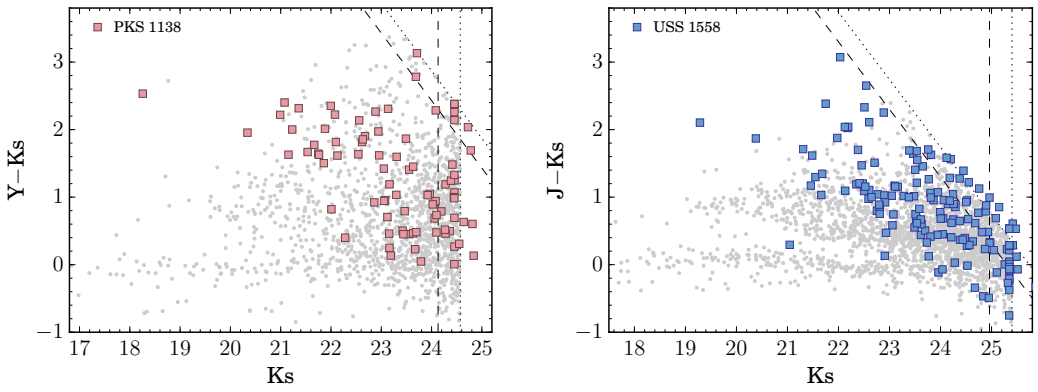

Figure 4.7: Colour-magnitude diagram for PKS 1138 (left: Ks versus Y–Ks) and USS 1558 (right: Ks versus J–Ks). The pink and cyan colours show HAEs in PKS 1138 and USS 1558, respectively. The grey dots are NB-detected sources. Two sigma limiting magnitude is assumed for the sources with band detection level lower than of two sigma. The grey dashed and dotted lines indicate two and three sigma limiting magnitude or colour limit at each band (Table 2.1), respectively.

Table 4.1: The comparison results in the KS test of HAEs in the lower densities (larger 50th percentiles in the mean distance) with those in denser 25th and 50th percentiles denoted as 25th-all and 50th-all, respectively. This table shows (r,p) values in the KS test for physical parameters shown in the Fig. 4.3 and 4.4 (log stellar mass, log SFR, log sSFR, deviation from the main sequence, dust reddening, and broadband colours across Balmer/4000Å break). 25th-mc and 50th-mc mean the comparisons in the mass-control samples.

Comparisons	$\log(M_\star/M_\odot)$	$\log(SFR/M_\odot yr^{-1})$	$\log(sSFR/Gyr^{-1})$	ΔMS	E(B−V)	4000Å colour
PKS 1138						
50th-all	(0.177, 0.481)	(0.198, 0.337)	(0.172, 0.518)	(0.171, 0.523)	(0.100, 0.977)	(0.241, 0.145)
50th-mc	(0.381, 0.024)	(0.161, 0.821)	(0.325, 0.079)	(0.313, 0.101)	(0.267, 0.227)	(0.377, 0.026)
25th-all	(0.200, 0.572)	(0.152, 0.874)	(0.219, 0.456)	(0.195, 0.608)	(0.146, 0.900)	(0.171, 0.767)
25th-mc	(0.419, 0.057)	(0.241, 0.600)	(0.402, 0.076)	(0.313, 0.275)	(0.228, 0.667)	(0.313, 0.275)
USS 1558						
50th-all	(0.159, 0.233)	(0.232, 0.020)	(0.073, 0.976)	(0.122, 0.548)	(0.171, 0.165)	(0.171, 0.165)
50th-mc	(0.181, 0.575)	(0.242, 0.133)	(0.100, 0.975)	(0.129, 0.834)	(0.146, 0.708)	(0.208, 0.267)
25th-all	(0.207, 0.168)	(0.256, 0.046)	(0.085, 0.985)	(0.207, 0.168)	(0.159, 0.463)	(0.171, 0.370)
25th-mc	(0.191, 0.696)	(0.325, 0.066)	(0.108, 0.991)	(0.175, 0.705)	(0.133, 0.936)	(0.250, 0.264)

4.2 Lyα emissivity in the protocluster

In §3.1, we have found a clear deficiency of LAEs in any of the notably dense group environments with the mean 5th projected distance of $\lesssim$ 100 ph-kpc. The following section investigates this intriguing phenomenon more quantitatively by comparing the number density distribution of HAEs with that of HAEs+LAEs, and also derive the escape fraction of Lyα photons from the stacking analysis. We here employ 13 out of 16 LAE candidates whose Hα lines are detected by our deep Hα line imaging, which are highly expected to be associated with USS 1558 at $z = 2.53$. Thus, the LAE samples used in this section are completely free from the foreground contaminations such as [OII]$\lambda\lambda$3727, 3730, CIV$\lambda\lambda$1548, 1551 emitters (Sobral et al., 2016).

4.2.1 Comparison between HAEs and HAEs+LAEs

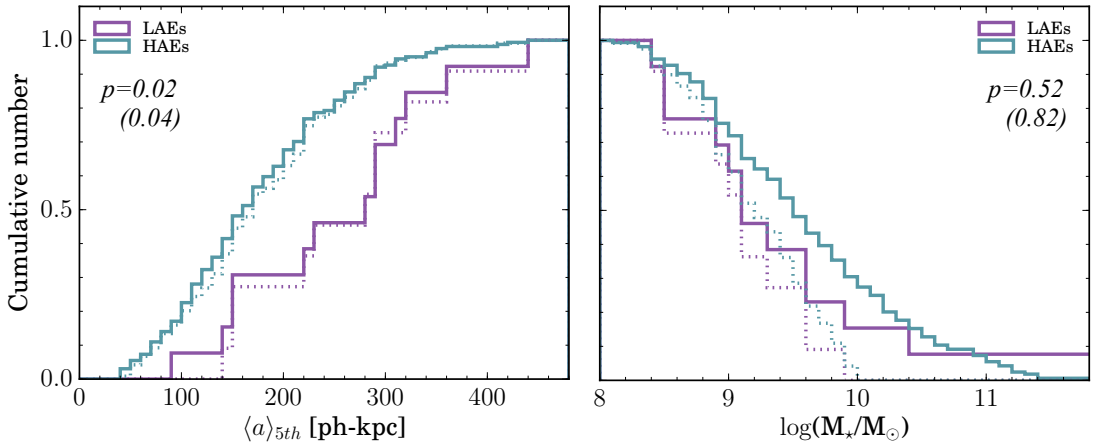

Figure 4.8: Cumulative distributions of (left) the mean projected distances and (right) stellar masses of HAEs and HAEs+LAEs shown by the blue and purple lines, respectively. Solid lines show the overall HAEs, while dotted lines are the mass-control samples with $M_\star < 10^{10}$ $M_\odot$. p-values of the KS test are shown in the inset of each figure (values enclosed by parentheses show p-values derived from the comparisons based on the mass-control samples).

Figure 3.4 in §3 have shown that the USS 1558 protocluster traced by the HAEs with MOIRCS are embedded in the much larger scale structures traced by LAEs. The location of the four sigma density peak of LAEs is quite roughly consistent with the main-body of USS 1558 traced by HAEs. However, on a much smaller scale (~150 ph-kpc), HAEs with Lyα line detections are distributed as if they are trying to avoid the overdense groups of HAEs. The fractions of HAEs+LAEs among the entire HAE samples are 11 ± 7 per cent in the lower densities ($\langle a \rangle_{5\mathrm{th}} > 150$ ph-kpc) and only 1 ± 3 per cent excluding the RG (or 3 ± 4 % with the RG) in the high density regions ($\langle a \rangle_{5\mathrm{th}} < 150$ ph-kpc), respectively.

Figure 4.8 shows the cumulative distribution functions for the mean projected distance, $\langle a \rangle_{5\mathrm{th}}$ (the left panel) and stellar mass (the right panel) for the HAEs and the HAEs with Lyα emission detections which are selected as LAEs as well. In the left panel, the possibility that "HAEs" and "HAEs+LAEs" are drawn from the same population is only two per cent according to the Kolmogorov-Smirnov (KS) test. Therefore, LAEs are statistically missing

in the dense protocluster cores, which suggest that Lyα photons are more depleted in the dense group cores. Such a statistical significance remains even if we use the mass-control samples where the samples are limited to the galaxies only with the stellar masses lower than 10^{10} $M_{\odot}$ (p=0.04). If we go further down in stellar masses, where such statistical test would become no longer significant, while the LAE deficiency at $\langle a \rangle_{5\mathrm{th}} < 150$ ph-kpc seems to still remain. In fact, there is no significant difference in stellar mass distributions between the HAEs and those with Lyα emission lines, because p-value is more than five per cent ($p = 0.07$) for the entire sample and is 18 per cent for the mass-control sample, respectively. Also, recent studies (Hagen et al., 2016; Hathi et al., 2016) have reported insignificant or small difference in stellar mass distributions between LAEs and non-LAEs against the past studies claiming that LAEs are significantly low-mass populations (Ono et al., 2010a,b). Considering these factors, the LAE deficiency in the protocluster cores can hardly be examined by the environmental dependence of stellar mass.

4.2.2 Escape fraction of Lyα photons

We measure the escape fraction of Lyα photons by comparing the Lyα and Hα line fluxes. This technique can quantify the depletion effect on Lyα emission line in the dense group cores in USS 1558, and then can provide us a further insight into its physical origins. However, the current NB428 data ($\mathrm{NB}_{5\sigma} = 25.15$ mag) are not deep enough to derive the escape fraction of Lyα photons for individual HAEs.

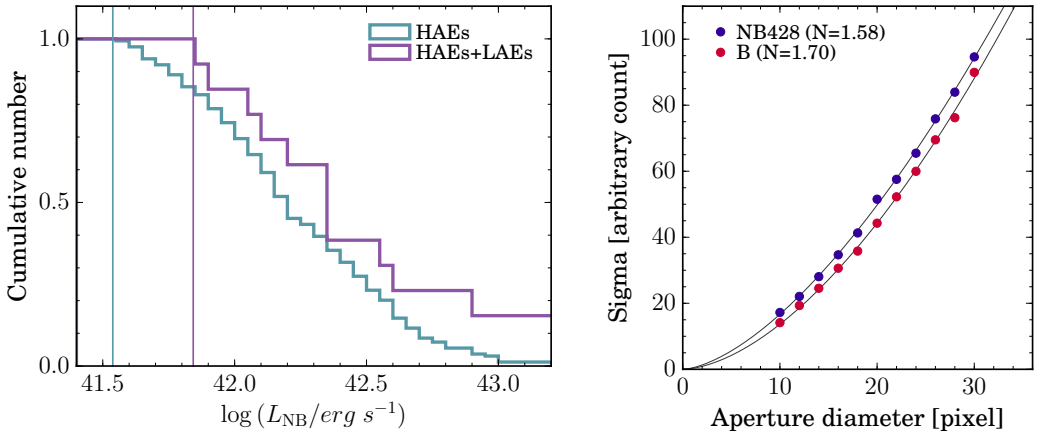

Figure 4.9: (a: left) The cumulative distribution function for Hα luminosities of the entire HAE samples and HAEs+LAEs. They are shown by the blue and the purple lines, respectively. The vertical lines correspond to the minimum Hα line luminosities for each sample. (b: right) 1-sigma Gaussian noise in background counts for the narrowband (NB428) and B-band data. The blue and red circles show the measured 1-sigma noises in NB428 and B-band, respectively. Then, those are best-fitted by the power functions as represented by the black curves.

For this reason, we perform the stacking analysis and estimate Hα and Lyα line luminosities with high precisions. The entire HAE samples are divided into two sub-samples by their local 2-D densities at the 5th mean distance ($\langle a \rangle_{5\mathrm{th}} = 150$ ph-kpc). In addition to that, we employ only bright HAE samples with Hα fluxes ≥ 1.347 erg s^{-1}cm^{-2} to determine the Lyα photon escape fractions with high significance levels. This threshold

corresponds to the lowest Hα line flux of dual HAEs and LAEs (Fig. 4.9a). It means that our stacking analysis compares the Lyα photon escape fractions across number densities above the Hα flux limit where we clearly see the LAE deficiency in the USS 1558 field. The narrowband images of individual HAEs are then combined with the IMCOMBINE task by median on IRAF.

Then, Hα and Lyα fluxes are calculated in the same manner as for the individual HAEs and LAEs as performed in this *thesis* (see §2.4.2). Photometric errors of line fluxes are derived with a similar approach taken by Skelton et al. (2014) and this work for the Hα narrowband data. The error estimation is based on the 1-sigma Gaussian noise in background counts that is measured by the random empty circular apertures with variable aperture size (from 10 to 30 pixels in step of 2 pixel size; see also §2.4.1). Then, measured 1-sigma noise counts are fitted by the power function (Fig. 4.9b). Through these processes, we eventually obtain photometric errors of the stacked images by dividing fitted error functions by the square root of number of science frames used for the stacking analysis. This enables us with quantifying errors in various photometric aperture sizes. Thus, our error estimations are carried out independently of photometries by the SExtractor since the SExtractor algorithm does not take account of the pixel-to-pixel correlation (i.e. this assumes that photometric errors increase with aperture area scaled as $\propto \sqrt{\text{area}}$), and thus the SExtractor photometry underestimates the errors especially for photometries with large aperture sizes. Indeed, the power indexes for NB428, B, NB2315, and K -band images are estimated to be N=1.58, 1.70, 1.41, and 1.35, respectively. Based on these procedures, we estimate Lyα and Hα fluxes. Here, both Lyα and Hα fluxes are measured with various photometric aperture radii from 6 to 30 ph-kpc taking into account the fact that most of the star-forming galaxies including Lyα-absorbed objects show diffuse Lyα components (Steidel et al., 2011; Matsuda et al., 2012; Matthee et al., 2016; Dey et al., 2016). The contribution of the PSF sizes to the science images are corrected for each.

Measured Lyα line fluxes of the composite HAEs seem to show diffuse Lyα profiles since those Lyα fluxes significantly increase with aperture radii over several 10 ph-kpc, while those Hα fluxes reach almost 100 per cent within aperture of 10 ph-kpc radii (Fig. 4.10). These differential surface brightness between Hα and Lyα line is consistent with Matthee et al. (2016) in which they have reported the similar results for the composite HAEs in the general field at $z = 2.23$. Lyα fluxes in the both sub-samples show negative values in small photometric aperture, which is consistent with the individual detection of Lyα absorption in massive HAEs in the random field (Shimakawa et al., 2016). Remarkably, moreover, Lyα feature appears in strong absorption in the composite HAEs in higher-density regions as compared to that of HAEs in lower-density regions. This suggests that Lyα line would have dramatically depleted in the protocluster cores along the line of sight. It should be noted that we employ the mesh size of 13 arc sec ($\sim$ 105 ph-kpc) for the sky subtraction in the data reduction process of the NB428 data. This may affect the estimation of Lyα line flux at the aperture sizes larger than $\gtrsim$ 25 ph-kpc, since it must be desirable that the mesh size for the sky subtraction is by more than two times larger than the photometric aperture size (see also Matsuda et al. 2012). However, regardless of the choice of mesh size, the depth of the composite NB428 image is clearly insufficient to determine precise line fluxes in such large aperture photometries, and thus we do not take care about this systematic uncertainty.

We then estimate the Lyα photon escape fractions of the composite HAE sub-samples,

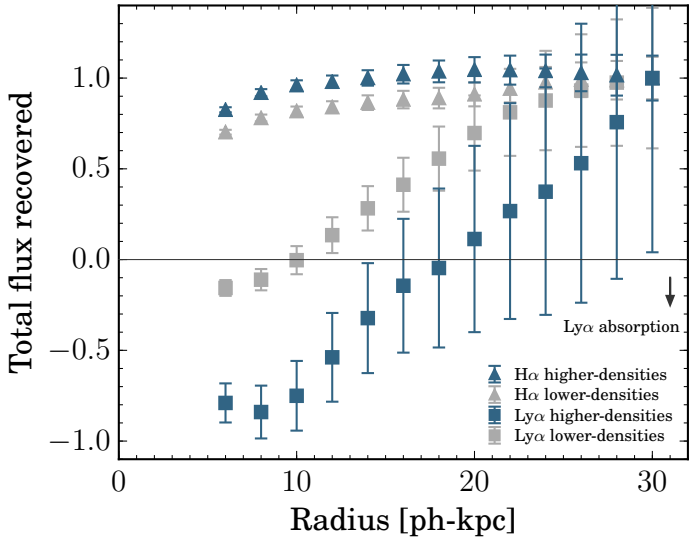

Figure 4.10: The proportions of line flux to the flux within 30 ph-pkc aperture radius as a function of aperture radius. The triangle and square symbols indicate Hα and Lyα fluxes, respectively. The blue/grey colours show HAEs in higher/lower density regions split at the mean projected distance of $\langle a \rangle_{5\mathrm{th}} = 150$ ph-kpc. The negative value on the y-axis means that composite line images show line profiles in absorption.

which is given by,

$$f_{\mathrm{esc}}^{\mathrm{Ly}\alpha} = \frac{f_{\mathrm{Ly}\alpha,\mathrm{obs}}}{8.7 f_{\mathrm{H}\alpha,\mathrm{int}}}, \tag{4.1}$$

where 8.7 is the ratio of Lyα line to Hα line under the assumption of case B recombination (Brocklehurst, 1971). $f_{\mathrm{Ly}\alpha,\mathrm{obs}}$ and $f_{\mathrm{H}\alpha,\mathrm{int}}$ are observed Lyα and intrinsic (dust-corrected) Hα flux, respectively. In order to determine dust-corrected Hα flux from the narrowband data, we assume a 10 % flux contamination from [NII]$\lambda\lambda$6550, 6585 line to the narrowband flux for Hα according to the typical line ratio of [NII] to Hα line flux (Steidel et al., 2014; Sanders et al., 2015). Moreover, 0.7 mag of dust extinction in Hα flux is assigned, which is based on the median value of nebular extinction in Hα for the entire HAE samples. The calibration technique of Hα extinctions of HAEs are described in §4.1.1.

We compare the measured Lyα photon escape fractions of the composite HAEs in high-density regions and those of HAEs in lower-density regions. Since Lyα line appears in absorption rather than emission on the inside, we obtained the negative values of the escape fractions of Lyα photons at the small photometric apertures (Fig. 4.11). More importantly, we find systematically lower Lyα photon escape fractions of the composite HAEs in high-density regions, which mean that the Lyα emission lines are systematically more depleted in the protocluster's dense cores than in lower-density regions in USS 1558. However, we should note that such a discrepancy between the two composite HAEs may also include such second factors besides environments, since the Lyα photon escape fraction should depend on various physical properties such as dust and SFR (Hayes et al., 2010; Matthee et al., 2016). We stress that this trend should be more enhanced if we take more appropriate values for the Hα flux corrections. The HAEs in denser environments tend to be a bit

dustier by 0.1 dex in the median value of $A_{H\alpha}$. On top of that, it should be noted that the narrowband photometries cannot resolve the detail spectral features around the Lyα line. It is expected that SiIIλ1207 absorption line may fall within transmission curve of the NB428 filter, and also we cannot rule out the possibility of the contamination from Lyα absorption due to foreground CGM/IGM and/or blue-shifted dense outflowing gas (Reddy et al., 2016b). Therefore, our estimations may underestimate the escape fraction of Lyα photons for these samples.

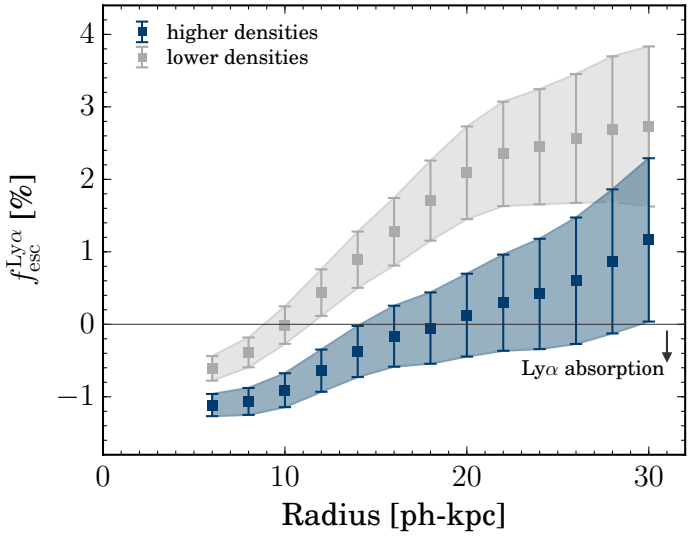

Figure 4.11: The escape fraction of Lyα photons in the composite HAEs as a function of aperture radius within which we integrate line fluxes. The HAE samples are divided into two sub-samples at the mean projected distance of $\langle a \rangle_{5th} = 150$ ph-kpc. The composite HAEs in the higher and lower density regions are represented by blue and grey zones, respectively. The errorbars are based on the 1-sigma photometric errors in line fluxes. The negative $f_{esc}^{Ly\alpha}$ values mean that Lyα is seen as an absorption line.

5 | Discussion

Based on total of 249 HAE samples traced down to the stellar mass of $\sim 10^8$ $M_\odot$ and the SFR limit of ~ 2 $M_\odot$/yr, this *Thesis* has analysed the environmental dependence of physical properties of star-forming galaxies on the group/substructure (several 100 ph-kpc) scale, associated with the massive protoclusters at $z = 2.2$ and 2.5. Moreover, we find that Lyα emission lines from HAEs in the protocluster's dense cores are remarkably depleted by analysing the dual Hα and Lyα emitters in USS 1558.

We discuss causal physical mechanisms inferred from the results presented in this *Thesis*, and characterise galaxy evolution in the growing protoclusters at z =2–3, in relation to many other achievements by relevant observations and simulations in the literature.

5.1 Star-formation in low-mass systems

This *Thesis* demonstrates a significant merit of identifying low-mass, active star-forming galaxies by deep narrowband imaging observations. In general, low-mass systems have very faint stellar continua, and thus it is quite hard to discover those by photo-z or magnitude-limited surveys. On the other hand, 20 and 50 out of 134 and 212 originally-selected narrowband emitters respectively, have not been detected in the Ks-band images, indicating that deep narrowband surveys work effectively to find line emitters even if the continua are very faint. As a result, we have identified very active HAEs in the low-mass regime, which have sSFR higher than $(0.1\ \mathrm{Gyr})^{-1}$. Such high sSFRs are more than four times larger than the sSFRs inferred from the main sequence (Shivaei et al., 2015). There is no better way to identify the detailed physical origins of such low-mass starbursts than to conduct a deep follow-up spectroscopy of these unique sources, since it is hard to characterise the faint star-forming objects only with the photometric data. However, even the current datasets allow us to constrain some physical mechanisms of such enhanced star-forming activities in low-mass systems by combing the Hα narrowband fluxes with the observed UV luminosities corrected for the dust reddening, as discussed in the following.

Figure 5.1 shows stellar mass versus SFR diagram for HAEs in both PKS 1138 and USS 1558 protoclusters as presented in §4.1.2. The colours of the symbols indicate the ratios of the observed SFRs derived from Hα luminosities to those derived from UV luminosities, respectively (we hereafter refer to this as " Hα/UV ratio"). The observed Hα/UV ratio basically reflects the amount of dust extinction since these wavelength are different each other (the dust reddening function at UV wavelength k_{UV} is higher by ~ 4 times than that of the wavelength of Hα line). Thus, it is expected that $\mathrm{SFR}_{\mathrm{H}\alpha}$ and $\mathrm{SFR}_{\mathrm{UV}}$ should ideally be the same (Kennicutt, 1998) once the dust attenuation is appropriately corrected for. Indeed, it is known that the observed Hα/UV ratios correlate with dust

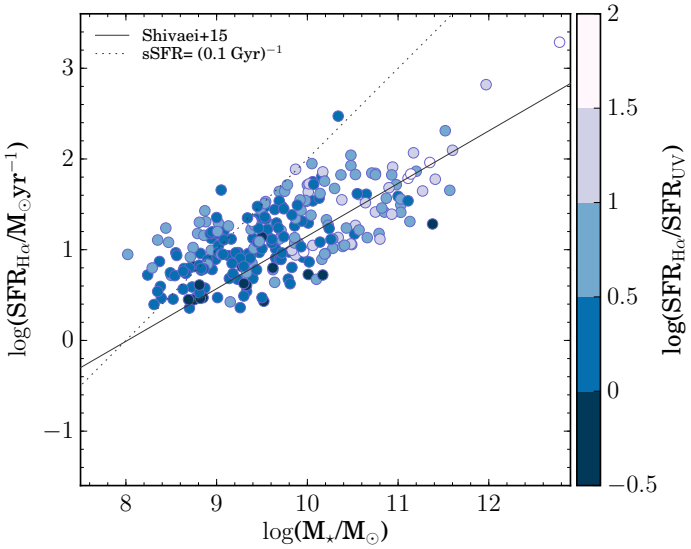

Figure 5.1: Stellar mass versus dust-corrected SFR from Hα luminosities of HAEs in PKS 1138 and USS 1558. Those colours represent the ratio of dust-uncorrected $\mathrm{SFR}_{\mathrm{H}\alpha}$ to $\mathrm{SFR}_{\mathrm{UV}}$. Those observed UV luminosities are derived from the SED-inferred flux densities at $\lambda = 1600$ Å. The black solid line shows the star-forming main-sequence at the similar redshifts by Shivaei et al. (2015). The black dotted line indicates the specific SFR of $(0.1\ \mathrm{Gyr})^{-1}$.

extinctions with a large scatter based on the large SDSS data library (Koyama et al., 2015). However, it should be noted that there is a considerable scatter in the observed and intrinsic Hα/UV ratios of star-forming galaxies (Price et al., 2014; Reddy et al., 2015; Koyama et al., 2015) since the reddening effects for Hα and UV are very different because Hα corresponds to the gaseous extinction while the UV corresponds to the stellar extinction.

Therefore, higher Hα/UV ratios of more massive HAEs seen in Fig. 5.1 can be normally attributed to stronger dust attenuation of massive star-forming galaxies. Such a correlation has been reported by a lot of past studies (e.g. Garn & Best 2010; Reddy et al. 2015; Koyama et al. 2015). On top of that, we can see a trend in the low-mass regime ($\mathrm{M}_\star \lesssim 1\times10^9\ \mathrm{M}_\odot$) that the low-mass HAEs with higher SFRs tend to have higher Hα/UV ratios than those with lower SFRs at the fixed stellar mass. To investigate it further, we compare the Hα/UV ratios of the low-mass HAEs as a function of specific SFR (sSFR) and dust extinction of Hα line in Fig. 5.2.

The comparison results indicate a clear correlation between sSFR and Hα/UV ratio. Also, surprisingly, we find a moderate anti-correlation between sSFR and Hα line extinction ($\mathrm{A}_{\mathrm{H}\alpha}$) derived from the SED-fitting. We have performed the Spearman's rank correlation test and these correlation and anti-correlation show p-values of 1.8×10^{-9} and 4.7×10^{-2}, respectively. The anti-correlation is inconsistent with the past studies that have reported that SFR tightly correlates with dust extinction (Reddy et al., 2015). Such a contradiction could be arisen if the galaxies with higher (specific) SFRs tend to have higher nebular (Hα) extinction values with respect to the stellar extinction values than those with lower (specific) SFR (Price et al., 2014; Reddy et al., 2015). If this is indeed the case, the apparent anti-correlation between sSFR and $\mathrm{A}_{\mathrm{H}\alpha}$ may be reversed and can be consistent, since this work has assumed the fixed ratio of nebular extinction to stellar extinction for all HAEs

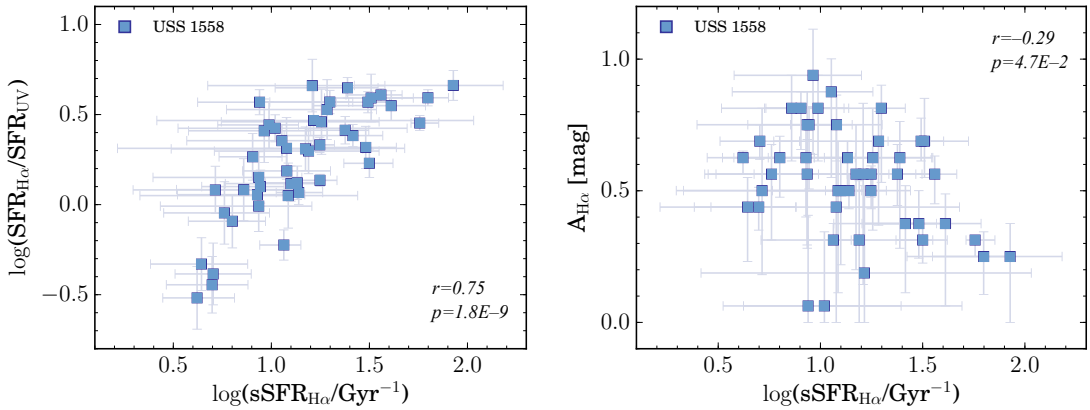

Figure 5.2: (a: left) Specific SFR versus the ratio of the observed (dust-uncorrected) $SFR_{H\alpha}$ to SFR_{UV}. These two parameters are closely correlated at more than five sigma confidence level ($p = 1.8 \times 10^{-9}$). The square symbols indicate low-mass HAEs ($M_\star < 1 \times 10^9$ $M_\odot$) in USS 1558. Observed SFR_{UV} and errors are based on r'-band photometry. (b: right) Specific SFR versus Hα extinction ($A_{H\alpha}$). Those two values are moderately correlated with $p = 0.047$ according to the Spearmans's rank correlation. The squares are the same as shown in the left panel. $A_{H\alpha}$ values are derived from the SED-fitting (§4.1.1)

(§4.1.1). However, the correlation between sSFR and the observed Hα/UV ratio cannot be reproduced by this effect, because it would rather enhance the intrinsic Hα/UV ratios of highly active low-mass HAEs. Therefore, in any case, the tight correlation between sSFR and Hα/UV ratio should not be caused by high dust obscuration, and Hα/UV ratio would be intrinsically high in more active star-forming galaxies in the low-mass regime. Another plausible scenario is needed to explain this unique trend.

Another causal factor would be the different time-scale of Hα line emission ($\leq$ several Myrs) from that of FUV radiation ($\leq$ 100 Myrs) (Cerviño et al., 2016). The Hα-derived SFR is more robust than the UV-inferred SFR, because the Hα line luminosity reflects more instantaneous star-formation activity than the UV luminosity (i.e. less dependent on past star-formation histories) and is much less affected by dust extinction either. In fact, the Kennicutt (1998) calibration from UV flux is calculated under the assumption of continuous star-formation over a timescale of 10^8 yrs or longer. Kennicutt (1998) also caution that this conversion would underestimate SFRs in younger star-forming populations. Wuyts et al. (2013) have reported an age dependence of intrinsic Hα/UV flux ratio for various star-formation histories (see Fig. 3 in their paper). For example, they show that the Hα/UV ratio is higher at younger ages (< 100 Myrs) if a constant star-formation rate is assumed. Further discussion may be needed in our analysis; less massive galaxies would have higher mass-loading factors due to their shallower potential wells (Okamoto et al., 2010; Muratov et al., 2015), and the subsequent star-formation is more easily truncated (Hayward & Hopkins, 2015), which may lead to periodic star-formation histories for low-mass HAEs. Therefore, it is not easy to determine star-formation histories of such low-mass systems. However, it is highly likely that very active low-mass HAEs would be dominated by young stellar populations (< several Myrs) compared to older populations.

In addition to that, binary star evolution that takes into account of quasi-homogeneous evolution (see the introduction §1.2.2) might be important to explain high Hα/UV ratios of

active HAEs in the low-mass regime. High redshift galaxies tend to have lower metallicities, especially stellar Fe abundance, due to the lack of the chemical enrichments by type-I supernovae (Steidel et al., 2014, 2016). In such a ISM condition, assuming the case B recombination (Brocklehurst, 1971) and a star-burst population with a total stellar mass of 10^8 $M_\odot$ and SFR of 10 $M_\odot$/yr, the FUV luminosity increases by a factor of ~ 3, and the ionising photon flux even more increases by a factor of ~ 12 as compared to those in a meta-rich condition (Stanway et al., 2016). To test this hypothesis, deep spectroscopic observations with MOSFIRE and LRIS on the Keck telescope will be effective, since these surveys allow us to constrain ISM conditions and metallicities of low-mass HAEs and then compare those as a function of sSFR and Hα/UV ratio.

So far, we do not know much about the detailed physical properties of low-mass star-forming galaxies, however, our new samples are unique and can help us to understand the formation histories of the present-day L^*-type galaxies (Gawiser et al., 2007; Guaita et al., 2010, 2011; Shimakawa et al., 2016). Such a deep follow-up spectroscopy is highly desired in the future.

5.2 Environmental dependence of galaxy properties

We have found some environmental dependencies of physical properties in the two protoclusters by comparing cumulative functions of six physical parameters (stellar mass, SFR, sSFR, ΔMS, E(B−V), and 4000Å/Balmer break colour) between the two sub-samples divided by the projected mean distance. The environmental variation in physical properties seems to depend on the protocluster sample and the substructures within the protoclusters. Below, we discuss the most plausible scenario that can account for all the observed trends presented in this work.

Firstly, the comparison of cumulative distributions between lower and higher halves in the mean distance reveals a statistical difference in stellar mass for HAEs in PKS 1138 and in SFR for those in USS 1558. However, there is no clear difference between the two environmental groups in the deviation from the main sequence (ΔMS). This suggests that stellar masses and SFRs of HAEs in denser environments are systematically shifted upper-rightward, approximately in parallel to the main sequence. To evaluate this hypothesis more quantitatively, we revisit mass–SFR diagram of the protocluster galaxies (Fig. 5.3), and then define the position along the main sequence with respect to a certain point on the main sequence as ||MS. It is defined by the following equation,

$$|| \,\mathrm{MS} = \frac{|\log(\mathrm{SFR}/\mathrm{M}_\star\ \mathrm{yr}^{-1}) + 2.27\log(\mathrm{M}_\star/\mathrm{M}_\odot) - 19.2|}{\sqrt{(1+2.27^2)}}. \tag{5.1}$$

||MS quantifies a systematic offset along the best-fitted mass–SFR relation for HAEs as illustrated by the black arrow in Fig. 5.3.

Measured ||MS distributions are shown in Fig. 5.4. We do not find any statistically significant difference in ||MS between lower and higher density regions within the protoclusters according to the KS test (p-values of ~ 0.2 at minimum). However, we do see a slight offset between the cumulative distribution functions in each protocluster (Fig. 5.4) in the sense that denser structures tend to involve more massive and active star-forming galaxies. Moreover, we can see such a trend at the massive end ($\gtrsim 1\times10^{11}$ $\mathrm{M}_\odot$) in PKS 1138 while the similar feature likely appears at relatively lower mass regime in USS 1558 ($\gtrsim 1\times10^{10}$ $\mathrm{M}_\odot$) compared to PKS 1138. This may be corresponding to the growth history of massive cluster galaxies from $z = 2.53$ to $z = 2.15$, although we cannot strongly say that by only two protoclusters. Possible excess of the number of active, massive star-forming objects in particularly dense structures within the provinces of PKS 1138 and USSS 1558 suggests that such overdense structures at $z = 2$–3 promotes galaxy growth into more massive systems faster/earlier than in lower density environments. These intriguing results motivate us to increase protocluster samples in order to statistically consolidate our hypothesis in the future (see also §7.4).

Deep narrowband imaging also reveals that the fraction of HAEs in the denser regions of PKS 1138 tend to be more occupied by red, massive star-forming galaxies than that in the low-density regions in the same field. Such environmental difference in colour and stellar mass function may be strongly linked to the conditions of circumgalactic/intergalactic medium (CGM/IGM) within the massive structure of PKS 1138. Massive galaxies in the late phase of declining star-formation histories would be redder (passive reddening), since the amount of inflowing cold gas would be deficient due to such as shock heating and

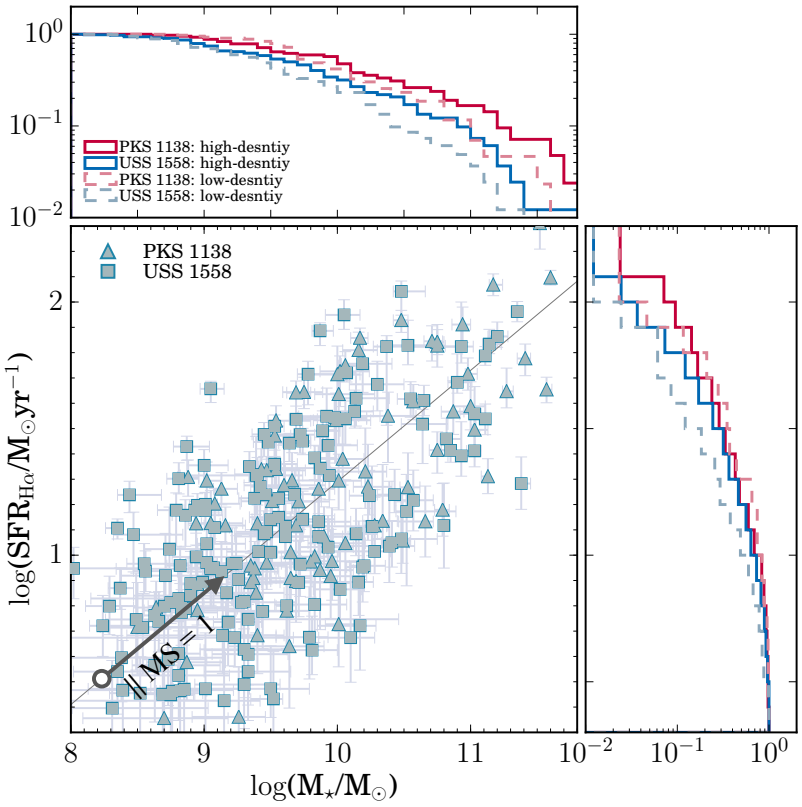

Figure 5.3: Stellar mass versus dust-corrected SFR from Hα luminosities. Triangles and squares are HAEs in PKS 1138 and USS 1558, respectively. Those 1σ errors are presented by individual errorbars. The upper and right panels represent the normalised cumulative distributions of stellar mass and SFR, respectively. Red solid and dashed lines indicate HAEs in PKS 1138 in high/low density regions (divided at the median value of $\langle a \rangle_{5\text{th}}$ = 214 ph-kpc, respectively. Blue solid and dashed lines show HAEs in USS 1558 in high/low density regions (divided at the median value of $\langle a \rangle_{5\text{th}}$ = 164 ph-kpc, respectively.

AGN feedback (Dekel & Birnboim, 2006; Sijacki et al., 2007). Moreover, in such conditions in massive haloes, star-forming satellites falling into them cannot accrete or retain the cold gas due to the environmental effects such as strangulation or ram pressure stripping. Those star-formation activities can no longer be sustained, and are eventually quenched due to a lack of gas reservoirs (environmental quenching; Peng et al. 2010b). However, our HAE samples in both PKS 1138 and USS 1558 do not show significant deficits of low-mass star-forming galaxies in high-density regions. Although it could suggest that the environmental quenching of low-mass galaxies would have minor impact at high redshifts, it is too early to conclude so because our narrowband data do not sufficiently cover the star-forming objects down to low SFR and low Hα line EW (< 30 Å).

On the other hand, dense substructures in USS 1558 would be still efficiently fed by cold accretions which is actually seen as strong Lyα depletion as described in the next section. Therefore, massive star-forming galaxies can have bluer colours and retain vigorous star-formation even in the higher-density regions in USS 1558. Indeed, we find that the high-density regions and the densest group in USS 1558 are occupied by a lager number of

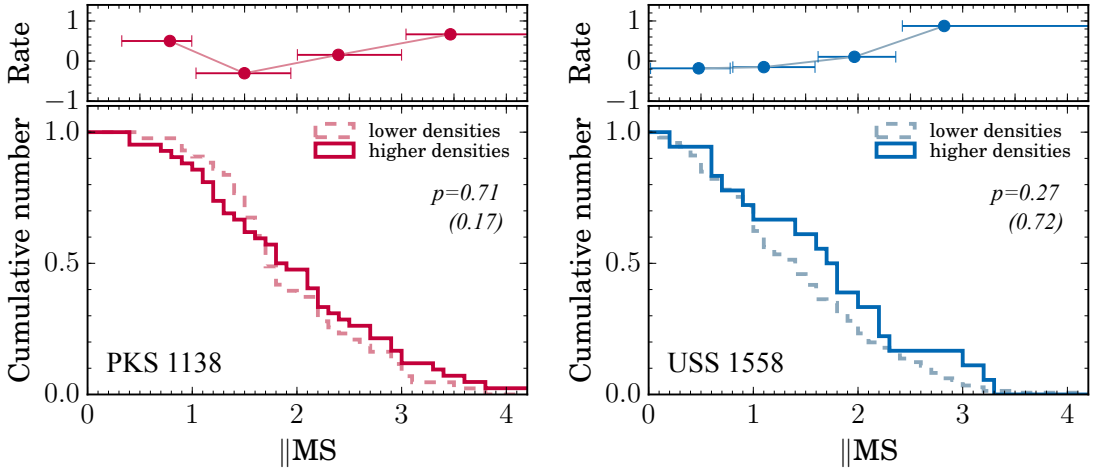

Figure 5.4: Normed cumulative distribution of ||MS. Left and right figures show the result in PKS 1138 and USS 1558, respectively. Solid and dashed lines indicate cumulative functions of HAEs separated to lower and higher halves in terms of 5th mean distance. These are divided at $\langle a \rangle_{5\mathrm{th}}$ = 214 and 164 ph-kpc (corresponding to the median values), respectively. p-values from the KS test are shown in the inset of each panel. The numbers enclosed by the parentheses are derived for the mass-control sample ($M_\star > 10^{9.6}$ and $> 10^{9.4}$ $M_\odot$ for PKS 1138 and USS 1558, respectively). The upper panels represent the excess rates of the number of HAEs in high-density regions relative to those in low-density regions at each ||MS bin for PKS 1138 and USS 1558, respectively.

more massive and more active star-forming galaxies. These results strongly support this scenario.

5.3 Lyα depletion in overdense groups

Based on the dual Hα and Lyα emitter survey for the same protocluster field at $z = 2.5$, we have found that LAEs are missing in the dense HAE groups. We also find that the escape fractions of Lyα photons in the composite HAEs in high-density regions are lower than those in lower-density regions. In the general field, LAEs are thought to have less dust and lower HI covering fractions (Shibuya et al., 2014; Reddy et al., 2016b) and the Lyα photons can easily escape from the galaxies. On the other hand, in the dense protocluster environment, extra surrounding gas and dust components trapped in the group/cluster scale haloes may prevent the Lyα photons from escaping from the systems. Such ambient dense cold gas in group/cluster-scale haloes may be supplied from the surrounding regions, for example, by cold-mode stream along the filamentary structures (Dekel et al., 2009a,b; van de Voort et al., 2011). Galaxy–CGM/IGM connection is one of the key aspects to understanding galaxy formation at high redshifts, since most of the galaxies are likely to be formed through cold-mode gas accretion at high redshifts (Kereš et al., 2005), which help galaxies to grow into very massive galaxies as observed in the today's Universe (Dekel et al., 2009a,b). Although we are still unsure if the Lyα depletion effect results from the dense cold gas associated with the massive protocluster cores, this hypothesis is comfortably consistent with the mass and/or SFR offsets seen in the high-density regions in the protoclusters based on the comparison of the cumulative distributions functions (§4.1.4).

In addition, because the mean projected distance of HAEs is much smaller ($\lesssim 150$ ph-kpc) in higher-density regions than in the lower-density regions, Lyα photons escaped from a HAE have a higher chance of penetrating CGM associated to other member galaxy(ies) in the foreground located along the line of sight, and thus they can be more depleted. This scenario is indistinguishable from the one in the previous paragraph by using the narrowband data alone. To resolve these two plausible effects, a deep, rest-frame FUV spectroscopy of the protocluster galaxies with LRIS and/or KCWI on Keck telescope will be helpful, which can constrain the physical origins of the Lyα depletion effect (see the future work in §6).

Otherwise, most of the individual galaxies in the dense cores could originally have lower Lyα photon escape fractions due for example to higher dust extinction by some environmental effect (Koyama et al., 2013a,b; Hatch et al., 2017). Actually, HAEs in higher-density regions tend to be dustier according to the SED-inferred E(B−V) as presented in Fig. 5.5, and yet the difference of E(B−V) between HAEs in high-density and low-density regions is not statistically significant ($p = 0.06$–0.07 according to the KS test). In particular, we see only ~ 10 per cent of HAEs have E(B−V) lower than 0.2 mag, while ~ 30 per cent of HAEs in lower-density regions have such lower amount of dust extinction. Since a large fraction of HAEs+LAEs have significantly lower dust reddening as compared to the HAE samples (Fig. 5.5), the discrepancy of dust reddening of individual HAEs between high and low density regions may be sufficient to explain the deficiency of LAEs in the dense group cores. Therefore, we cannot rule out the dust extinction effect on the Lyα depletion in the dense group cores. However, the scenario that dense CGM/IGM matters in the protocluster's core deplete Lyα emission line is more preferred if we take into account the observed enhancement of SFR in high-density regions in USS 1558.

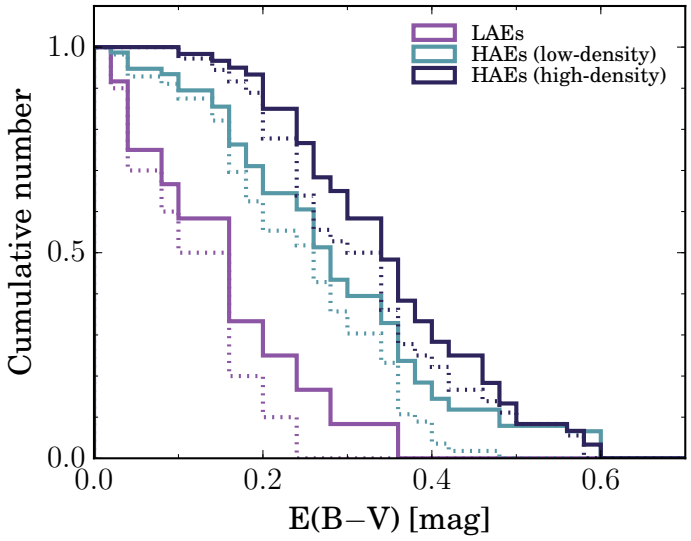

Figure 5.5: Normed cumulative distribution of E(B−V). The black, blue, and purple lines show the HAE samples in high-density regions ($\langle a \rangle_{5\mathrm{th}} < 150$ ph-kpc), those in lower-density regions ($\langle a \rangle_{5\mathrm{th}} > 150$ ph-kpc), and HAEs+LAEs. Here, we only use flux-limited samples with $f_{\mathrm{H}\alpha} \geq 1.347$ erg s^{-1}cm^{-2}, which is tailored to the samples used for the stacking analysis (see §4.2.2). It should be noted that even if we employ the entire HAE samples, the statistical trends remain consistent. The dashed lines indicate cumulative functions for HAEs limited by the stellar mass $< 10^{10}$ M$_{\odot}$.

Furthermore, our dual Lyα and Hα line survey of a protocluster at $z = 2.5$ has reported a broad agreement in the spatial distributions between LAEs and HAEs on a large scale ($\gtrsim 10$ co-moving Mpc). This indicates that Lyα line would be a good tracer of LSSs in the high-z Universe. In other words, we can effectively search for and discover protocluster candidates at $z > 2$ by targeting LAEs as tracers with optical imager and spectrograph with much wider field of views than those at near-infrared. HSC and PFS on the Subaru Telescope are quite powerful to conduct such surveys.

On a smaller scale, however, we find that LAEs, except for the RG, are totally missing in the protocluster's dense cores, which are well traced by HAEs at the same redshift as significant overdensities. This suggests that the LAE surveys of protoclusters (e.g. Ouchi et al. 2005; Venemans et al. 2007; Yamada et al. 2012; Wylezalek et al. 2013) would inevitably miss the particularly dense structures in protoclusters which are thought to be the most interesting and important environments where we expect to identify any early environmental effects as the progenitors of today's very massive cluster cores. Therefore, we will not really be able to investigate environmental effects with LAEs alone as they can trace only the outskirts of protocluster cores or even larger-scale structures around them. This means that it is very hard to search for truly dense structures at $z > 2.6$ since Hα is no longer available at such high redshifts. To overcome this situation, the James Webb Space Telescope (Gardner et al., 2006) launched in the near future will be powerful as it probes the rest-frame optical regime where many nebular emission lines other than Lyα are located. On the other hand, we should note that bright Lyα blobs can be also used as a tracer of the central galaxies in massive haloes as suggested by the past studies (e.g. Steidel et al. 2000; Matsuda et al. 2009, 2011a; Hennawi et al. 2015; Cai et al. 2016b).

5.4 Co-evolution of galaxies and environments

Cluster galaxies are formed within large-scale structures including cores, filaments/sheets, and voids as simulated by ΛCDM cosmological simulations (Bullock et al., 2001; Springel & Hernquist, 2003; Springel et al., 2005; Guo et al., 2011). The modern hydrodynamical cosmological simulations predict that the cold gas accretion that controls the gas supply process, strongly depends on halo mass and redshift (Kereš et al., 2005, 2009; Dekel et al., 2009a,b), which is especially complicated at the redshift interval of $z \simeq 2$–3. Within this framework, galaxies and environments "co-evolve" through the structure growth, mass and gas assembly, and subsequent star-formation activities. Thus, the physical properties of CGM associated with the protocluster core is critically important in determining the destiny of cluster galaxies therein.

In the forming massive haloes associated with the protocluster, initially cold gas streams would penetrate towards the centre of the haloes through hot media (Dekel et al., 2009a,b; van de Voort et al., 2011), which then lead to formation and growth of massive galaxies even in such massive protocluster's cores. This can be expected to occur in massive structures at high redshifts which still retain rich cold gas reservoirs (Dekel et al., 2009a). Our finding of lower escape fraction of Lyα photons in the dense group cores in USS 1558 at $z = 2.53$ is consistent with this scenario, since the depletion effect of Lyα emission line would be due to high covering fraction of dense cold gas clouds associated with the protocluster cores. Indeed, HAEs in USS 1558 tend to have higher SFRs in the high-density regions, and we see the enhancements in both SFR and stellar mass of HAEs in the densest group in USS 1558, which have not been seen in cluster environments at $z \lesssim 2$ (Butcher & Oemler, 1984; Finn et al., 2005; Koyama et al., 2010, 2011; Smail et al., 2014; Shimakawa et al., 2014; Clements et al., 2014; Kato et al., 2016). These unique trends also support our implications, and suggest that they are still in the mid of forming massive star-forming galaxies intensively in the protocluster cores fed by cold gas accretions. On the other hand, no difference in the deviation from the main sequence (ΔMS) between higher and lower density regions within the protoclsuters would imply that strong external environmental effects such as galaxy-galaxy interactions may be less important in boosting the star-forming activities in the protocluster cores at $z > 2$.

After consuming the cold gas intensively by star-formation (with some dusty starburst events induced by galaxy-galaxy mergers), and also after the growth of halo masses of the clusters ($\gtrsim 1 \times 10^{14}$ M$_\odot$), star-forming activities would begin to decline, and then a red sequence is built up and emerging as seen in PKS 1138 at $z = 2.15$ (Kodama et al., 2007; Koyama et al., 2013a,b; Hatch et al., 2017). We see the number excess of massive and red HAEs in the high-density regions in PKS 1138, which is different from what we see in the high-density regions in USS 1558. These massive and red HAEs would be the progenitors of early-type galaxies seen at the bright end of the red sequence seen in today's galaxy clusters (Gladders & Yee, 2000; Thomas et al., 2005; Koester et al., 2007; Stott et al., 2009; Cappellari et al., 2011). At the later stage of cluster growth at $z \leq 2$, the SFR densities in the (proto)cluster cores start to decline sharply at a rate of $(1+z)^{6-7}$ (Smail et al., 2014; Shimakawa et al., 2014; Clements et al., 2014; Kato et al., 2016), and the protoclusters will eventually grow into rich, inactive galaxy clusters in the present-day Universe like the Coma cluster.

6 | Summary

Protocluster environments at the cosmic high noon era (z = 2–3) is the ideal laboratory to investigate the environmental dependence of galaxy formation and gas feeding mechanism in the protocluster cores. We have carried out two observing programs to resolve these problems. The following items briefly summarise all the results we have obtained in this *Thesis*.

— Based on the deep Hα line imaging of the two known protoclusters (PKS 1138 at z = 2.2 and USS 1558 at z = 2.5) with MOIRCS on the Subaru Telescope, we have succeeded in constructing large samples HAEs (85 and 164, respectively). Such a very high density sampling allows us to map sub-structures down to the several hundred physical kpc scale for the first time. A follow-up Lyα line imaging for USS 1558 with the Suprime-Cam on Subaru enables us to collect 162 LAE candidates associated with the large-scale structures in and around USS 1558 protocluster region, of which 13 are overlapped with HAEs and thus confirmed.

— Thanks to the deep Hα imaging, we collect total of 249 HAE samples down to the stellar mass of 1×10^8 $M_\odot$ and SFR of 2 $M_\odot$/yr. By comparing galaxy properties as a function of mean projected distance (or number density), we find that the protoclusters' dense cores tend to have larger numbers of more massive and/or more active star-forming galaxies, although they are not clearly deviated from the star-forming main sequence. On the other hand, dependencies of the physical properties on the environment are diverse among different cluster/group structures. This may suggest that the environmental effects on galaxy formation depend on the stage of cluster/group formation and evolution in the course of the cosmic mass-assembly history.

— Our deep Hα line imaging have identified as many as 54 less massive HAEs with stellar mass $< 1 \times 10^9$ $M_\odot$ down to the SFR limit of $\sim$ 2 $M_\odot$/yr. Some of those have quite high SFRs $\sim$ 10 $M_\odot$/yr for their stellar mass, corresponding to the specific SFRs $\sim$ (0.1 Gyr)$^{-1}$. Thus, those are young star-bursts in the protocluster regions. Furthermore, we find a tight correlation between their Hα/UV flux ratios and specific SFRs, perhaps suggesting that they have exceptionally hard ionisation fields due to their young ages and low metallicities.

— Our panoramic mapping of LAEs in USS 1558 has identified large-scale structures around the global density peak which nicely coincides with the protocluster core

identified by numerous HAEs associated to the radio galaxy. On much smaller scales, however, LAEs are remarkably missing in the densest regions traced by HAEs, and the fraction of LAEs among the HAEs is only one per cent in the higher density regions in USS 1558, which is an order of magnitude lower than that in lower density regions. On top of that, the stacked line images of HAEs divided into higher and lower density groups show that the escape fraction of Lyα photons in the high density regions is lower, suggesting that denser circumgalactic/intergalactic matters may severly deplete the Lyα line emission from star-forming galaxies in the protocluster cores.

— Based on all these results presented in this *Thesis*, we conclude that the densest regions at $z = 2$–3 are indeed hosting the formation of the progenitors of massive galaxies that grow into early-type galaxies at the bright end of the red sequence commonly seen in the present-day galaxy clusters. The young protocluster cores without a prominent red sequence are probably in the mid of vigorous accretion of cold gas (cold streams) as predicted by the modern cosmological simulations, since we find the clear depletion effect of Lyα emission lines there. Our first systematic combined analysis of both Hα and Lyα lines in the protocluster environments have provided us with new insights into the physical mechanisms of galaxy formation in the the early phase of galaxy cluster assembly.

7 | Future prospects

Our Hα line imaging of the two known dense protoclusters, PKS 1138 ($z = 2.15$) and USS 1558 ($z = 2.53$) and follow-up Lyα observation of USS 1558 infer vigorous star-formation activities of massive galaxies in the dense cores due to rich cold gas fed by cold streams as predicted by the modern cosmological simulations. However, the results are based on only two protocluster samples, which are certainly insufficient to establish a general picture of cluster formation and galaxy formation therein at high redshifts. The following section describes outstanding issues and our future plans to address these problems.

7.1 Future of MAHALO-DEEP

There are some immediate objectives left for us to study based on our unique statistical HAE samples taken by the deep Hα imaging, such as

1. Stellar mass and luminosity functions, and
2. Size measurements by using HST data.

(1) Analyses of stellar mass function in the protocluster fields can identify the stellar mass range at which we see the number excess of galaxies in high-density regions (§4.1.3). Likewise, comparison of Hα luminosity functions across various environments will test if there is any environmental dependence of star-forming activities. These work will be performed immediately after the *Thesis*.

(2) Size estimation of UV and stellar components of HAEs in the protoclusters, and comparison of the measured sizes across the environment are also important to constrain the environmental dependence of size growth histories at high redshifts. For example, overdense environments would involve higher chance of galaxy mergers (Okamoto & Habe, 2000; Gottlöber et al., 2001). These merger events are likely to change the size growth rate as a function of total stellar mass. Specifically, it is expected that major mergers and minor mergers increase the effective radii of stellar components scaled as $\delta\log(r_e)/\delta\log(M_\star) \sim 1$ and 2, respectively (Bezanson et al., 2009; Naab et al., 2009; van Dokkum et al., 2010). Mergers would also drive the gas towards the centre and lead to more centrally concentrated star-formation. Mass and size evolution in high density regions still remain poorly understood (Papovich et al., 2012), especially at $z > 2$. We have F485/814W and F814/160W data in PKS 1138 and USS 1558, respectively, which allow us to derive the sizes of rest-frame UV for the HAEs in PKS 1138, and those of both rest-frame UV and optical light for the HAEs in USS 1558, based on the model profile fitting technique such as GALFIT (Peng et al., 2010a).

7.2 Future of follow-up spectroscopy

We are extending the intensive narrowband line search (MAHALO-Subaru) to the systematic follow-up spectroscopic survey named CHEERS-MAHALO (*Cosmic History of Environmental Effects Revealed by Spectroscopy*), led by RS. We have carried out deep spectroscopic observations with MOIRCS on the Subaru Telescope, and in recent times, with MOSFIRE on the Keck telescope since it has a much greater sensitivity than any other similar instruments today. Deep near-infrared spectroscopy allows us to detect multi-emission lines emitted from HII regions in star-forming galaxies. We can then study the early phase of environmental dependence of physical properties of the ionised gas in protocluster galaxies such as gas-phase metallicity and ionisation parameters derived from the (semi-)empirical line diagnostics (Osterbrock, 1974; Zaritsky et al., 1994; Kewley & Dopita, 2002; Kobulnicky & Kewley, 2004; Tremonti et al., 2004; Nagao et al., 2006; Maiolino et al., 2008; Levesque & Richardson, 2014; Dopita et al., 2016).

First of all, there could be an environmental dependence of the time-scale of galaxy formation and evolution because of hierarchical clustering formation; overdense environments such as galaxy clusters start off from the highest density peaks in the early Universe which must collapse first. Such an intrinsic (nature) effect may lead galaxy formation and evolution to proceed earlier and/or faster. This also applied to the chemical evolution (Genel, 2016). Such nature effect may particularly affect galaxy downsizing (mass-dependent time-scale of galaxy formation and evolution; Cowie et al. 1996; Cattaneo et al. 2008) in the sense that the downsizing proceeds earlier in the protocluster regions. This would especially enhance gas-phase metallicities of low-mass systems in overdense environments as compared to those at the same stellar mass in the general fields.

In addition to that, the overdense environments should also affect the formation histories of satellite objects falling into the cores, since the haloes of those infalling galaxies would dramatically change from individual haloes to the cluster-scale haloes shared with massive host galaxies. This should alter the gas accretion mechanism to individual galaxies due to the big changes in dynamical and cooling timescales. Moreover, the gas outflow process from galaxies is also dependent on galaxy mass and surrounding environment since dense intergalactic medium may drive the outflowing gas back into the systems (Oppenheimer & Davé, 2008; Davé et al., 2011). Such biased gaseous feeding/feedback mechanisms in dense environments ought to directly affect the chemical evolution of cluster galaxies as suggested by the modern cosmological simulations (Davé et al. 2011; Bahe et al. 2016, but see Genel 2016) and observations (Kulas et al., 2013; Shimakawa et al., 2015a; Valentino et al., 2015).

So far, we have carried out the spectroscopic follow-up survey of HAEs in PKS 1138 and USS 1558 with MOIRCS. We have succeeded in identifying one or more emission lines of 60 individual HAEs. We then estimate gas-phase metallicities of the HAEs in the protocluster regions, and find the enhancement of chemical enrichments in the low-mass regime on the mass-metallicity relation compared to the counterparts in the general field at the same redshift (Shimakawa et al., 2015a) based on the stacking analyses. However, since these processes are rather stochastic, a considerable scatter in the chemical properties is expected, and thus, the stacking analyses is not ideal at all. With this background and motivations, our spectroscopic campaign is an on-going efforts, and we aim to obtain high S/N spectra with MOSFIRE to analyse ISM conditions in individual galaxies. It will allow

us to explore the environmental dependence of ISM properties as a function of the mean projected distance in and around the protoclusters, and also by comparing the gaseous metallicities of galaxies with those in the general fields.

7.3 Future of Lyα line analyses

Cold gas is a critically important component for galaxy formation and evolution (Kereš et al., 2005). The gas content and feeding mechanism of galaxies are thought to depend on the cosmic age, halo mass and environment, and they have significant variations in particular at the peak epoch of galaxy formation ($z = 2-3$) (Dekel et al., 2009a,b). We have discovered for the first time the prominent deficiency of LAEs in the dense HAE groups in the USS 1558 protocluster filed at $z = 2.53$. This suggests the environmental dependence of CGM/IGM properties. However, we have not yet reached a fully consistent picture from the narrowband datasets alone. In order to resolve this situation, a deep FUV spectroscopy by using such as LRIS and KCWI on the Keck telescope is highly desired. We expect that the stacking analyses of deep FUV spectra taken by such powerful instruments can detect faint FUV continuum spectra and hydrogen absorption features, which allow us to constrain HI covering fractions and HI column densities of the protocluster galaxies as demonstrated for the field galaxies at the similar redshifts (Reddy et al., 2016a,b).

In the meanwhile, we are also working on the analyses of Lyα line imaging at $z > 2$ with the Hyper Suprime-Cam (HSC; Miyazaki et al. 2012) on the Subaru Telescope. This is one of the hundreds of projects branched from the Subaru Strategic Program with HSC (project-151; Shimakawa et al.)[3]. In this project, we aim to conduct

1. A systematic search for Lyα absorption systems at $z > 2$, and
2. A comparison of IGM densities inferred from Lyα forests of bright background objects with the number densities of narrow-band selected LAEs.

Shimakawa et al. (2016) have tested the feasibility to identify galaxies with strong Lyα absorption ($EW_{Ly\alpha} \lesssim -10$ Å) on the basis of narrowband deficits at the Lyα wavelength. We find that this technique works pretty well to detect Lyα absorption systems (Lyα absorbers, LAAs), while this method cannot trace typical star-forming galaxies that have the Lyα line EW of around zero Å. The narrowband (NB387) observations are now on-going with HSC in the XMM-LSS, COSMOS, DEEP2, and ELAIS fields, where we will perform these analyses to discover LAAs at $z = 2.2$.

In XMM-LSS, COSMOS and DEEP2 among the survey fields, a large spectral library of high-z QSOs taken by SDSS/BOSS survey is also available. This allows us to map out IGM densities at $z > 2$ along the line of sights of those bright high-z QSOs by the Lyα forest analyses (Lynds, 1971; Fan et al., 2006b; Meiksin, 2009) based on the Lyα forest catalogue of the SDSS-III/BOSS survey distributed by Lee et al. (2013). Therefore, we can compare the IGM densities at $z = 2.2$ in the background QSO sight lines with the number densities of LAEs and LAAs at $z = 2.2$ traced by the HSC narrow-band surveys, and we can investigate the spatial correlations between IGM densities and galaxy densities statistically. For example, to estimate IGM transmissions at the narrow redshift slice traced by the NB387 filter installed on HSC, we can use the background QSOs at $z = 2.2815$–2.6860 since

those Lyα forest spectra (λ = 1041–1185 Å) all fall within the filter FWHM where most of LAEs are expected to be selected. 140 QSOs can meet this criterion, which is a large enough to investigate the relationships between galaxy number densities and associated IGM densities.

7.4 Future of protocluster science

To resolve environmental effects on galaxy formation at high redshfit, we still have some big remaining problems:

– Galaxy selection bias,

– Difficulty in quantifying cluster/group scales and masses, and

– Shortage of high-z protocluster samples.

So far, while lots of high-z (proto)cluster searches have been performed, we have always been suffering from galaxy selection biases at different fields and redshifts as actually noted by this *Thesis* for the selection bias between LAEs and HAEs. Other than that, for example, Balmer break galaxies are preferentially used as tracers for low-z galaxy cluster surveys (Kodama & Bower, 2001). On the other hand, Lyman break galaxies (Steidel et al., 1998) are alternative sign-spots at high redshifts. In addition to that, we cannot ignore galaxy formation and evolution themselves, which also affect galaxy selection biases at different redshifts, since for example Lyman Break galaxies at high redshifts must not stay as they are down to the present-day. Moreover, restricted survey areas due to the observational limitation insufficiently resolve the cosmic variance, which complicates the quantification of galaxy over(under) densities. Also, it is hard to identify rare massive protoclusters by such a limited survey volume. All those biases and restrictions have resulted in vague definitions of "protocluster". Indeed, the definition of protocluster is totally incoherent among different research groups. These issues seriously prevent us from identifying physical origins of early environmental effects on galaxy formation. A more complete search of high-z matter overdensities with a larger survey volume is strongly desired.

Cosmological network system known as the "cosmic web" consisting of filaments, sheets, and clusters is considered to be originated from gravitational instability that started from the initial density fluctuations (Bond et al., 1996). Cold gas is considered to naturally follow such mass-assembly histories over a large scale, and thus the density of intervening HI gas should reflect the cosmic matter density, namely environment (Kollmeier et al., 2003). Therefore, IGM densities derived from the Lyα forest analyses is the most effective and unbiased quantity to define over(under)-dense environments "independent of galaxy selection bias". Indeed, some past studies have successfully found that the galaxy locations clearly coincide with the regions which have higher IGM absorptions (Lee et al., 2016). Recently, Cai et al. (2016a) have developed a novel approach for identifying the extreme tails of matter distribution. This utilizes the large library of quasar spectra from the SDSS-III/BOSS survey to search for extremely rare, coherently strong IGM Lyα absorption ($> 4\sigma$

[3] http://hsca.ipmu.jp/hsc/projects/cgi-bin/projects.pl?action=display_project;number=151

in the optical depth) at the scales of 20–30 h^{-1} comoving Mpc (cMpc). Combined with cosmological simulation (Peirani et al., 2014), those are expected to trace very massive overdensities of halo masses greater than 10^{14} $M_{\odot}$. By examining 160k quasar spectra, their survey volume reaches to 1 $(h^{-1}\ \mathrm{Gpc})^3$, by an order of magnitude larger than any other competitive surveys, enabling the first ever unbiased protocluster search at $z > 2$. In the near future, this sort of large protocluster search will be able to overcome the issues that we curently have, and to take a step closer to a full explanation of galaxy diversity depending on the environment.

Acknowledgements

I am grateful to Taddy Kodama at NAOJ for his memorable supervision in my research life. I acknowledge Ikuru Iwata, Saeko Hayashi, Daisuke Iono at NAOJ, Kouji Ohta at Kyoto University, and Takashi Okamoto at Hokkaido University for their reviewing of this *Thesis*. I also thank Nobunari Kashikawa at NAOJ for his reviewing of my progress report and giving me useful comments.

I thank Ken-ichi Tadaki at MPE, Masao Hayashi, Masatoshi Imanishi at NAOJ, Yusei Koyama, Ichi Tanaka, and Masato Onodera at Subaru Telescope for very useful comments and advisement that improved this *Thesis*. Then, I mahalo Subaru folks, especially Kentaro Aoki and Nobuo Arimoto in Hilo, Hawaii where I had wonderful stay for two years. I thank Tomoko L. Suzuki, Moegi Yamamoto, and many colleagues and staffs at Subaru, NAOJ, and SOKENDAI for the assistance and discussions over the five years while this Thesis work was conducted.

This *Thesis* is grounded on the data collected at the Subaru Telescope, which is operated by the National Astronomical Observatory of Japan. This work is also based on observations taken by the 3D-HST Treasury Program (GO 12177 and 12328) with the NASA/ESA HST, which is operated by the Association of Universities for Research in Astronomy, Inc., under NASA contract NAS5-26555. This work is subsidized by JSPS KAKENHI Grant Number 15J04923, and is also partially supported by the Research Fund for Students (2013) of the Department of Astronomical Science, SOKENDAI (the Graduate University for Advanced Studies). Data analysis was in part carried out on a common use data analysis computer system at the Astronomy Data Center, ADC, of the National Astronomical Observatory of Japan. RS acknowledges the financial support from the Japan Society for the Promotion of Science (JSPS) through JSPS research fellowships for young scientists.

Bibliography

Abadi M. G., Moore B., Bower R. G., 1999, MNRAS, 308, 947

Abazajian K. N., et al., 2009, ApJS, 182, 543

Abell G. O., Corwin Jr. H. G., Olowin R. P., 1989, ApJS, 70, 1

Adelberger K. L., Steidel C. C., Shapley A. E., Hunt M. P., Erb D. K., Reddy N. A., Pettini M., 2004, ApJ, 607, 226

Adelberger K. L., Shapley A. E., Steidel C. C., Pettini M., Erb D. K., Reddy N. A., 2005, ApJ, 629, 636

Aird J., et al., 2010, MNRAS, 401, 2531

An F. X., et al., 2014, ApJ, 784, 152

Andrews B. H., Martini P., 2013, ApJ, 765, 140

Bahe Y. M., Schaye J., Crain R. A., McCarthy I. G., Bower R. G., Theuns T., McGee S. L., Trayford J. W., 2016, preprint, (arXiv:1609.03379)

Baldry I. K., Glazebrook K., Brinkmann J., Ivezić Ž., Lupton R. H., Nichol R. C., Szalay A. S., 2004, ApJ, 600, 681

Baldry I. K., Balogh M. L., Bower R. G., Glazebrook K., Nichol R. C., Bamford S. P., Budavari T., 2006, MNRAS, 373, 469

Baldwin J. A., Phillips M. M., Terlevich R., 1981, PASP, 93, 5

Bamford S. P., et al., 2009, MNRAS, 393, 1324

Barden M., Häußler B., Peng C. Y., McIntosh D. H., Guo Y., 2012, MNRAS, 422, 449

Barnes J. E., Hernquist L., 1996, ApJ, 471, 115

Barro G., et al., 2016, ApJ, 827, L32

Becker G. D., Rauch M., Sargent W. L. W., 2007, ApJ, 662, 72

Behroozi P. S., Wechsler R. H., Conroy C., 2013a, ApJ, 770, 57

Behroozi P. S., Marchesini D., Wechsler R. H., Muzzin A., Papovich C., Stefanon M., 2013b, ApJ, 777, L10

Bekki K., 2014, MNRAS, 438, 444

Bell E. F., et al., 2004, ApJ, 608, 752

Bertin E., Arnouts S., 1996, A&AS, 117, 393

Best P., et al., 2010, preprint, (arXiv:1003.5183)

Bezanson R., van Dokkum P. G., Tal T., Marchesini D., Kriek M., Franx M., Coppi P., 2009, ApJ, 697, 1290

Birnboim Y., Dekel A., 2003, MNRAS, 345, 349

Birnboim Y., Dekel A., Neistein E., 2007, MNRAS, 380, 339

Blumenthal G. R., Faber S. M., Primack J. R., Rees M. J., 1984, Nature, 311, 517

Bond J. R., Kofman L., Pogosyan D., 1996, Nature, 380, 603

Booth C. M., Schaye J., 2009, MNRAS, 398, 53

Boselli A., Gavazzi G., 2006, PASP, 118, 517

Bothwell M. S., Maiolino R., Kennicutt R., Cresci G., Mannucci F., Marconi A., Cicone C., 2013, MNRAS, 433, 1425

Botticella M. T., et al., 2008, A&A, 479, 49

Bouché N., et al., 2010, ApJ, 718, 1001

Bouché N., Murphy M. T., Kacprzak G. G., Péroux C., Contini T., Martin C. L., Dessauges-Zavadsky M., 2013, Science, 341, 50

Bournaud F., Jog C. J., Combes F., 2007, A&A, 476, 1179

Bouwens R. J., et al., 2011, ApJ, 737, 90

Bouwens R. J., et al., 2012, ApJ, 754, 83

Bower R. G., Kodama T., Terlevich A., 1998, MNRAS, 299, 1193

Brinchmann J., Charlot S., White S. D. M., Tremonti C., Kauffmann G., Heckman T., Brinkmann J., 2004, MNRAS, 351, 1151

Brinchmann J., Pettini M., Charlot S., 2008, MNRAS, 385, 769

Brocklehurst M., 1971, MNRAS, 153, 471

Bruzual G., Charlot S., 2003, MNRAS, 344, 1000

Bullock J. S., Kolatt T. S., Sigad Y., Somerville R. S., Kravtsov A. V., Klypin A. A., Primack J. R., Dekel A., 2001, MNRAS, 321, 559

Bunker A. J., Warren S. J., Hewett P. C., Clements D. L., 1995, MNRAS, 273, 513

Butcher H., Oemler Jr. A., 1984, ApJ, 285, 426

Cai Z., et al., 2016b, preprint, (arXiv:1609.04021)

Cai Z., et al., 2016a, preprint, (arXiv:1609.02913)

Calzetti D., 2001, PASP, 113, 1449

Calzetti D., Armus L., Bohlin R. C., Kinney A. L., Koornneef J., Storchi-Bergmann T., 2000, ApJ, 533, 682

Cano-Díaz M., Maiolino R., Marconi A., Netzer H., Shemmer O., Cresci G., 2012, A&A, 537, L8

Cappellari M., et al., 2011, MNRAS, 416, 1680

Cardelli J. A., Clayton G. C., Mathis J. S., 1989, ApJ, 345, 245

Carilli C. L., Walter F., 2013, ARA&A, 51, 105

Carilli C. L., Harris D. E., Pentericci L., Rottergering H. J. A., Miley G. K., Bremer M. N., 1998, ApJ, 494, L143

Carilli C. L., Harris D. E., Pentericci L., Röttgering H. J. A., Miley G. K., Kurk J. D., van Breugel W., 2002, ApJ, 567, 781

Cattaneo A., et al., 2007, MNRAS, 377, 63

Cattaneo A., Dekel A., Faber S. M., Guiderdoni B., 2008, MNRAS, 389, 567

Cattaneo A., et al., 2009, Nature, 460, 213

Cerviño M., Bongiovanni A., Hidalgo S., 2016, A&A, 589, A108

Chabrier G., 2003, PASP, 115, 763

Chapman S. C., Blain A. W., Smail I., Ivison R. J., 2005, ApJ, 622, 772

Chiang Y.-K., Overzier R., Gebhardt K., 2014, ApJ, 782, L3

Chiang Y.-K., et al., 2015, ApJ, 808, 37

Cicone C., et al., 2014, A&A, 562, A21

Clements D. L., et al., 2014, MNRAS, 439, 1193

Coil A. L., et al., 2015, ApJ, 801, 35

Cole S., Lacey C. G., Baugh C. M., Frenk C. S., 2000, MNRAS, 319, 168

Cooke E. A., Hatch N. A., Muldrew S. I., Rigby E. E., Kurk J. D., 2014, MNRAS, 440, 3262

Costa T., Sijacki D., Haehnelt M. G., 2014, MNRAS, 444, 2355

Couch W. J., Ellis R. S., Sharples R. M., Smail I., 1994, ApJ, 430, 121

Cowie L. L., Songaila A., Hu E. M., Cohen J. G., 1996, AJ, 112, 839

Cresci G., Mannucci F., Maiolino R., Marconi A., Gnerucci A., Magrini L., 2010, Nature, 467, 811

Croft S., Kurk J., van Breugel W., Stanford S. A., de Vries W., Pentericci L., Röttgering H., 2005, AJ, 130, 867

Cucciati O., et al., 2012, A&A, 539, A31

Daddi E., et al., 2007a, ApJ, 670, 156

Daddi E., et al., 2007b, ApJ, 670, 173

Daddi E., et al., 2010, ApJ, 713, 686

Dahlen T., et al., 2004, ApJ, 613, 189

Dahlen T., Mobasher B., Dickinson M., Ferguson H. C., Giavalisco M., Kretchmer C., Ravindranath S., 2007, ApJ, 654, 172

Dannerbauer H., et al., 2014, A&A, 570, A55

Darg D. W., et al., 2010, MNRAS, 401, 1552

Davé R., Finlator K., Oppenheimer B. D., 2011, MNRAS, 416, 1354

Davis M., Efstathiou G., Frenk C. S., White S. D. M., 1985, ApJ, 292, 371

Davis T. A., et al., 2014, MNRAS, 444, 3427

Dayal P., Ferrara A., Dunlop J. S., 2013, MNRAS, 430, 2891

De Lucia G., Springel V., White S. D. M., Croton D., Kauffmann G., 2006, MNRAS, 366, 499

Dekel A., Birnboim Y., 2006, MNRAS, 368, 2

Dekel A., Birnboim Y., 2008, MNRAS, 383, 119

Dekel A., et al., 2009a, Nature, 457, 451

Dekel A., Sari R., Ceverino D., 2009b, ApJ, 703, 785

Dey A., Lee K.-S., Reddy N., Cooper M., Inami H., Hong S., Gonzalez A. H., Jannuzi B. T., 2016, ApJ, 823, 11

Doherty M., et al., 2010, A&A, 509, A83

Dopita M. A., Kewley L. J., Sutherland R. S., Nicholls D. C., 2016, Ap&SS, 361, 61

Dressler A., 1980, ApJ, 236, 351

Dressler A., Oemler Jr. A., Butcher H. R., Gunn J. E., 1994, ApJ, 430, 107

Dressler A., et al., 1997, ApJ, 490, 577

Eisenstein D. J., et al., 2011, AJ, 142, 72

Elbaz D., et al., 2007, A&A, 468, 33

Eldridge J. J., Stanway E. R., 2012, MNRAS, 419, 479

Eldridge J. J., Langer N., Tout C. A., 2011, MNRAS, 414, 3501

Ellingson E., Lin H., Yee H. K. C., Carlberg R. G., 2001, ApJ, 547, 609

Ellison S. L., Simard L., Cowan N. B., Baldry I. K., Patton D. R., McConnachie A. W., 2009, MNRAS, 396, 1257

Ellison S. L., Patton D. R., Simard L., McConnachie A. W., Baldry I. K., Mendel J. T., 2010, MNRAS, 407, 1514

Emsellem E., et al., 2011, MNRAS, 414, 888

Erb D. K., Shapley A. E., Steidel C. C., Pettini M., Adelberger K. L., Hunt M. P., Moorwood A. F. M., Cuby J.-G., 2003, ApJ, 591, 101

Erb D. K., Shapley A. E., Pettini M., Steidel C. C., Reddy N. A., Adelberger K. L., 2006a, ApJ, 644, 813

Erb D. K., Steidel C. C., Shapley A. E., Pettini M., Reddy N. A., Adelberger K. L., 2006b, ApJ, 647, 128

Fabian A. C., 2012, ARA&A, 50, 455

Fakhouri O., Ma C.-P., 2009, MNRAS, 394, 1825

Fan X., Carilli C. L., Keating B., 2006a, ARA&A, 44, 415

Fan X., et al., 2006b, AJ, 132, 117

Fillingham S. P., Cooper M. C., Pace A. B., Boylan-Kolchin M., Bullock J. S., Garrison-Kimmel S., Wheeler C., 2016, MNRAS, 463, 1916

Finn R. A., et al., 2005, ApJ, 630, 206

Fitzpatrick E. L., 1999, PASP, 111, 63

Förster Schreiber N. M., et al., 2006, ApJ, 645, 1062

Förster Schreiber N. M., et al., 2009, ApJ, 706, 1364

Fox A. J., Ledoux C., Petitjean P., Srianand R., 2007, A&A, 473, 791

Fujita Y., 1998, ApJ, 509, 587

Fujita Y., 2004, PASJ, 56, 29

Fujita Y., Nagashima M., 1999, ApJ, 516, 619

Furusawa H., et al., 2008, ApJS, 176, 1

Galametz A., et al., 2013, ApJS, 206, 10

Gardner J. P., et al., 2006, Space Sci. Rev., 123, 485

Garn T., Best P. N., 2010, MNRAS, 409, 421

Gavazzi R., Adami C., Durret F., Cuillandre J.-C., Ilbert O., Mazure A., Pelló R., Ulmer M. P., 2009, A&A, 498, L33

Gawiser E., et al., 2006, ApJ, 642, L13

Gawiser E., et al., 2007, ApJ, 671, 278

Geach J. E., Smail I., Moran S. M., MacArthur L. A., Lagos C. d. P., Edge A. C., 2011, ApJ, 730, L19

Genel S., 2016, ApJ, 822, 107

Genel S., et al., 2014, MNRAS, 445, 175

Genzel R., et al., 2011, ApJ, 733, 101

Genzel R., et al., 2014a, ApJ, 785, 75

Genzel R., et al., 2014b, ApJ, 796, 7

Gilbank D. G., Gladders M. D., Yee H. K. C., Hsieh B. C., 2011, AJ, 141, 94

Gladders M. D., Yee H. K. C., 2000, AJ, 120, 2148

Gobat R., et al., 2013, ApJ, 776, 9

Goto T., et al., 2003, PASJ, 55, 739

Gottlöber S., Klypin A., Kravtsov A. V., 2001, ApJ, 546, 223

Grogin N. A., et al., 2011, ApJS, 197, 35

Gruppioni C., et al., 2013, MNRAS, 432, 23

Guaita L., et al., 2010, ApJ, 714, 255

Guaita L., et al., 2011, ApJ, 733, 114

Gunn J. E., Gott III J. R., 1972, ApJ, 176, 1

Gunn J. E., Peterson B. A., 1965, ApJ, 142, 1633

Guo Q., et al., 2011, MNRAS, 413, 101

Guo Y., et al., 2013, ApJS, 207, 24

Haehnelt M. G., Rees M. J., 1993, MNRAS, 263, 168

Hagen A., et al., 2016, ApJ, 817, 79

Hammer D., et al., 2010, ApJS, 191, 143

Hatch N. A., Overzier R. A., Kurk J. D., Miley G. K., Röttgering H. J. A., Zirm A. W., 2009, MNRAS, 395, 114

Hatch N. A., et al., 2014, MNRAS, 445, 280

Hatch N. A., Cooke E. A., Muldrew S. I., Hartley W. G., Almaini O., Conselice C. J., Simpson C. J., 2017, MNRAS, 464, 876

Hathi N. P., et al., 2016, A&A, 588, A26

Hayano Y., et al., 2010, in Society of Photo-Optical Instrumentation Engineers (SPIE) Conference Series. , doi:10.1117/12.857567

Hayashi M., Kodama T., Koyama Y., Tanaka I., Shimasaku K., Okamura S., 2010, MNRAS, 402, 1980

Hayashi M., Kodama T., Koyama Y., Tadaki K.-I., Tanaka I., 2011, MNRAS, 415, 2670

Hayashi M., Kodama T., Tadaki K.-i., Koyama Y., Tanaka I., 2012, ApJ, 757, 15

Hayashi M., Kodama T., Tanaka I., Shimakawa R., Koyama Y., Tadaki K.-i., Suzuki T. L., Yamamoto M., 2016, ApJ, 826, L28

Hayes M., et al., 2010, Nature, 464, 562

Hayward C. C., Hopkins P. F., 2015, preprint, (arXiv:1510.05650)

Hennawi J. F., Prochaska J. X., Cantalupo S., Arrigoni-Battaia F., 2015, Science, 348, 779

Hine N. K., Geach J. E., Alexander D. M., Lehmer B. D., Chapman S. C., Matsuda Y., 2016, MNRAS, 455, 2363

Holden B. P., et al., 2016, ApJ, 820, 73

Hollenbach D., McKee C. F., 1989, ApJ, 342, 306

Hollenbach D. J., Tielens A. G. G. M., 1999, Reviews of Modern Physics, 71, 173

Hopkins A. M., Beacom J. F., 2006, ApJ, 651, 142

Hopkins P. F., Richards G. T., Hernquist L., 2007, ApJ, 654, 731

Hopkins P. F., Hernquist L., Cox T. J., Kereš D., 2008, ApJS, 175, 356

Hopkins P. F., Bundy K., Hernquist L., Wuyts S., Cox T. J., 2010, MNRAS, 401, 1099

Horiuchi S., Beacom J. F., Kochanek C. S., Prieto J. L., Stanek K. Z., Thompson T. A., 2011, ApJ, 738, 154

Hubble E. P., 1926, ApJ, 64

Hubble E. P., 1936, Realm of the Nebulae

Hughes D. H., et al., 1998, Nature, 394, 241

Hughes T. M., Cortese L., Boselli A., Gavazzi G., Davies J. I., 2013, A&A, 550, A115

Ichikawa T., et al., 2006, in Society of Photo-Optical Instrumentation Engineers (SPIE) Conference Series. , doi:10.1117/12.670078

Iwata I., Ohta K., Tamura N., Ando M., Wada S., Watanabe C., Akiyama M., Aoki K., 2003, PASJ, 55, 415

Iwata I., Ohta K., Tamura N., Akiyama M., Aoki K., Ando M., Kiuchi G., Sawicki M., 2007, MNRAS, 376, 1557

Iwata I., et al., 2009, ApJ, 692, 1287

Iye M., et al., 2004, PASJ, 56, 381

Izotov Y. I., Stasińska G., Meynet G., Guseva N. G., Thuan T. X., 2006, A&A, 448, 955

Jaffé Y. L., Poggianti B. M., Verheijen M. A. W., Deshev B. Z., van Gorkom J. H., 2012, ApJ, 756, L28

Jaffé Y. L., Smith R., Candlish G. N., Poggianti B. M., Sheen Y.-K., Verheijen M. A. W., 2015, MNRAS, 448, 1715

Jaffé Y. L., et al., 2016, MNRAS, 461, 1202

Jesseit R., Cappellari M., Naab T., Emsellem E., Burkert A., 2009, MNRAS, 397, 1202

Jian H.-Y., Lin L., Chiueh T., 2012, ApJ, 754, 26

Johansson P. H., Naab T., Ostriker J. P., 2009, ApJ, 697, L38

Kacprzak G. G., et al., 2015, ApJ, 802, L26

Kacprzak G. G., et al., 2016, ApJ, 826, L11

Kajisawa M., Kodama T., Tanaka I., Yamada T., Bower R., 2006, MNRAS, 371, 577

Kampczyk P., et al., 2013, ApJ, 762, 43

Kato Y., et al., 2016, MNRAS, 460, 3861

Kauffmann G., 1996, MNRAS, 281, 487

Kauffmann G., et al., 2003, MNRAS, 346, 1055

Kauffmann G., White S. D. M., Heckman T. M., Ménard B., Brinchmann J., Charlot S., Tremonti C., Brinkmann J., 2004, MNRAS, 353, 713

Kauffmann G., Li C., Zhang W., Weinmann S., 2013, MNRAS, 430, 1447

Kaviraj S., Schawinski K., Silk J., Shabala S. S., 2011, MNRAS, 415, 3798

Kenney J. D. P., van Gorkom J. H., Vollmer B., 2004, AJ, 127, 3361

Kennicutt Jr. R. C., 1998, ARA&A, 36, 189

Kereš D., Katz N., Weinberg D. H., Davé R., 2005, MNRAS, 363, 2

Kereš D., Katz N., Davé R., Fardal M., Weinberg D. H., 2009, MNRAS, 396, 2332

Kewley L. J., Dopita M. A., 2002, ApJS, 142, 35

Kewley L. J., Ellison S. L., 2008, ApJ, 681, 1183

Kewley L. J., Dopita M. A., Sutherland R. S., Heisler C. A., Trevena J., 2001, ApJ, 556, 121

Kewley L. J., Dopita M. A., Leitherer C., Davé R., Yuan T., Allen M., Groves B., Sutherland R., 2013a, ApJ, 774, 100

Kewley L. J., Maier C., Yabe K., Ohta K., Akiyama M., Dopita M. A., Yuan T., 2013b, ApJ, 774, L10

Kewley L. J., et al., 2016, ApJ, 819, 100

Khaire V., Srianand R., 2015, ApJ, 805, 33

Kobayashi N., et al., 2000, in Iye M., Moorwood A. F., eds, Society of Photo-Optical Instrumentation Engineers (SPIE) Conference Series Vol. 4008, Optical and IR Telescope Instrumentation and Detectors. pp 1056–1066

Kobulnicky H. A., Kewley L. J., 2004, ApJ, 617, 240

Kodama T., Bower R. G., 2001, MNRAS, 321, 18

Kodama T., Smail I., 2001, MNRAS, 326, 637

Kodama T., Bower R. G., Bell E. F., 1999, MNRAS, 306, 561

Kodama T., Balogh M. L., Smail I., Bower R. G., Nakata F., 2004, MNRAS, 354, 1103

Kodama T., et al., 2005, PASJ, 57, 309

Kodama T., Tanaka I., Kajisawa M., Kurk J., Venemans B., De Breuck C., Vernet J., Lidman C., 2007, MNRAS, 377, 1717

Kodama T., Hayashi M., Koyama Y., Tadaki K.-i., Tanaka I., Shimakawa R., 2013, in Thomas D., Pasquali A., Ferreras I., eds, IAU Symposium Vol. 295, IAU Symposium. pp 74–77, doi:10.1017/S1743921313004353

Koester B. P., et al., 2007, ApJ, 660, 239

Kollmeier J. A., Weinberg D. H., Davé R., Katz N., 2003, ApJ, 594, 75

Konno A., Ouchi M., Nakajima K., Duval F., Kusakabe H., Ono Y., Shimasaku K., 2016, ApJ, 823, 20

Kormendy J., Bender R., 1996, ApJ, 464, L119

Koyama Y., Kodama T., Shimasaku K., Hayashi M., Okamura S., Tanaka I., Tokoku C., 2010, MNRAS, 403, 1611

Koyama Y., Kodama T., Nakata F., Shimasaku K., Okamura S., 2011, ApJ, 734, 66

Koyama Y., Kodama T., Tadaki K.-i., Hayashi M., Tanaka M., Smail I., Tanaka I., Kurk J., 2013a, MNRAS, 428, 1551

Koyama Y., et al., 2013b, MNRAS, 434, 423

Koyama Y., Kodama T., Tadaki K.-i., Hayashi M., Tanaka I., Shimakawa R., 2014, ApJ, 789, 18

Koyama Y., et al., 2015, MNRAS, 453, 879

Kriek M., van Dokkum P. G., Labbé I., Franx M., Illingworth G. D., Marchesini D., Quadri R. F., 2009, ApJ, 700, 221

Kriek M., et al., 2014, preprint, (arXiv:1412.1835)

Kronberger T., Kapferer W., Ferrari C., Unterguggenberger S., Schindler S., 2008a, A&A, 481, 337

Kronberger T., Kapferer W., Unterguggenberger S., Schindler S., Ziegler B. L., 2008b, A&A, 483, 783

Kubo M., Yamada T., Ichikawa T., Kajisawa M., Matsuda Y., Tanaka I., 2015, ApJ, 799, 38

Kulas K. R., et al., 2013, ApJ, 774, 130

Kurk J. D., et al., 2000, A&A, 358, L1

Kurk J. D., Pentericci L., Röttgering H. J. A., Miley G. K., 2004a, A&A, 428, 793

Kurk J. D., Pentericci L., Overzier R. A., Röttgering H. J. A., Miley G. K., 2004b, A&A, 428, 817

Lagos C. D. P., Baugh C. M., Lacey C. G., Benson A. J., Kim H.-S., Power C., 2011, MNRAS, 418, 1649

Law D. R., Steidel C. C., Erb D. K., Pettini M., Reddy N. A., Shapley A. E., Adelberger K. L., Simenc D. J., 2007, ApJ, 656, 1

Lawrence A., et al., 2007, MNRAS, 379, 1599

Le Floc'h E., et al., 2005, ApJ, 632, 169

Lee K.-G., et al., 2013, AJ, 145, 69

Lee K.-G., Hennawi J. F., White M., Croft R. A. C., Ozbek M., 2014a, ApJ, 788, 49

Lee K.-G., et al., 2014b, ApJ, 795, L12

Lee K.-S., Dey A., Hong S., Reddy N., Wilson C., Jannuzi B. T., Inami H., Gonzalez A. H., 2014c, ApJ, 796, 126

Lee K.-G., et al., 2016, ApJ, 817, 160

Lehmer B. D., et al., 2009, ApJ, 691, 687

Lehmer B. D., et al., 2013, ApJ, 765, 87

Levesque E. M., Richardson M. L. A., 2014, ApJ, 780, 100

Liang Y. C., Yin S. Y., Hammer F., Deng L. C., Flores H., Zhang B., 2006, ApJ, 652, 257

Lilly S. J., Le Fevre O., Hammer F., Crampton D., 1996, ApJ, 460, L1

Lilly S. J., Carollo C. M., Pipino A., Renzini A., Peng Y., 2013, ApJ, 772, 119

Lin L., et al., 2010, ApJ, 718, 1158

Liu X., Shapley A. E., Coil A. L., Brinchmann J., Ma C.-P., 2008, ApJ, 678, 758

Lofthouse E. K., Kaviraj S., Conselice C. J., Mortlock A., Hartley W., 2016, preprint, (arXiv:1608.03892)

López-Cruz O., Barkhouse W. A., Yee H. K. C., 2004, ApJ, 614, 679

Lowenthal J. D., et al., 1997, ApJ, 481, 673

Lynds R., 1971, ApJ, 164, L73

Madau P., Dickinson M., 2014, ARA&A, 52, 415

Madau P., Ferguson H. C., Dickinson M. E., Giavalisco M., Steidel C. C., Fruchter A., 1996, MNRAS, 283, 1388

Magnelli B., Elbaz D., Chary R. R., Dickinson M., Le Borgne D., Frayer D. T., Willmer C. N. A., 2011, A&A, 528, A35

Magnelli B., et al., 2013, A&A, 553, A132

Maiolino R., et al., 2008, A&A, 488, 463

Maloney P. R., Hollenbach D. J., Tielens A. G. G. M., 1996, ApJ, 466, 561

Mannucci F., Della Valle M., Panagia N., 2007, MNRAS, 377, 1229

Mannucci F., Cresci G., Maiolino R., Marconi A., Gnerucci A., 2010, MNRAS, 408, 2115

Mannucci F., Salvaterra R., Campisi M. A., 2011, MNRAS, 414, 1263

Martig M., Bournaud F., Teyssier R., Dekel A., 2009, ApJ, 707, 250

Matsuda Y., et al., 2009, MNRAS, 400, L66

Matsuda Y., et al., 2011a, MNRAS, 410, L13

Matsuda Y., et al., 2011b, MNRAS, 416, 2041

Matsuda Y., et al., 2012, MNRAS, 425, 878

Matthee J., Sobral D., Oteo I., Best P., Smail I., Röttgering H., Paulino-Afonso A., 2016, MNRAS, 458, 449

Mayo J. H., Vernet J., De Breuck C., Galametz A., Seymour N., Stern D., 2012, A&A, 539, A33

McGaugh S. S., 1991, ApJ, 380, 140

McGee S. L., Balogh M. L., Bower R. G., Font A. S., McCarthy I. G., 2009, MNRAS, 400, 937

McLean I. S., et al., 2010, in Society of Photo-Optical Instrumentation Engineers (SPIE) Conference Series. p. 1, doi:10.1117/12.856715

McLean I. S., et al., 2012, in Society of Photo-Optical Instrumentation Engineers (SPIE) Conference Series. , doi:10.1117/12.924794

Meiksin A. A., 2009, Reviews of Modern Physics, 81, 1405

Merluzzi P., Busarello G., Dopita M. A., Haines C. P., Steinhauser D., Bourdin H., Mazzotta P., 2016, MNRAS, 460, 3345

Mihos J. C., Hernquist L., 1996, ApJ, 464, 641

Miley G. K., et al., 2004, Nature, 427, 47

Miley G. K., et al., 2006, ApJ, 650, L29

Minowa Y., et al., 2010, in Society of Photo-Optical Instrumentation Engineers (SPIE) Conference Series. , doi:10.1117/12.857818

Miyazaki S., et al., 2002, PASJ, 54, 833

Miyazaki S., et al., 2012, in Ground-based and Airborne Instrumentation for Astronomy IV. p. 84460Z, doi:10.1117/12.926844

Momcheva I. G., et al., 2016, ApJS, 225, 27

Montero-Dorta A. D., et al., 2009, MNRAS, 392, 125

Moore B., Katz N., Lake G., Dressler A., Oemler A., 1996, Nature, 379, 613

Moore B., Lake G., Katz N., 1998, ApJ, 495, 139

Moore B., Ghigna S., Governato F., Lake G., Quinn T., Stadel J., Tozzi P., 1999, ApJ, 524, L19

Muratov A. L., Kereš D., Faucher-Giguère C.-A., Hopkins P. F., Quataert E., Murray N., 2015, MNRAS, 454, 2691

Naab T., Johansson P. H., Ostriker J. P., 2009, ApJ, 699, L178

Naab T., et al., 2014, MNRAS, 444, 3357

Nagao T., Maiolino R., Marconi A., 2006, A&A, 459, 85

Nakajima K., Ouchi M., 2014, MNRAS, 442, 900

Nakajima K., Ouchi M., Shimasaku K., Hashimoto T., Ono Y., Lee J. C., 2013, ApJ, 769, 3

Nanayakkara T., et al., 2016, ApJ, 828, 21

Navarro J. F., Frenk C. S., White S. D. M., 1995, MNRAS, 275, 56

Navarro J. F., Frenk C. S., White S. D. M., 1996, ApJ, 462, 563

Newman S. F., et al., 2014, ApJ, 781, 21

Niino Y., 2012, ApJ, 761, 126

Nilsson K. K., et al., 2007, A&A, 471, 71

Noeske K. G., et al., 2007, ApJ, 660, L43

Obreschkow D., Rawlings S., 2009, ApJ, 696, L129

Ogle P., Davies J. E., Appleton P. N., Bertincourt B., Seymour N., Helou G., 2012, ApJ, 751, 13

Ohta K., et al., 2003, ApJ, 598, 210

Okamoto T., Habe A., 1999, ApJ, 516, 591

Okamoto T., Habe A., 2000, PASJ, 52, 457

Okamoto T., Nagashima M., 2001, ApJ, 547, 109

Okamoto T., Nagashima M., 2003, ApJ, 587, 500

Okamoto T., Nemmen R. S., Bower R. G., 2008, MNRAS, 385, 161

Okamoto T., Frenk C. S., Jenkins A., Theuns T., 2010, MNRAS, 406, 208

Oke J. B., Gunn J. E., 1983, ApJ, 266, 713

Olsen K. P., Rasmussen J., Toft S., Zirm A. W., 2013, ApJ, 764, 4

Omand C. M. B., Balogh M. L., Poggianti B. M., 2014, MNRAS, 440, 843

Ono Y., et al., 2010a, MNRAS, 402, 1580

Ono Y., Ouchi M., Shimasaku K., Dunlop J., Farrah D., McLure R., Okamura S., 2010b, ApJ, 724, 1524

Onodera M., et al., 2016, ApJ, 822, 42

Oppenheimer B. D., Davé R., 2006, MNRAS, 373, 1265

Oppenheimer B. D., Davé R., 2008, MNRAS, 387, 577

Osterbrock D. E., 1974, Astrophysics of gaseous nebulae

Oteo I., Sobral D., Ivison R. J., Smail I., Best P. N., Cepa J., Pérez-García A. M., 2015, MNRAS, 452, 2018

Ouchi M., et al., 2003, ApJ, 582, 60

Ouchi M., et al., 2004, ApJ, 611, 660

Ouchi M., et al., 2005, ApJ, 620, L1

Ouchi M., et al., 2008, ApJS, 176, 301

Overzier R. A., et al., 2008, ApJ, 673, 143

Papovich C., et al., 2012, ApJ, 750, 93

Peeples M. S., Shankar F., 2011, MNRAS, 417, 2962

Peirani S., Weinberg D. H., Colombi S., Blaizot J., Dubois Y., Pichon C., 2014, ApJ, 784, 11

Peng C. Y., Ho L. C., Impey C. D., Rix H.-W., 2010a, AJ, 139, 2097

Peng Y.-j., et al., 2010b, ApJ, 721, 193

Peng Y., Maiolino R., Cochrane R., 2015, Nature, 521, 192

Pentericci L., Roettgering H. J. A., Miley G. K., Carilli C. L., McCarthy P., 1997, A&A, 326, 580

Pentericci L., et al., 2000, A&A, 361, L25

Pentericci L., Kurk J. D., Carilli C. L., Harris D. E., Miley G. K., Röttgering H. J. A., 2002, A&A, 396, 109

Pérez-González P. G., et al., 2008, ApJ, 675, 234

Pettini M., Pagel B. E. J., 2004, MNRAS, 348, L59

Pilyugin L. S., 2001, A&A, 369, 594

Pilyugin L. S., Thuan T. X., 2005, ApJ, 631, 231

Price S. H., et al., 2014, ApJ, 788, 86

Prieto M., et al., 2013, MNRAS, 428, 999

Quilis V., Moore B., Bower R., 2000, Science, 288, 1617

Rauch M., 1998, ARA&A, 36, 267

Reddy N. A., Steidel C. C., 2009, ApJ, 692, 778

Reddy N. A., Erb D. K., Steidel C. C., Shapley A. E., Adelberger K. L., Pettini M., 2005, ApJ, 633, 748

Reddy N. A., et al., 2015, ApJ, 806, 259

Reddy N. A., Steidel C. C., Pettini M., Bogosavljević M., 2016a, ApJ, 828, 107

Reddy N. A., Steidel C. C., Pettini M., Bogosavljević M., Shapley A. E., 2016b, ApJ, 828, 108

Riechers D. A., Carilli C. L., Walter F., Momjian E., 2010, ApJ, 724, L153

Rix H.-W., et al., 2004, ApJS, 152, 163

Roediger E., Brüggen M., 2007, MNRAS, 380, 1399

Rowan-Robinson M., et al., 2016, MNRAS, 461, 1100

Salim S., et al., 2007, ApJS, 173, 267

Sanders R. L., et al., 2015, ApJ, 799, 138

Sanders R. L., et al., 2016, ApJ, 816, 23

Santini P., et al., 2014, A&A, 562, A30

Santos J. S., et al., 2014, MNRAS, 438, 2565

Sarazin C. L., 1986, Reviews of Modern Physics, 58, 1

Sargent W. L. W., Young P. J., Boksenberg A., Tytler D., 1980, ApJS, 42, 41

Sato T., Matsushita K., Ota N., Sato K., Nakazawa K., Sarazin C. L., 2011, PASJ, 63, S991

Scannapieco E., Pichon C., Aracil B., Petitjean P., Thacker R. J., Pogosyan D., Bergeron J., Couchman H. M. P., 2006, MNRAS, 365, 615

Schawinski K., et al., 2007a, ApJS, 173, 512

Schawinski K., Thomas D., Sarzi M., Maraston C., Kaviraj S., Joo S.-J., Yi S. K., Silk J., 2007b, MNRAS, 382, 1415

Schawinski K., et al., 2009a, ApJ, 690, 1672

Schawinski K., Virani S., Simmons B., Urry C. M., Treister E., Kaviraj S., Kushkuley B., 2009b, ApJ, 692, L19

Schawinski K., Dowlin N., Thomas D., Urry C. M., Edmondson E., 2010, ApJ, 714, L108

Schawinski K., et al., 2014, MNRAS, 440, 889

Schaye J., Carswell R. F., Kim T.-S., 2007, MNRAS, 379, 1169

Schiminovich D., et al., 2005, ApJ, 619, L47

Schlafly E. F., Finkbeiner D. P., 2011, ApJ, 737, 103

Seko A., Ohta K., Yabe K., Hatsukade B., Akiyama M., Tamura N., Iwamuro F., Dalton G., 2016, ApJ, 833, 53

Shankar F., Weinberg D. H., Miralda-Escudé J., 2009, ApJ, 690, 20

Shapley A. E., Steidel C. C., Pettini M., Adelberger K. L., 2003, ApJ, 588, 65

Shapley A. E., Coil A. L., Ma C.-P., Bundy K., 2005, ApJ, 635, 1006

Shapley A. E., et al., 2015, ApJ, 801, 88

Shibuya T., et al., 2014, ApJ, 788, 74

Shimakawa R., Kodama T., Tadaki K.-i., Tanaka I., Hayashi M., Koyama Y., 2014, MNRAS, 441, L1

Shimakawa R., Kodama T., Tadaki K.-i., Hayashi M., Koyama Y., Tanaka I., 2015a, MNRAS, 448, 666

Shimakawa R., et al., 2015b, MNRAS, 451, 1284

Shimakawa R., et al., 2016, preprint, (arXiv:1607.08005)

Shimasaku K., et al., 2003, ApJ, 586, L111

Shivaei I., et al., 2015, ApJ, 815, 98

Sijacki D., Springel V., Di Matteo T., Hernquist L., 2007, MNRAS, 380, 877

Simcoe R. A., Sargent W. L. W., Rauch M., Becker G., 2006, ApJ, 637, 648

Skelton R. E., et al., 2014, ApJS, 214, 24

Skibba R. A., et al., 2009, MNRAS, 399, 966

Smail I., et al., 2014, ApJ, 782, 19

Sobral D., et al., 2009, MNRAS, 398, 75

Sobral D., Smail I., Best P. N., Geach J. E., Matsuda Y., Stott J. P., Cirasuolo M., Kurk J., 2013, MNRAS, 428, 1128

Sobral D., Best P. N., Smail I., Mobasher B., Stott J., Nisbet D., 2014, MNRAS, 437, 3516

Sobral D., et al., 2016, preprint, (arXiv:1609.05897)

Songaila A., Cowie L. L., 2002, AJ, 123, 2183

Sparre M., et al., 2015, MNRAS, 447, 3548

Speagle J. S., Steinhardt C. L., Capak P. L., Silverman J. D., 2014, ApJS, 214, 15

Springel V., Hernquist L., 2003, MNRAS, 339, 312

Springel V., et al., 2005, Nature, 435, 629

Stanway E. R., Eldridge J. J., Becker G. D., 2016, MNRAS, 456, 485

Steidel C. C., Adelberger K. L., Dickinson M., Giavalisco M., Pettini M., Kellogg M., 1998, ApJ, 492, 428

Steidel C. C., Adelberger K. L., Shapley A. E., Pettini M., Dickinson M., Giavalisco M., 2000, ApJ, 532, 170

Steidel C. C., Shapley A. E., Pettini M., Adelberger K. L., Erb D. K., Reddy N. A., Hunt M. P., 2004, ApJ, 604, 534

Steidel C. C., Erb D. K., Shapley A. E., Pettini M., Reddy N., Bogosavljević M., Rudie G. C., Rakic O., 2010, ApJ, 717, 289

Steidel C. C., Bogosavljević M., Shapley A. E., Kollmeier J. A., Reddy N. A., Erb D. K., Pettini M., 2011, ApJ, 736, 160

Steidel C. C., et al., 2014, ApJ, 795, 165

Steidel C. C., Strom A. L., Pettini M., Rudie G. C., Reddy N. A., Trainor R. F., 2016, ApJ, 826, 159

Stott J. P., Pimbblet K. A., Edge A. C., Smith G. P., Wardlow J. L., 2009, MNRAS, 394, 2098

Stott J. P., et al., 2013, MNRAS, 436, 1130

Strateva I., et al., 2001, AJ, 122, 1861

Strom A. L., Steidel C. C., Rudie G. C., Trainor R. F., Pettini M., Reddy N. A., 2016, preprint, (arXiv:1608.02587)

Strömgren B., 1939, ApJ, 89, 526

Struble M. F., Rood H. J., 1999, ApJS, 125, 35

Sunyaev R. A., Zeldovich Y. B., 1972, A&A, 20, 189

Suzuki R., et al., 2008, PASJ, 60, 1347

Suzuki T. L., et al., 2015, ApJ, 806, 208

Tacconi L. J., et al., 2010, Nature, 463, 781

Tacconi L. J., et al., 2013, ApJ, 768, 74

Tadaki K.-I., Kodama T., Koyama Y., Hayashi M., Tanaka I., Tokoku C., 2011, PASJ, 63, 437

Tadaki K.-i., et al., 2012, MNRAS, 423, 2617

Tadaki K.-i., Kodama T., Tanaka I., Hayashi M., Koyama Y., Shimakawa R., 2013, ApJ, 778, 114

Tadaki K.-i., Kodama T., Tanaka I., Hayashi M., Koyama Y., Shimakawa R., 2014, ApJ, 780, 77

Tadaki K.-i., et al., 2016, preprint, (arXiv:1608.05412)

Tal T., et al., 2014, ApJ, 789, 164

Tanaka I., et al., 2011, PASJ, 63, 415

Tanaka M., et al., 2013a, PASJ, 65, 17

Tanaka M., et al., 2013b, ApJ, 772, 113

Taylor M. B., 2015, in Taylor A. R., Rosolowsky E., eds, Astronomical Society of the Pacific Conference Series Vol. 495, Astronomical Society of the Pacific Conference Series. p. 177 (arXiv:1410.8507)

Thomas D., Maraston C., Bender R., Mendes de Oliveira C., 2005, ApJ, 621, 673

Tinsley B. M., 1980, Fund. Cosmic Phys., 5, 287

Tomczak A. R., et al., 2016, ApJ, 817, 118

Toomre A., Toomre J., 1972, ApJ, 178, 623

Toshikawa J., et al., 2012, ApJ, 750, 137

Toshikawa J., et al., 2016, ApJ, 826, 114

Tran K.-V. H., et al., 2010, ApJ, 719, L126

Trayford J. W., Theuns T., Bower R. G., Crain R. A., Lagos C. d. P., Schaller M., Schaye J., 2016, MNRAS, 460, 3925

Tremonti C. A., 2003, PhD thesis, THE JOHNS HOPKINS UNIVERSITY

Tremonti C. A., et al., 2004, ApJ, 613, 898

Troncoso P., et al., 2014, A&A, 563, A58

Trump J. R., et al., 2013, ApJ, 763, L6

Valentino F., et al., 2015, ApJ, 801, 132

Veilleux S., Osterbrock D. E., 1987, ApJS, 63, 295

Venemans B. P., et al., 2002, ApJ, 569, L11

Venemans B. P., et al., 2005, A&A, 431, 793

Venemans B. P., et al., 2007, A&A, 461, 823

Villar-Martín M., Sánchez S. F., Humphrey A., Dijkstra M., di Serego Alighieri S., De Breuck C., González Delgado R., 2007, MNRAS, 378, 416

Visvanathan N., Sandage A., 1977, ApJ, 216, 214

Whitaker K. E., et al., 2014, ApJ, 795, 104

Whitaker K. E., et al., 2015, ApJ, 811, L12

White S. D. M., Frenk C. S., 1991, ApJ, 379, 52

Wisnioski E., et al., 2015, ApJ, 799, 209

Wuyts S., et al., 2011, ApJ, 742, 96

Wuyts S., et al., 2013, ApJ, 779, 135

Wylezalek D., et al., 2013, ApJ, 769, 79

Yabe K., et al., 2012, PASJ, 64, 60

Yabe K., Ohta K., Akiyama M., Iwamuro F., Tamura N., Yuma S., Dalton G., Lewis I., 2015, ApJ, 798, 45

Yagi M., Kashikawa N., Sekiguchi M., Doi M., Yasuda N., Shimasaku K., Okamura S., 2002, AJ, 123, 66

Yamada T., et al., 2009, ApJ, 699, 1354

Yamada T., Nakamura Y., Matsuda Y., Hayashino T., Yamauchi R., Morimoto N., Kousai K., Umemura M., 2012, AJ, 143, 79

Yates R. M., Kauffmann G., Guo Q., 2012, MNRAS, 422, 215

Yin S. Y., Liang Y. C., Hammer F., Brinchmann J., Zhang B., Deng L. C., Flores H., 2007, A&A, 462, 535

Yoshikawa T., et al., 2010, ApJ, 718, 112

Yuan T., et al., 2014, ApJ, 795, L20

Zahid H. J., Dima G. I., Kudritzki R.-P., Kewley L. J., Geller M. J., Hwang H. S., Silverman J. D., Kashino D., 2014, ApJ, 791, 130

Zaritsky D., Kennicutt Jr. R. C., Huchra J. P., 1994, ApJ, 420, 87

van Dokkum P. G., 2001, PASP, 113, 1420

van Dokkum P. G., et al., 2010, ApJ, 709, 1018

van Dokkum P. G., et al., 2011, ApJ, 743, L15

van de Voort F., Schaye J., Booth C. M., Haas M. R., Dalla Vecchia C., 2011, MNRAS, 414, 2458

van der Wel A., et al., 2012, ApJS, 203, 24